

AD657169

53

USL Report No. 834

Measurement of the Dissipation Associated with the Electromechanical Coupling in Piezoelectric Ceramics

RALPH S. WOOLLETT
Applied Research Branch
Sonar Transducer Division



12 July 1967

D D C
DRAFTED
AUG 30 1967
RECORDED
C

This document has been approved for public release and sale;
its distribution is unlimited.

U. S. Navy Underwater Sound Laboratory
Fort Trumbull, New London, Connecticut

CLEARINGHOUSE

143

ABSTRACT

The object of this investigation is to develop methods for precise measurements of velocity or displacement (including their phase angles as well as their magnitudes) and to apply these methods to extend the knowledge of the dissipative parameters of piezoelectric ceramics.

Laser interferometry is a very promising new method for measuring small vibrations. In this method the motion of a small mirror attached to the vibrating body phase-modulates the light beam, and the light beam is subsequently demodulated by a photomultiplier tube. An electronic control system was developed to stabilize the interferometer against low-frequency building vibrations. In this system the mirror of the interferometer that is normally fixed is mounted on a small piezoelectric transducer. This transducer is driven by a servo amplifier in such a manner that it keeps the path length of the interfering beams constant at low frequencies. Building vibrations thus are canceled out, but the control system becomes inoperative above 1 kHz and, hence, does not interfere with the measurement of the desired vibration signals, which are in this upper frequency range. Another feedback control system was developed to stabilize the amplitude of the laser output, which was found to fluctuate as much as 10 percent. These fluctuations were reduced to about 1 percent.

After suitable measurement methods had been developed, measurements were made of the electromechanical transfer ratios of a number of ceramic samples. It was found that there is no simple one-to-one relation between the mechanical displacement and the polarization under stiffly controlled conditions. The phase angle between the displacement and charge in barium titanate bars with transverse field becomes a lead angle at high drive levels. The amplitude of displacement for these bars is more nearly proportional to the electric field than to the polarization. Some samples were measured under blocked conditions by use of quarter-wave blocking stubs. In this way enough data were obtained to calculate a complete set of two-port parameters.

ADMINISTRATIVE INFORMATION

This study was originally prepared as a dissertation in partial fulfillment of the requirements for the degree Doctor of Philosophy in Electrical Engineering at the University of Connecticut. The work was accomplished under USL Project No. 7-1-451-00-06 and Navy Subproject and Task No. SF 101 03 18-11287.

The author wishes to express his gratitude to Professor C. W. Schultz for helpful discussions and encouragement during the course of this work and to Professors H. M. Lical and D. E. Spencer for assistance in planning the project and in the preparation of the manuscript. Support of this work by the U. S. Navy Underwater Sound Laboratory is gratefully acknowledged. In addition, the author wishes to express his appreciation to the many individuals at the Laboratory who generously provided special services needed to keep this project on schedule.

ACCESSION for		
CFSTI	WHITE SECTION <input checked="" type="checkbox"/>	BLACK SECTION <input type="checkbox"/>
DOC		
ANNOUNCED		
JUSTIFICATION		
BY		
DISTRIBUTION/AVAILABILITY CODES		
BIST.	AVAIL. and/or SPECIAL	
/		

REVIEWED AND APPROVED: 12 July 1967

J. E. Nash
Technical Director


R. L. Corkran, Jr., Captain, USM
Commanding Officer and Director

TABLE OF CONTENTS

	Page
LIST OF TABLES	iii
LIST OF ILLUSTRATIONS	v
Chapter	
I. INTRODUCTION	1
II. SPECIFIC OBJECTIVES AND MEASUREMENT PLANS	7
2.1 Objectives in Terms of Ceramic Parameters	7
2.2 Objectives in Terms of Transducer Parameters	11
2.3 Possible Mechanical Terminations for the Transducer	18
2.4 Existing Data and Scope of Investigation	21
III. VIBRATION INTERFEROMETRY	27
3.1 Introduction	27
3.2 Theory of the Interferometer	29
3.3 Setting Up and Adjusting the Interferometer	38
3.3.1 Major Components	39
3.3.2 Alignment Procedure	42
3.3.3 Choice of Pinhole Size	44
3.4 A Control System for Stabilizing the Operating Point	46
3.4.1 Description of System	48
3.4.2 Design Objectives	50
3.4.3 Mirror Transducer	52
3.4.4 System Analysis	54
3.4.5 Measured Characteristics	63
3.4.6 Input Impedance at Signal Frequencies	67

Chapter		Page
3.4.7	Evaluation of the Control System	69
3.5	Laser Amplitude Control	72
3.6	Performance of the Interferometer	78
IV.	SENSORS USING OPTICAL-FIBER BUNDLES	79
4.1	The Fotonic Sensor	79
4.2	Attempts to Improve Signal-to-Noise Ratio	82
V.	ELECTRICAL INSTRUMENTATION	85
5.1	Generation of High a.c. Voltage	85
5.2	Measurement of Amplitude and Phase	87
5.2.1	Driving-Point Impedance Bridge	89
5.2.2	Transfer Parameter Bridges	92
5.2.3	Phase Calibration of the Interferometer	95
5.2.4	Advantages and Disadvantages of Null Methods	99
5.2.5	Phase Balancing by Lissajous Patterns	99
5.2.6	Relative Phase Measurements with Fotonic Sensor	103
VI.	MOUNTING SYSTEM FOR THE CERAMIC BARS	105
6.1	Stabilizing the Bar Against Building Vibrations	105
6.2	Behavior at Frequencies Used for Measurements	110
VII.	MEASURED CERAMIC PROPERTIES	113
7.1	5-inch Barium Titanate Bar	113
7.2	5-inch Lead Titanate Zirconate Bars	119
7.3	3/4-inch Lead Titanate Zirconate Bars	127
7.4	Discussion of Results	131
VIII.	CONCLUSIONS	135
	BIBLIOGRAPHY	137
	INITIAL DISTRIBUTION LIST	Inside Back Cover

LIST OF TABLES

Table	Page
1 High-Field Data on the 5-inch PZT Bar	121

LIST OF ILLUSTRATIONS

Figure		Page
1	Electromechanical Circuit of the Stiffness-Controlled Lossless Transducer	13
2	Electromechanical Circuit of the Stiffness-Controlled Transducer with General Dissipation	15
3	Transformation of the Circuit of Figure 2 to Eliminate the Non-Conservative Coupler	17
4	Simplified Diagram of the Vibration Interferometer	30
5	Homodyne Detector Operating Characteristic	34
6	Profile of Expanded Laser Beam	45
7	Control System for Stabilizing the Operating Point	49
8	Mirror Transducer for Adjusting Interferometer Path Length	53
9	Block Diagram of the Control System	55
10	Redrawn Control System Diagram	59
11	Closed-Loop Response of the Mirror Control System to a Path-Length Disturbance	64
12	Relative Current Response of Interferometer to Mechanical Displacement of Constant Amplitude	65
13	Circuit Representation of the Input Admittance	68
14	Relative Spectrum of Noise Output of Interferometer	71
15	Feedback System to Stabilize Laser Intensity	74

Figure	Page
16 Paths of Primary Beam and Laser Monitor	76
17 Optical-Fiber Displacement Sensor	80
18 High-Voltage Power Supplies	88
19 Driving-Point Impedance Bridge	90
20 Transfer Parameter Bridges	93
21 Phase Measurement Circuits	96
22 Calibration Circuit after Thévenin Transformation	98
23 Oscilloscope Patterns Obtained with the Circuit of Figure 21b	100
24 Five-inch Barium Titanate Bar Mounted on Vibrator Carriage	106
25 3/8" x 3/4" PZT-4 Ceramic Vibrators	107
26 Driving-Point Impedance of a Flexing Beam	110
27 5-inch Barium Titanate Bar Permittivity and Input Dissipation Factor	114
28 5-inch Barium Titanate Bar (a) Strain (b) Transfer Phase Angles	115
29 5-inch PZT Bar Permittivity and Input Dissipation Factor	122
30 5-inch PZT Bar (a) Strain (b) Transfer Phase Angles	124
31 3/4-inch PZT Bar Permittivity and Input Dissipation Factor	128
32 3/4-inch PZT Bar (a) Strain (b) Transfer Phase Angles	130

INTRODUCTION

When piezoelectric ceramics became available commercially, shortly after World War II, they rapidly replaced most of the other piezoelectric and magnetostrictive materials that had been used in Naval sonar and industrial ultrasonics. The piezoelectric ceramics have higher electromechanical coupling and higher power handling capacity than their competitors for service in electromechanical transducers. They are at a disadvantage for applications requiring high stability or very low losses; and in these cases, crystals, such as quartz, still reign supreme. But for most applications requiring the generation or detection of sound in liquids and solids, the ruggedness, economy, and power capability of the ceramics are more important considerations than their susceptibility to change of properties with age and use.

The first piezoelectric ceramic to become available was barium titanate but in recent years ceramics composed of solid solutions of lead titanate/lead zirconate have been overtaking barium titanate in popularity. The latter ceramics have higher electromechanical coupling and power capability than barium titanate, and they are available in compositions with a wide range of properties. The piezoelectricity of the ceramics is an induced property, brought about by the poling process which creates a semipermanent electric polarization in the material. This phenomenon is a manifestation of the ferroelectric nature of the individual crystals

composing these ceramics; the basic physics of these materials has been covered in a number of recent books.⁽³⁾⁻⁽⁴⁾

Piezoelectric behavior in the ceramics is achieved by linearizing their characteristics for small signals by means of the poling process, which establishes an operating point that is favorable for linear operation. Basically, though, the materials are highly nonlinear in most of their properties; and when the large signals required in high-power sonic applications are applied to the poled ceramics, the underlying nonlinearity again becomes evident. Nevertheless, the linear theory of classical piezoelectricity is used to great advantage in the engineering application of these materials to transducer design. The measurements and reporting of the technically important properties are done in terms of the linear theory. An excellent summary of this information is given in a recent book compiled by W. P. Mason.⁽⁵⁾

Not only nonlinearities but also dissipative phenomena are neglected in classical piezoelectric theory. The material is treated as a conservative system, and the equations of state are derived from thermodynamic potentials.^{(6),(7)} This approach is an excellent one for normal piezoelectric crystals, since their highly ordered structure does indeed result in linear behavior and very low dissipation. For small signals this treatment is also satisfactory for prepolarized ceramics; the dissipation factors at low levels rarely exceed 1 percent for properly made ceramics. Some information has been made available on the dissipation in piezoelectric ceramics at high signal levels.⁽⁵⁾ The existing data, however, are derived from measurements made only at the electrical terminals of the ceramic transducers. Such measurements are relatively easy to make, but they can not provide complete information on the dissipative parameters of the transducer.

The object of the present work is to extend the knowledge of the dissipative parameters of piezoelectric ceramics, and the approach is to conduct measurements simultaneously of electrical variables at the input and mechanical variables at the output of the ceramic while it is operating as an electromechanical transducer. The simplest such transducer has two ports (one electrical; one mechanical), and it is fundamentally impossible to obtain all the parameters of a transducer by measurements involving only one port. Either mechanical variables, such as force and velocity, have to be measured along with voltage and current, or loads of known mechanical impedance have to be applied to the mechanical port when the electrical measurements are made. In either case, highly accurate mechanical measurements are required if really useful results are to be obtained, especially for the dissipative parameters. The difficulty of making these accurate mechanical measurements is the reason that the desired data have not been made available in the past.

Of the two mechanical variables, force and velocity, velocity is the easier one to measure. Measurement of force at the mechanical port requires insertion of a force gauge between the transducer surface and the mechanical load. Such a gauge might consist of a slab of piezoelectric material; its construction and calibration would involve some difficulties but the main problem is in connecting it into the mechanical circuit. The mechanical analog of the nearly infinitely conductive clip lead used in electrical measurements is a nearly infinitely stiff adhesive bond. Bonding the force gauge into place unfortunately is a much more difficult operation than attaching clip leads; and subsequent removal of the bonds, nondestructively, verges on the impossible. The epoxy adhesives used with ceramics

are an order of magnitude less stiff than the ceramics themselves, and they are noticeably dissipative. These considerations led to the belief that force measurements were best left until the art of mechanical measurements was further advanced, and only velocity measurements were planned for the present investigation. Since sinusoidal signals are employed, the distinction between velocity V and displacement ξ is trivial; $V = j\omega\xi$, where ω is the angular frequency. Actually, displacement is the directly measured variable in this work.

Displacement, or velocity, may be measured without contacting the vibrating surface, and it thus qualifies as a minimum disturbance type of measurement. One method of measurement is to place a small capacitor plate near a conductive vibrating surface; the variation in capacity resulting from the vibrations may be detected by a variety of electronic circuits.^{(8),(9)} Experience with capacitive probes used to measure vibrations of ceramics driven with strong electric fields indicates that it is difficult to shield the probes from direct electrical pickup of the a.c. driving field. Another limitation of this method is that the measurements are not absolute; the probe must be calibrated. An alternate approach is to use optical methods; these require only that a light beam be reflected from the vibrating surface. Modern interferometry applied to vibration measurement appears extremely promising; so this was adopted as the primary method of measurement. It is an absolute type of measurement. Another optical method using fiber optics to transmit light to and from a vibrating surface was adopted as a secondary method.

The development of measurement techniques for obtaining two-port parameters of ceramic transducers, particularly dissipative parameters, was considered to be the main objective of this investigation. Once such techniques have been perfected,

a large number of materials may be measured and different modes of motion investigated. Only a small amount of data on materials is included in this report, however. Study of dissipation in ceramics necessarily leads one into their nonlinear domain of operation, but a complete treatment of the nonlinear problem is beyond the scope of this investigation. In this project the electric field was run up to high levels, but the velocity was kept relatively low. A full study of nonlinearity would require that the velocity also be made high. A theoretical treatment of the nonlinear ceramic transducer is also lacking at the present time.

II

SPECIFIC OBJECTIVES AND MEASUREMENT PLANS

2.1 Objectives in Terms of Ceramic Parameters

Before the detailed measurement plans are presented, further discussion of the present state of knowledge of the ceramic properties is probably warranted. In linear piezoelectricity the materials are described by tensor equations of state. The general tensor theory has been worked out by J. H. Jurmain⁽¹⁰⁾ under the supervision of Professor Domina Spencer. The general theory is valid in any coordinate system and hence is the most powerful approach to advanced problems in dynamic piezoelectricity. Most authors, however, use Cartesian tensors and work only in rectangular coordinates. If one is willing to give up index balance, and risk losing sight of the tensorial nature of the quantities involved, abbreviations may be introduced which reduce the number of indices of the variables and coefficients in the piezoelectric equations. The equations then become matrix equations, and it is this form that has been standardized by the IEEE⁽¹¹⁾ and is generally used by engineers.

For example, if all the components of the stress applied to the ceramic are zero except for the extensional stresses T_1 and T_3 and all the electric field components zero except for E_3 , then the equations of state in terms of matrix components are

$$\begin{aligned}
 S_1 &= s_{11}^E T_1 + s_{12}^E T_3 + d_{31}^E E_3 \\
 S_2 &= s_{12}^E T_1 + s_{13}^E T_3 + d_{31}^E E_3 \\
 S_3 &= s_{13}^E T_1 + s_{33}^E T_3 + d_{33}^E E_3 \\
 D_3 &= d_{31}^E T_1 + d_{33}^E T_3 + \epsilon_{33}^T E_3
 \end{aligned} \tag{1}$$

S_1, S_2, S_3 are the extensional strains; D_3 is the electric displacement; $s_{11}^E, s_{12}^E, s_{13}^E, s_{33}^E$ are compliance constants at constant field; d_{31}^E, d_{33}^E are piezoelectric constants; and ϵ_{33}^T is the permittivity at constant stress. In ceramic piezoelectricity the convention has been established that the x_3 axis is the axis of permanent polarization. Hence, the electric field is here assumed to be applied in the direction of the permanent polarization; this is the usual situation unless excitation of shear motion is desired.

Poled ceramics have planar isotropy in the plane perpendicular to the poling axis (x_3). This symmetry causes them to have far fewer unique constants than exist for the most general piezoelectric crystal. In fact, they have 5 elastic constants, 3 piezoelectric constants, and 2 permittivities. A measurements program carried out over a period of several years by Clevite Corporation has produced values for all these constants for all of the technically important ceramics.⁽⁵⁾ The measurement procedures are described in IEEE Standards publications.⁽¹¹⁾ All measurements are electrical with one exception: the mass density. When the assumptions of linearity and no dissipation are made, this one mechanical measurement of density is sufficient. The other mechanical and electromechanical parameters may then be derived from electrical data.

When extensions of the classical piezoelectric theory to encompass dissipation

are attempted, it is reasonable to assume that a dissipative parameter will be associated with each of the constants defined under the lossless theory. Thus the piezoelectric ceramics might be expected to have ten independent dissipative parameters. The formal results of introducing dissipation into the piezoelectric equations by the standard procedure of letting all coefficients of the equations of state become complex has recently been set forth by Holland.⁽¹²⁾ His paper contains no physical data, however. To measure all ten dissipative parameters of the ceramics would require a very extensive measurement program.

Practical transducers often employ simple ceramic configurations, whose analysis involves only a few of the ceramic coefficients rather than the full set of ten. The present investigation will be limited to a study of these simple configurations. One such transducer consists of a slender ceramic bar of uniform cross-section, electroded on the ends. The electric field (and also the permanent polarization) is in the axial direction, x_3 . The mechanical loading is applied to the ends of the bar, and for simplicity it will be assumed that the loading is equal on each end. A stress T_3 exists because of the end loading. The sides of the bar are loaded only by air, and this is a negligible effect. The stresses T_1 and T_2 are thus zero at the surface, and since the lateral dimensions of the bar are very small in terms of wavelengths, these stresses are zero throughout the bar. The strains S_1 and S_2 exist but are not of present interest.

The useful equations of state for this vibrator are obtained from Equation (1) and are

$$\begin{aligned} S_3 &= S_{33}T_3 + d_{33}\mathcal{E}_3 \\ D_3 &= d_{33}T_3 + \mathcal{E}_{33}^T\mathcal{E}_3 \end{aligned} \quad (2)$$

Only three of the ceramic coefficients are involved. These equations of state may be put into another useful form by choosing D_3 to be an independent variable rather than \mathcal{E}_3 . The results in standard notation are written

$$\begin{aligned} S_3 &= s_{33}^D T_3 + g_{33} D_3 \\ \mathcal{E}_3 &= -g_{33} T_3 + \beta_{33}^T D_3 \end{aligned} \quad (3)$$

Here s_{33}^D is the compliance constant at constant electric displacement, g_{33} is a piezoelectric constant, and $\beta_{33}^T = 1/\epsilon_{33}^T$ is the impermeability at constant stress. The coefficients of Equation (3) are of course not independent but are obtainable from those of Equation (2).

Another simple transducer is a bar that is similar in every respect to the one described above except that the electrodes are on the sides rather than on the ends. In this case the bar is assumed to have a rectangular cross-section. The electric field is now transverse to the useful motion; the electromechanical coupling is less for this arrangement but is still high enough to provide useful performance. The axial direction of the bar will be taken to be x_1 ; the working stress is T_1 , while T_3 becomes zero because it is in the transverse direction. From Equation (1) the desired equations of state are seen to be

$$\begin{aligned} S_1 &= s_{11}^E T_1 + d_{31} \mathcal{E}_3 \\ D_3 &= d_{31} T_1 + \epsilon_{33}^T \mathcal{E}_3 \end{aligned} \quad (4)$$

The alternate set of equations is

$$\begin{aligned} S_1 &= s_{11}^D T_1 + g_{31} D_3 \\ \mathcal{E}_3 &= -g_{31} T_1 + \beta_{33}^T D_3 \end{aligned} \quad (5)$$

The objectives of this investigation may now be stated concisely: It is desired to find the loss parameters associated with the five coefficients $s_{11}^E, s_{33}^E, d_{31}, d_{33}$,

ϵ_{33}^T . This statement implies that the material will continue to be described adequately by the linear equations of state, even when it is driven with such large signals that the dissipation parameters have become significant. It is believed that a mildly nonlinear region of operation exists where such a compromise is meaningful. However, a further restriction on the scope of the present investigation appears desirable: The material will be operated only under low-strain conditions. Stated more specifically, the bar vibrators will be operated in the stiffness-controlled, or quasi-static, frequency range. If operation at the mechanical resonance took place, the strain would be greatly stepped up in relation to the electric driving field. Such operating conditions would be of practical interest, but there would be less chance of the linear equations retaining their validity if both the electric field and the strain were high. It appears best to first investigate the simpler situation of quasi-static operation.

Operation under stiffness-controlled conditions has the advantage that the stress and strain are uniform throughout the bar. In other words, the bar length is a small fraction of the acoustic wavelength under these conditions. This uniformity is important if the dissipation parameters depend on the strain level as they undoubtedly do. With nonuniform strain one would not measure an unambiguous material parameter but rather a parameter that depended on the strain distribution.

2.2 Objectives in Terms of Transducer Parameters

Consideration of the electromechanical circuits of the bar vibrators is of help in planning the measurement program. The bar vibrator operating as described earlier may well be thought of as a three-port transducer, since each end of the

bar may be considered to be a mechanical port. However, when it is stipulated that the two ends are equally loaded, then they may be combined into a single port. Suitable transducer equations, assuming linear operation, are the following:⁽¹³⁾

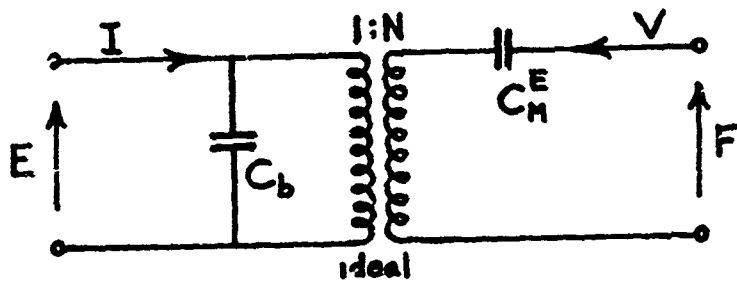
$$\begin{aligned} I &= Y_b E - NV \\ F &= NE + Z_M^E V \end{aligned} \quad (6)$$

E and I are the voltage and current, respectively, at the connections to the electrodes, V is the velocity of the end of the bar, F is the total force on the ends of the bar, Y_b is the electrical admittance when the ends of the bar are blocked, N is the electromechanical transfer ratio, and Z_M^E is the mechanical impedance when the electrical terminals are short-circuited.

With the transducer assumed to be lossless and operating in the stiffness-controlled frequency range, the electromechanical circuit which corresponds to Equation (6) is as shown in Figure 1. The coupler is an ideal electromechanical transformer. An important parameter of the transducer is its electromechanical coupling factor k , which plays a role analogous to that of the coupling coefficient of an electrical two-port network. The coupling factor is expressed in terms of the circuit parameters by the formula

$$\frac{k^2}{1-k^2} = \frac{N^2 C_M^E}{C_b} \quad (7)$$

The lossless circuit of Figure 1 contains three circuit parameters that are specified by real numbers. This property is also shared by the equations of state, Equations (2) or (4), where three real numbers specify the coefficients. A two-port transducer with dissipation, on the other hand, in general requires three complex numbers for its specification (at a single frequency). The straightforward way



C_b = blocked capacity.

C_M^E = short-circuit compliance.

N = electromechanical transfer ratio.

Bar Dimensions

l = length. h = separation between electrodes.

A_3 = electrode area (one electrode).

A_c = cross-sectional area.

End-Electroded Bar

$$C_b = \frac{A_3 E_{33}^T}{l} (1 - k_{33}^2) \quad k_{33}^2 = \frac{d_{33}^2}{s_{33}^E E_{33}^T}$$

$$C_M^E = \frac{l s_{33}^E}{4 A_3} \quad N = \frac{2 d_{33} A_3}{s_{33}^E l}$$

Laterally-Electroded Bar

$$C_b = \frac{A_3 E_{33}^T}{h} (1 - k_{31}^2) \quad k_{31}^2 = \frac{d_{31}^2}{s_{11}^E E_{33}^T}$$

$$C_M^E = \frac{l s_{11}^E}{4 A_c} \quad N = \frac{2 d_{31} A_3}{s_{11}^E l}$$

FIGURE 1

Electromechanical Circuit of the Stiffness-Controlled
Lossless Transducer

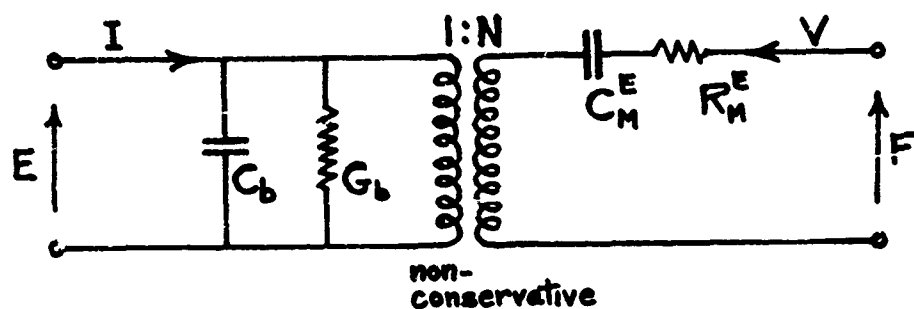
of introducing dissipation into the circuit of Figure 1 evidently is to let all three of its circuit parameters become complex. A dissipation factor $\tan \delta_b$ will be associated with the blocked capacity C_b , a dissipation factor $\tan \delta_M$ will be associated with the compliance C_M^E , and a small phase angle θ_N will be associated with the transfer ratio N . The circuit after this modification is shown in Figure 2.

The coupler of the circuit of Figure 2 is a very illegitimate circuit element. It could be called a transformer with a complex turns ratio, but it must not be confused with the complex transformer described by Carlin and Giordano.⁽¹⁴⁾ Their complex transformer is a lossless coupler; the transformation ratio for the voltage is the complex conjugate of the transformation ratio for the current. The transformer used here, however, does not have this conjugate property, and it is a nonconservative element. The phase angle of the vector power changes in going through this transformer, and the real power may either increase or decrease depending on the relative signs of θ_N and the phase angle of the vector power. A pure reactance becomes a lossy reactance after transformation; likewise a pure resistance acquires a reactive component. The resistive components generated by the transformation in some cases may be negative.

In view of the unconventional nature of the coupler a look at physical realizability conditions is perhaps advisable. The requirement that the electrical input conductance of the circuit of Figure 2 remain positive leads to the necessary condition

$$\tan \delta_b + \frac{k^2}{1-k^2} \cos \delta_M \sin(\delta_M - 2\theta_N) > 0 . \quad (8)$$

This condition sets an upper limit on θ_N . In the derivation of this equation, a



$$N = |N| e^{j\theta_N}$$

$$\begin{aligned} Y_b &= j|Y_b| e^{-j\delta_b} \\ &= G_b + jB_b \\ \delta_b &> 0 \end{aligned}$$

$$\begin{aligned} Z_M^E &= -j|Z_M^E| e^{j\delta_M} \\ &= R_M^E + jX_M^E \\ \delta_M &> 0 \end{aligned}$$

$$B_b = \omega C_b$$

$$X_M^E = -\frac{1}{\omega C_M^E}$$

$$G_b = \omega C_b \tan \delta_b$$

$$R_M^E = \frac{\tan \delta_M}{\omega C_M^E}$$

$$\begin{aligned} \tan \delta_b &= \frac{G_b}{B_b} \\ &= \frac{G_b}{\omega C_b} \end{aligned}$$

$$\begin{aligned} \tan \delta_M &= -\frac{R_M^E}{X_M^E} \\ &= \omega R_M^E C_M^E \end{aligned}$$

FIGURE 2

Electromechanical Circuit of the Stiffness-Controlled Transducer with General Dissipation

new definition of the electromechanical coupling factor k was introduced:

$$\frac{k^2}{1-k^2} = \frac{|N|^2 C_m^e}{C_b} \quad (9)$$

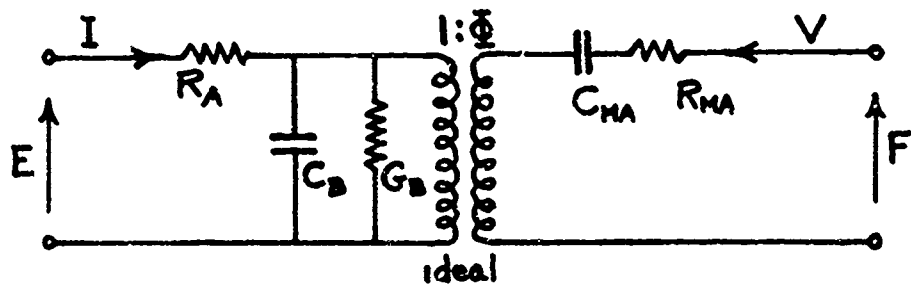
by analogy with Equation (7). There is no standard definition of the coupling factor of a lossy transducer, and Equation (9) constitutes a convenient definition for present purposes. The condition that the mechanical input resistance remain positive sets a lower limit on θ_N :

$$\tan \delta_m + \frac{k^2}{1-k^2} \cos \delta_b \sin(\delta_b + 2\theta_N) > 0 \quad (10)$$

These conditions set rather wide limits on the range of θ_N . Their only value would be for detecting gross measurement errors.

If one sets out to calculate the performance of a lossy transducer, the presence of the complex coefficient N in Equation (6) does not present any unusual difficulties. For engineers who are adept at estimating performance from circuit diagrams, however, the circuit diagram of Figure 2 leaves something to be desired because of its unfamiliar coupler. Of course, if θ_N is small, it can be ignored for most purposes and the coupler treated as an ideal transformer. A more rigorous method of eliminating the unconventional coupler is desirable, however. If a third resistance is introduced into the circuit in such a way that it does not combine trivially with G_b or R_m^e , then replacement of the unconventional coupler by an ideal transformer should be possible. The only basic requirement is that the circuit contain three independent loss parameters.

The resistance R_A in the circuit of Figure 3 evidently meets the requirements



$$R_A = \frac{-\tan \theta_N}{\omega C_b (1 - \tan \theta_N \tan \delta_b)}$$

$$G_B = \frac{\omega C_b (\tan \theta_N + \tan \delta_b - \tan^2 \theta_N \tan \delta_b - \tan \theta_N \tan^2 \delta_b)}{1 + \tan^2 \theta_N}$$

$$\approx \frac{\omega C_b (\tan \theta_N + \tan \delta_b)}{1 + \tan^2 \theta_N}$$

$$C_B = \frac{C_b (1 + \tan \theta_N \tan \delta_b)}{1 + \tan^2 \theta_N}$$

$$\Phi = |N| (1 - \tan \theta_N \tan \delta_b) \cos \theta_N$$

$$R_{MA} = R_M^E - \frac{|N|^2 \sin 2\theta_N}{2\omega C_b}$$

$$\frac{1}{C_{MA}} = \frac{1}{C_M^E} + \frac{|N|^2 \sin^2 \theta_N}{C_b}$$

FIGURE 3

Transformation of the Circuit of Figure 2 to
Eliminate the Non-Conservative Coupler

described above. The condition is imposed that the transfer ratio Φ of this circuit be a real number, and the equivalence relations between this circuit and that of Figure 2 may then be derived. The results are given in Figure 3. The algebra required to obtain these results is lengthy, but routine. R_A will be negative if θ_N is positive. Positive θ_N implies that the force generated when the transducer is blocked ($V = 0$) will lead the applied voltage, and this seems unlikely physically.

2.3 Possible Mechanical Terminations for the Transducer

The equations and circuits that have been developed above provide a background against which proposed measurements may be discussed. One of the first practical questions to consider is: What mechanical loads should be applied to the two ends of the vibrating bar? The easiest load to apply is zero load; so the exploitation of this condition will be considered first. When the transducer is vibrating freely in air it is essentially unloaded, since the radiation impedance of the bar ends is negligible compared with the bar's internal mechanical impedance. Measurements on the unconstrained bar enable three useful complex ratios to be determined: the ratio of displacement to voltage

$$\begin{aligned} \frac{S}{E} &= \left| \frac{S}{E} \right| e^{j\theta_E} = - \frac{N}{j\omega Z_M^E} \quad (F=0) \\ &= |N| C_M^E \cos \delta_M e^{j(\theta_N - \delta_M)}, \end{aligned} \quad (11)$$

the ratio of displacement to change

$$\frac{S}{Q} = \frac{V}{I} = \left| \frac{S}{Q} \right| e^{j\theta_Q} \quad (F=0), \quad (12)$$

and the ratio of voltage to current

$$\begin{aligned}\frac{E}{I} = Z_{IN} &= -j \left| \frac{E}{I} \right| e^{j\delta_{IN}} = \frac{S/Q}{j\omega(S/E)} \quad (F=0) \\ &= -j \frac{|S/Q|}{\omega |S/E|} e^{j(\theta_Q - \theta_E)} ; \quad \delta_{IN} = \theta_Q - \theta_E .\end{aligned}\quad (13)$$

Only two of these three ratios are independent. Measurement of all three will, therefore, give a check on the measurement accuracy.

To obtain a third independent measurement, and thereby determine all of the transducer circuit parameters, it is necessary to dispense with the easily obtained $F = 0$ condition and provide some other known boundary condition at the ends of the bar. The cement joint problem is then encountered; applying boundary conditions in this context inevitably involves cements. The available adhesives do not provide infinite-impedance joints, and breaking the joints when a change of boundary conditions is desired is very difficult.

The mechanical terminations that can be provided for the bar are of two basic types: active and passive. The active termination would require two identical auxiliary transducers; one would be cemented to each end of the bar. The auxiliary transducers could then provide a measured velocity input to the transducer under test. This technique appears very promising but requires considerable development to be made reliable. The trouble with passive terminations aside from the joint problem is that standard mechanical impedances are not available on the shelf, and to calibrate a mechanical impedance requires measurement of force as well as velocity. The simplest solution to this problem appears to be to aim for

infinite impedance terminations. Quarter-wave rods cemented to each end of the bar under test will approximate this condition at the one frequency for which the quarter wavelength stipulation is satisfied.

The effectiveness of the quarter-wave stubs in blocking the transducer can be judged by monitoring the velocity of the ends of the ceramic bar. If $V \rightarrow 0$, a measurement of the driving voltage and current will yield the blocked admittance

$$Y_b = \left(\frac{I}{E} \right)_{V=0} = j \left| \frac{I}{E} \right| e^{-j\delta_b} = G_b + j\omega C_b . \quad (14)$$

Subtracting the blocked admittance from the free input admittance, Equation (13), yields the motional admittance

$$Y_{\text{mot}} = Y_{\text{in}} - Y_b = \frac{1}{Z_{\text{in}}} - Y_b = \frac{N^2}{Z_M} . \quad (15)$$

By combining the measured values of the motional admittance, Equation (15), and the transfer ratio ξ/E , Equation (11), values of the magnitude and phase of N are obtained.

$$N = \frac{j Y_{\text{mot}}}{\omega(\xi/E)} = |N| e^{j\theta_N} . \quad (16)$$

Substituting these results back into Equation (15) yields the complex values of the mechanical impedance

$$Z_M^E = \frac{N^2}{Y_{\text{mot}}} = R_M^E + \frac{1}{j\omega C_M^E} . \quad (17)$$

By the method described above all of the complex circuit parameters of the circuit of Figure 2 are obtained. Then the parameters for the circuit of Figure 3 may be calculated if desired. By use of the formulas in Figure 1, generalized for dissipative conditions, the values of the coefficients in the piezoelectric equations of state, Equation (1), may be calculated. It is noted that

The loss angle of ϵ_{33}^T is δ_{IN} , Equation (13);

The loss angle of s_{11}^E or s_{33}^E is δ_M , Figure 2;

The phase angle of d_{31} or d_{33} is θ_E , Equation (11);

The phase angle of g_{31} or g_{33} is θ_Q , Equation (12).

2.4 Existing Data and Scope of Investigation

At this point a review of the available data on dissipative parameters is appropriate. The only unambiguous data that have been reported are on the free dielectric loss angle δ_{IN} . Measurements of this parameter are fairly straightforward. Small samples of material operating in their stiffness-controlled frequency range are measured in high-voltage a.c. bridges. The main precaution necessary is to avoid a significant temperature rise due to the dissipated energy. This is accomplished by applying the high field for only brief intervals and allowing long cooling periods. Clevite has published curves of $\tan \delta_{IN}$ as a function of driving field for their materials at several values of ambient temperature,⁽⁵⁾ and similar data are available from several other manufacturers. Data on the variation of the reversible permittivity ϵ_{33}^T with field are also obtained in these measurements. Both the dissipation factor $\tan \delta_{IN}$ and the permittivity increase with increasing field.

The variation of ceramic losses at mechanical resonance as a function of the a. c. stress level was measured by Gerson.⁽¹⁵⁾ He observed the resonance and antiresonance characteristics of the electrical input admittance, which are caused by mechanical resonance, and interpreted his results in terms of mechanical storage factor Q_M and compliance C_M^E . The mechanical storage factor decreased and the compliance increased as the stress level was raised. This information was of much engineering value, but the interpretation was not rigorous. Since only one complex function, Y_{IN} , was measured, a true separation of the mechanical parameters from the other parameters of the transducer was not possible. Several investigators^{(16),(17)} have suggested that phase angles of the electromechanical transfer functions had a part to play in the interpretation of their measurements on transducers. No direct measurements of these phase angles have been reported, however. For the most part their existence has been ignored by transducer designers. Ignorance of the transfer phase angles has not been an important hindrance to transducer design in the past but may be so in the future as the demands on transducer performance become more severe.

Another question to be considered is whether physical theory can provide values for the electromechanical transfer angles. The answer is negative, since ferroelectric theory is almost entirely phenomenological and is used for correlating measurements but not for predicting properties. However, it is natural, though perhaps naive, to hypothesize that the strain under quasi-static conditions is in phase with the polarization. If this were true the phase angle θ_0 (Equation (12)) would be zero, and the determination of the remaining parameters would be simplified. (It is not necessary to distinguish between polarization and electric

displacement because the dielectric constants are very high). In view of the fact that the gross polarization results from a number of different domain processes, the above hypothesis appears suspect, and verbal communication with several authorities in this field did not turn up much support for it. The results of the present investigation do not indicate that $\theta_Q = 0$ for all cases.

Two assumptions are implicit in the piezoelectric equations of state and in the network theory as employed above. These are linearity, as has been emphasized, and reciprocity. It is by virtue of reciprocity that the same d_{33} coefficient is used in both equations of the set (2) and the same N coefficient is used in both equations of the set (6). There is no evidence to cast doubt on the validity of the reciprocity assumption, though it may have to be reinterpreted under nonlinear conditions.

The adoption of the linearity assumption was prompted by convenience rather than by veracity. One consequence of the actual nonlinearity is, of course, distorted wave forms. However, the wave form distortion at fields up to values that cause surface flashovers is not very noticeable. Description of the transducer in terms of impedances therefore seems justified. For small distortion, measurements made on the filtered fundamental component provide useful engineering data. The main cause for concern is the superposition indicated in Equation (6). Measurements made under stiffness-controlled conditions will not necessarily provide useful information for other conditions where the ratio of V to E is different. Unfortunately, even to obtain the coefficients of Equation (6) requires that the ratio of V to E be disturbed. Unless superposition of the results obtained when the bar is blocked and when it is operated free (stiffness-controlled) is valid, the analysis

indicated in Equations (15), (16), and (17) will be invalid. While blocking lowers the velocity below its stiffness-controlled value (hopefully to zero), resonance operation raises the velocity above the stiffness-controlled values. The latter condition is expected to be especially inimical to successful superposition. Resolution of these questions about superposition would require a much more extensive measurement program than that undertaken here.

In the planned program, measurements are made on slender-bar vibrators. The measurements are made at a few discrete frequencies in the audio-frequency range. Use of discrete frequencies is justified by the fact that the polarization processes in the ferroelectric ceramics are known to be insensitive to frequency from the subaudible to the megacycle frequency range.⁽³⁾ At least this behavior is well established for the permittivity ϵ_{33}^T and the dielectric dissipation factor $\tan \delta_{IN}$. The observed losses are of the hysteresis type, and this means that the loss angles are independent of frequency. There are several reasons for choice of the audio-frequency range. The primary reason is that audio-frequency vibrators generate displacements large enough to be measured accurately. The displacement for a given driving field is proportional to the length of the bar, but the longer the bar the lower the resonant frequency of the gravest mode. It is advisable to operate at least an octave below resonance to be well in the stiffness-controlled region, and this operating frequency will fall in the audio range for reasonably long bars.

Another advantage of the audio-frequency range is that highly accurate electrical instrumentation, such as wave analyzers and resistance boxes, is available in this range. A third reason is that much of the Navy's sonar equipment now operates in the audio-frequency range.⁽¹⁰⁾ Since the Navy is one of the largest

users of piezoelectric ceramics, it would be well to have data applicable to their needs if an unexpected dependence of ceramic properties on frequency should eventually turn up.

The next sections of the report will treat the development of the instrumentation and measurement techniques that are required to implement the planned program. Finally, the specific transducers and the measurements made on them will be described.

III

VIBRATION INTERFEROMETRY

3.1 Introduction

The use of optical interferometers to measure small mechanical vibrations began in about 1927, and the theory of the method was presented in 1931 by Osterberg.⁽¹⁹⁾ In these methods the vibrating surface was either optically polished or had a mirror attached to it so that it could constitute one of the reflectors of the interferometer. The technique commonly used was often called the "fringe disappearance method," because at certain discrete vibration levels the interference fringes appeared to fade away into a uniformly illuminated field. The sensitivity of the method was fundamentally limited in that the lowest amplitude that could be measured was that corresponding to the first fringe disappearance. For 6328 Å light such as is used in the present project, for example, this lowest amplitude is 1210 Å, or 4.76 microinches.

Besides suffering a fundamental limit in sensitivity, the fringe disappearance method also had several other disadvantages. Only simple harmonic vibrations were covered by the theory, and there was no way of recovering the wave form of a distorted vibration from the measurement results. Also, no information on the phase of the mechanical signal was obtained. On the other hand, the early interferometer methods had the advantage that the vibration pattern of a surface vibrating in a complex mode could be observed, provided that the entire surface was

polished to be optically flat. (At the present time it appears that the capability of observing the entire vibration pattern of a surface is more conveniently obtained by holography).⁽²⁰⁾

The art of vibration interferometry was advanced substantially when electronic detection of the interferometer output was substituted for visual detection. This work was begun in the U.S.S.R. in 1952, when a photomultiplier was used to extrapolate the measurements below the calibration level established by the first fringe disappearance. In this country workers at the National Bureau of Standards adapted the Russians' method to the calibration of vibration pickups.⁽²¹⁾ Using traditional incoherent light sources, they made measurements down to 72 Å.

The next advance was brought about by the introduction of lasers into vibration interferometry. This step was reported by Defarrari and Andrews of Catholic University in a brief publication⁽²²⁾ in May 1966. Measurements down to .1 Å were claimed. Use of a laser light source not only improves the signal-to-noise ratio but also makes alignment of the apparatus considerably easier than in the older interferometry.

In the present project the interferometer initially was intended to be substantially a duplicate of the Catholic University setup. Some unpublished information on the components used by them was obtained by direct communication. To adapt the laser interferometer to the needs of the present project, however, two innovations were required: One was a control system to eliminate building vibrations from the instrument's output, and the other was a feedback system to reduce fluctuations in the laser-beam amplitude. These developments will be described in the following sections.

3.2 Theory of the Interferometer

A simplified schematic diagram of the vibration interferometer is shown in Figure 4. The CW laser emits a beam of light which is composed of plane waves having a constant polarization direction. Since the polarization direction has no influence on the operation of the apparatus, it is feasible to dispense with vectors and describe the light by the magnitude of its electric field strength. Thus, the laser emits light with field strength E_0 , and the dividing plate, which is a lightly metalized (and, therefore, partially reflecting) plane mirror, divides the laser light into two beams of field strengths E_1 and E_2 . The beam E_1 is reflected off the fixed mirror and is transmitted through the dividing plate towards the photomultiplier tube. The beam E_2 is reflected off the vibrating mirror and is then reflected by the dividing plate so that its path becomes coincident with that of E_1 in traveling towards the photomultiplier tube.

The combined beam $E_1 + E_2$ is detected by the photomultiplier tube, but first it must be attenuated so that it will not overload this tube. The beam, which is originally about 2 mm in diameter, is passed through a concave lens and expanded to about 7 mm in diameter. Then a pinhole aperture is used to admit only a small fraction of the beam's power. The laser light is further attenuated by a red filter and a diffuser before it reaches the photocathode of the photomultiplier (PM) tube. The red filter reduces the effect of room illumination to a negligible point, and the diffuser spreads the light over the photocathode surface; this diffusion is beneficial in the avoidance of fluctuations of photomultiplier gain. The current out of the photomultiplier tube is proportional to the light power admitted, and measurements made on this current will provide information on the amplitude of vibration

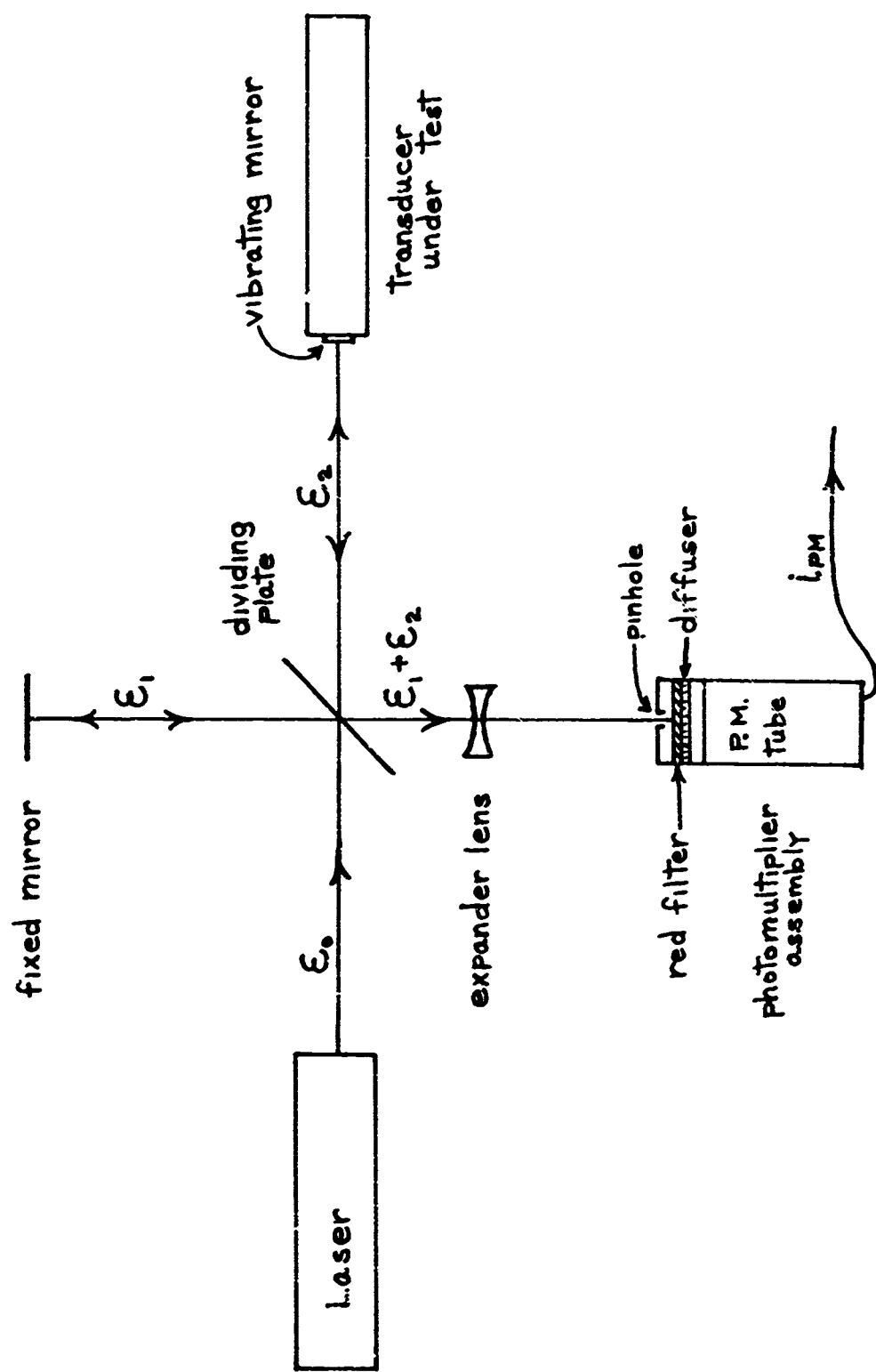


FIGURE 4
Simplified Diagram of the Vibration Interferometer

of the transducer under test and for small signals will also provide information on the phase and wave form of the vibration.

The Michelson interferometer described above may be discussed conveniently in the terminology of modern radio.⁽²³⁾ The light beam \mathcal{E}_2 upon being reflected by the vibrating mirror becomes phase-modulated by the vibration. The light beam \mathcal{E}_1 , which has the same frequency as the beam \mathcal{E}_2 but is not modulated, serves the function of a local oscillator. In recombining these two beams the dividing plate acts as a mixer, and the photomultiplier tube is a square-law detector for the combined beams. The detection of the phase-modulated signal, as carried out in this apparatus, is called homodyne detection and was invented in 1939; it never achieved popularity in radio systems.

Since laser light is highly monochromatic, the electric field strength \mathcal{E}_1 at the mixing point may be written

$$\mathcal{E}_1 = (\mathcal{E}_1)_{\max} \cos \omega_c t , \quad (18)$$

where ω_c is the angular frequency of the carrier, that is, of the laser light. It will be assured that the path lengths which the beams \mathcal{E}_1 and \mathcal{E}_2 traverse in going from the dividing plate to their respective mirrors and back differ by a distance d . Then the field strength \mathcal{E}_2 at the mixing point may be written

$$\mathcal{E}_2 = (\mathcal{E}_2)_{\max} \cos (\omega_c t + Kd) ; \quad (19)$$

where $K = 2\pi/\lambda = 2\pi/6328$, for the helium-neon laser used, with the presumption that d will be expressed in angstroms.

If the interferometer is aligned properly, the two beams will be coincident

and their wave fronts parallel at the mixing point. Hence, their combination involves only scalar addition of their field strengths. The magnitude of the Poynting vector at the mixing point is

$$\begin{aligned}
 S_m &= \sqrt{\frac{\epsilon_0}{\mu_0}} (\mathcal{E}_1 + \mathcal{E}_2)^2 \\
 &= \sqrt{\frac{\epsilon_0}{\mu_0}} \left\{ \frac{(\mathcal{E}_1)_{\max}^2}{2} [1 + \cos 2\omega_1 t] + \frac{(\mathcal{E}_2)_{\max}^2}{2} [1 + \cos 2(\omega_2 t + kd)] \right. \\
 &\quad \left. + (\mathcal{E}_1)_{\max} (\mathcal{E}_2)_{\max} [\cos(2\omega_1 t + kd) + \cos kd] \right\}, \quad (20)
 \end{aligned}$$

where trigonometric identities have been used to expand the squares and cross-products of the expressions in Equations (18) and (19).

The photomultiplier tube produces a current which is proportional to the light power

$$i = \chi \int_a S_{PM} dA, \quad (21)$$

where A is the pinhole area and S_{PM} is the magnitude of the Poynting vector at the photomultiplier input. The photomultiplier tube also acts as a low-pass filter; although its high-frequency response is very good in terms of radio frequencies, it does not pass light frequencies. The only terms in Equation (20) which survive the filtering are the d.c. terms and the $\cos kd$ term (which may vary with time). It is not important to keep track of the attenuation of the beams after mixing nor to determine the gain of the photomultiplier tube. It is sufficient to write

$$i = A + B \cos kd \quad (22)$$

and measure the parameters A and B directly.

Equation (22) is the basic equation of vibration interferometry. In practice,

building vibrations may cause the path difference d to vary; means for combating this will be described in later sections. For now it is assumed that only the test transducer will cause periodic variations in d . If the absolute displacement of the transducer face is

$$\xi = \xi_1 \cos(\omega t + \phi) , \quad (23)$$

then

$$d = d_0 + 2\xi = d_0 + 2\xi_1 \cos(\omega t + \phi) , \quad (24)$$

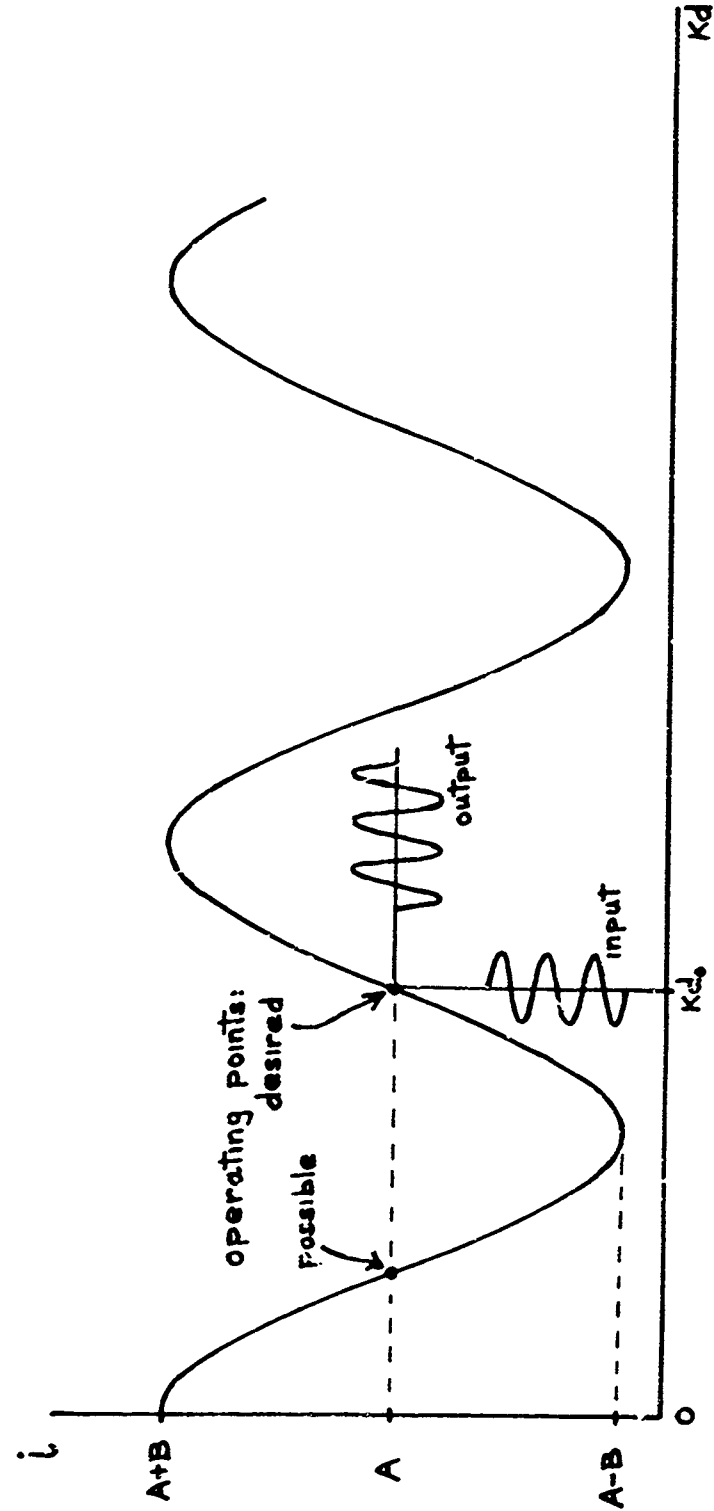
since the path lengths of both the incident and reflected waves in the divider-plate-to-transducer path will be changed by an amount ξ .

One of the great conveniences of using a laser light source is that the equilibrium value of the path difference d_0 may have almost any value. When the laser is operated at low intensities, the beam has a coherence length of many meters. With an incoherent light source, on the other hand, the equipment must be arranged so that d_0 is very small.

When Equation (24) is substituted into Equation (22), the result is

$$i = A + B \cos[Kd_0 + 2K\xi_1 \cos(\omega t + \phi)] . \quad (25)$$

This equation describes the homodyne detection process and it is illustrated in Figure 5. Evidently the best operating point is where the slope of the cosine curve is greatest (positive or negative), that is, where Kd_0 is an odd multiple of $\pi/2$. Half of the operating points so selected will give a phase reversal, which for many purposes would be unobjectionable. For the measurements intended here, however, this phase reversal should be avoided. When the operating point is set according



$$i = A + B \cos kd$$

FIGURE 5
Homodyne Detector Operating Characteristic

to these criteria, the a.c. output will be

$$\begin{aligned} i_{a.c.} &= I - I_0 = B \cos [Kd_0 + 2K\xi_1 \cos(\omega t + \phi)] \\ &= -B \sin [2K\xi_1 \cos(\omega t + \phi)]. \end{aligned} \quad (26)$$

When the signal amplitude ξ_1 is small, $\sin[2K\xi_1 \cos(\omega t + \phi)]$ may be replaced by its argument and the detection process is distortionless.

The detector saturates and clips the signal when $2K\xi_1 = \pi/2$, or $\xi_1 = \lambda/8$; with $\lambda = 6328 \text{ \AA}$ clipping occurs for $\xi_1 = 791 \text{ \AA}$. This value provides a calibration point for the equipment, since the onset of clipping, observed on an oscilloscope, can be determined rather precisely. For amplitudes greater than 791 \AA the detector has no semblance to a linear device, but it still can be used to measure amplitude. The methods used are then similar to the fringe-disappearance method but are implemented electronically. In the present project it was discovered that phase measurements in this large-signal region are also feasible.

To pursue the analysis beyond the graphical inspection of Figure 5, it is standard practice to transform Equation (25) to the form

$$\begin{aligned} i &= A + B \cos Kd_0 \cos [2K\xi_1 \cos(\omega t + \phi)] \\ &\quad - B \sin Kd_0 \sin [2K\xi_1 \cos(\omega t + \phi)] \end{aligned} \quad (27)$$

by trigonometry, and then expand the forms $\cos(x \cos y)$ and $\sin(x \cos y)$ in Fourier series. The result⁽²⁴⁾ is

$$\begin{aligned} i &= A + B \cos Kd_0 J_0(2K\xi_1) - 2B \sin Kd_0 J_1(2K\xi_1) \cos(\omega t + \phi) \\ &\quad + B \cos Kd_0 2 \sum_{m=1}^{\infty} (-1)^m J_{2m}(2K\xi_1) \cos 2m(\omega t + \phi) \\ &\quad - B \sin Kd_0 2 \sum_{m=2}^{\infty} (-1)^{m+1} J_{2m-1}(2K\xi_1) \cos[(2m-1)(\omega t + \phi)]. \end{aligned} \quad (28)$$

The Fourier coefficients are Bessel functions of the argument $2K\xi_1$.

When the operating point is set (by adjusting d) to the value shown in Figure 5, then $\cos Kd_0 = 0$ and $\sin Kd_0 = 1$. Equation (28) reduces to

$$i = A - B \left\{ 2 J_1(2K\xi_1) \cos(\omega t + \phi) + 2 \sum_{m=2}^{\infty} (-1)^{m+1} J_{2m+1}(2K\xi_1) \cos[(2m-1)(\omega t + \phi)] \right\}. \quad (29)$$

The current now contains the d.c. term $i_0 = A$, the fundamental component, and all odd harmonics. The distortion is independent of the local oscillator strength, that is, of the ratio B/A .

The fundamental component $2BJ_1(2K\xi_1) \cos(\omega t + \phi)$ may be isolated by electrical filtering. It is maximum when $\xi_1 = 926 \text{ \AA}^\circ$. This provides another calibration point. Since the maximum value of J_1 is .5819, the equation for the fundamental component at this maximum is

$$|I_1|_{\max} = 2B(.5819). \quad (30)$$

Hence, the unknown constant $2B$ (which may be considered also to absorb any attenuation of the filter) can be determined in terms of $|I_1|_{\max}$. Thus, for amplitudes less than 926 \AA° , the fundamental component of current is

$$|I_1| = \frac{|I_1|_{\max}}{.5819} J_1(2K\xi_1). \quad (31)$$

Given a measured value of $|I_1|$, one may solve this equation for ξ_1 by inverting the Bessel function. For small signals $J_1(2K\xi_1) \sim K\xi_1$, and the fundamental component becomes $i_1 = -2BK\xi_1 \cos(\omega t + \phi)$, as was predicted earlier from Equation (26).

While the interferometer can give wave form information only in the strictly linear range ($\xi_1 \ll 791 \text{ \AA}$), it should give phase information up to much higher levels. Equation (29) shows that the fundamental component of the output retains the phase ϕ of the original signal. By comparing the phase of the fundamental component against that of a reference signal in a bridge circuit, phase measurements up to 791 \AA can be made. Above that level the rapid increase of odd harmonic distortion destroys the accuracy of the bridge method, but Lissajous patterns can still be used as will be described in a later section.

For signals larger than 791 \AA , the amplitude information of the interferometer is very useful for calibrating instruments of secondary accuracy, such as the Fotonic Sensor. Quite a variety of techniques are available for this large-amplitude range. One method is to keep $\cos Kd_o = 0$ so that Equation (29) applies and follow the output of a filter tuned to the fundamental frequency as the vibration amplitude is raised. The filter output will trace out the first-order Bessel function curve $J_1(2K\xi_1)$. The successive zeros of this curve make especially good calibration points.

Instead of using a narrow-band filter tuned to the fundamental, one can use a d.c. meter as a low-pass filter. From Equation (28) the output is then seen to be

$$I_o = A + B \cos(Kd_o) J_0(2K\xi_1) . \quad (32)$$

In this case d_o should be adjusted so that $\cos Kd_o = 1$. As the vibration amplitude is raised, the meter reading varies in accordance with the zero-order Bessel function curve $J_0(2K\xi_1)$. The successive maxima and minima provide good calibration points, if they are not masked by building vibrations.

Maintaining $\cos Kd_0$ at the desired values (unity in one case, zero in the other) is difficult because drift tends to be pronounced. The drift may not cause too much trouble if only the maxima and minima of the Bessel functions are being determined; however, if a continuous calibration is being attempted as the vibration amplitude is raised, drift will present a severe problem. At Catholic University the present approach is to use two narrow-band filters, one tuned to the fundamental, the other to the 3rd harmonic. In Equation (28) it is seen that both these terms contain the factor $\sin (Kd_0)$; when the ratio of the two terms is taken, the result will be independent of d_0 and hence not affected by drift. Thus:

$$\frac{|I_3|}{|I_1|} = \frac{J_3(2K\xi_1)}{J_1(2K\xi_1)} \quad . \quad (33)$$

From the measured ratio of 3rd harmonic to fundamental, one may solve for the vibration amplitude ξ_1 .

3.3 Setting Up and Adjusting the Interferometer

The first requirement for an interferometer setup is a stable worktable. The setup here began with a standard laboratory bench with a 2-1/4-inch-thick wooden top. On top of this was placed a layer of sponge rubber 1-3/4 inches thick and on top of the rubber a steel plate 1 inch thick. The steel plate was 5-1/2 feet long by 2-1/3 feet deep, weighed 700 pounds, and had a planed upper surface. The laboratory bench was stiffened with diagonal crossbraces and its legs were padded to make even contact with the floor.

The steel plate had been used before at the U. S. Navy Underwater Sound Laboratory for visual interferometry using the fringe-disappearance method and it

appeared to provide sufficient stability. In the new setup at the University of Connecticut, however, definite deficiencies were noted. The main reason for this difference is that interferometers using photomultipliers demand much more stability, since they measure much smaller amplitudes than the older methods and their output must be steady enough to permit filtering and measurement by electronic instruments. Another reason is that the building vibrations on the third floor of the Engineering II building at University of Connecticut appear substantially greater than in the previous first floor location at the Underwater Sound Laboratory.

The sponge-rubber, steel-plate system constitutes a low-pass filter. Building vibrations below about 20 Hz. were transmitted through this filter with sufficient amplitude to be disturbing. The desirability of the large marble benches often seen in interferometer setups thus became clear, but no such bench was available. The present bench setup was made workable only by development of an automatic control system to remove building vibrations from the instrument's output. Even with a better bench and a better location, this control system would probably retain its value for achievement of ultimate stability.

3.3.1 Major Components

The major components used in the implementation of the system shown in Figure 4 will now be discussed.

The laser is a Perkin-Elmer Model 5200 helium-neon laser with a Model 5203 power supply. Its rated output is 1.3 milliwatts in the TEM_{∞} mode at 6328 \AA . This power is more than ample. Two other lasers were tried: a Perkin-Elmer 5200

with a Model 5202 power supply and a Spectra Physics 130. Surprisingly, the light output of these lasers was amplitude-modulated with 60 Hz hum, the modulation being as high as 30 percent. This hum causes the coefficients A and B in Equations (28) and (29) to vary with time; the result is that the hum causes intermodulation of the desired fundamental signal component. The disturbing effects of the hum are thus not simply corrected by filtering it from the output of the system. When the laser with the better power supply (Model 5203) was obtained, the hum problem disappeared. With this disturbance out of the way, it was then discovered that the laser output power fluctuated as much as 10 percent, the period of the fluctuation being of the order of seconds. The fluctuation could not be attributed to the power supply, since the latter was very well regulated. A control system was developed to greatly reduce the extent of this fluctuation.

An interferometer carriage that was originally part of a Gaertner I-333 Vibration Interferometer was available. On this carriage is mounted the dividing plate and fixed mirror. The fixed mirror actually has 3 degrees of freedom. It can be translated by a very precise transport screw in order to adjust the path difference d_0 . The mirror can be tilted in two planes by two thumbscrews with very fine threads; these adjustments are to make the wave fronts in the two interfering beams parallel. The transport screw is seldom used in the present setup. Although it has a fine thread and a vernier control, it is not really capable of setting d_0 with the precision required in the present application. A piezoelectric transducer is used to translate this mirror in conformity with the Catholic University setup. This transducer is also a key component in the control system used to eliminate building vibrations from the interferometer's output.

The two beams which recombine at the dividing plate and proceed towards the photomultiplier strike a mirror which changes their direction by 90°. This is done to conserve space in the layout of the equipment. The beams then pass through a plano-concave lens of -77 mm focal length and diverge over a distance of 25 cm before reaching the pinhole in front of the photomultiplier.

The photomultiplier tube is an RCA type 7265, and it is mounted in a housing manufactured by Pacific Photometric Instruments which bears the model designation 62/2F. The power supply is Model 1544 of Power Designs Inc. The manufacturer of the photomultiplier tube recommends that its output current not exceed .25 mA. when maximum stability is desired. To achieve this condition the power supply voltage is kept low (about 1600 volts) and the light beam is heavily attenuated. The sensitivity of this photomultiplier apparently is much greater than is required for the present application.

At the forward end of the photomultiplier housing an aluminum foil cover with a pinhole is mounted. Behind the pinhole a Kodak F-29 red filter is placed to discriminate against room illumination. A layer of fogged camera film is inserted to further attenuate the light and then a layer of 20 pound-weight bond paper to act as a diffuser. Without the diffuser the photocathode is illuminated only over a spot about a millimeter in diameter, and since this surface can not be expected to be of uniform sensitivity, a slight movement of the light spot might result in a change in the output current.

In Figure 4 the components which must be most rigidly mounted to the base plate are the fixed mirror, the dividing plate, and the transducer under test since it is these components that set up the interfering beams and determine the path

length difference d_o . Mounting of the laser, the expanding lens, and the photomultiplier is much less critical. The interferometer carriage is sealed to the base plate with paraffine. The mounting for the transducer under test will be described in detail later; a heavy carriage is used with 3 thumbscrews acting as legs. The piezoelectric ceramic sample must be compliantly mounted to its carriage in order that it may vibrate piezoelectrically; hence, it is susceptible to excitation by building vibrations if they are transmitted to the base plate. The fixed mirror is also susceptible to vibrations since its adjustable mounting is not very secure. A better mounting than the present one could probably be designed.

3.3.2 Alignment Procedure

In the mathematical analysis presented earlier it was assumed that the two interfering beams proceeding towards the photomultiplier had coincident paths and parallel wave fronts. The two beams may be observed visually at the face of the photomultiplier housing on the diaphragm containing the pinhole. At this point the beams have been expanded enough so that their details may be observed. If the alignment conforms to the assumptions of the analysis, a bright spot will be seen with no interference fringes. If d_o is varied by translating the fixed mirror, the spot will vary cyclically from bright to dark but will retain its uniformity with no interference fringes appearing. This phenomenon differs from that observed with the traditional Michelson interferometer, which uses spherical waves rather than plane waves. There, perfect alignment is indicated by circular interference fringes. The laser interferometer resembles rather the Twyman interferometer,⁽²⁵⁾ which uses collimated beams.

In setting up the laser interferometer one will, in general, observe two light spots, one from the fixed mirror and one from the mirror on the transducer under test. By using the tilt controls on the fixed mirror the two spots may be brought into coincidence, but interference fringes will probably be seen. Further adjustment of the fixed mirror will eliminate the fringes. The latter step amounts to obtaining parallel wave fronts at the expense of separating the beam axes slightly; i.e., not having complete overlap. If the two spots are noticeably nonoverlapping, the transducer carriage should be moved to a new position on the table and the fixed mirror again adjusted to eliminate fringes. In these trials only the two mirrors need be moved; the angle of the dividing plate with respect to the beams is of no concern.

The alignment of the laser interferometer actually proceeds very rapidly. In the trial and error procedure described one is guided by watching secondary reflection spots. Perfect alignment usually requires that the secondary reflections be aligned with the primary beams. However, such precise alignment is not necessary and may be undesirable since secondary interferences from surfaces such as the laser face will be set up.

When the alignment is so poor that interference fringes develop, this indicates that the path difference d_o varies with position over the viewing screen. To include this situation in the analysis, let x and y be the coordinates of the viewing screen, and let the wave fronts of one beam be parallel to the viewing screen. The wave fronts of the other beam are inclined an angle θ_1 from the x -axis and an angle θ_2 from the y -axis. Then for small angles the path difference may be expressed as

$$d_0 = d_\infty + \theta_1 x + \theta_2 y \quad (34)$$

To use the previously developed equations, (20) through (28), under these new conditions it is necessary merely to employ the new expression for d_0 in Equation (34). The magnitude of the Poynting vector, Equation (20), now varies with x and y (mapping out the fringes), and account of this must be taken in the integration of Equation (21).

Both theory and experiment show that the interferometer will operate satisfactorily with fringes present as long as the pinhole diameter at the photomultiplier entrance is considerably less than the fringe width. When d_0 is varied by translating the fixed mirror, the fringes will move across the screen. When the operating point is set correctly, the pinhole will be halfway between the centers of a bright and a dark fringe.

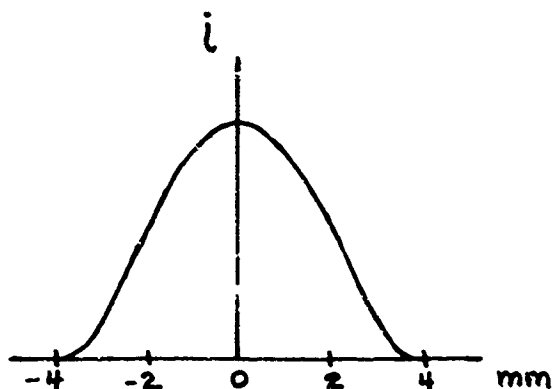
3.3.3 Choice of Pinhole Size

The limit on pinhole diameter mentioned above is not a stringent one, and the question remains open as to what the best pinhole size should be. While the pinhole plays an important part in attenuating the light, there are other attenuators in this system; so its size is not entirely determined by this function. As far as discrimination against room illumination goes, the pinhole size is not the important factor but rather the size of the expanded laser beam. The laser light intensity should be large compared with room illumination at the photomultiplier entrance; excessive beam expansion will militate against achievement of this condition. The pinhole provides equal attenuation for both components of the incident light. With

regard to sensitivity of the setup to building vibrations, examination of the theory failed to show any influence of pinhole size on this property.

Initially the equipment was operated with very small pinholes (about .2 mm diameter). The wisdom of this choice seemed doubtful when careful inspection of the expanded laser beam showed that it has a pronounced microstructure of light and dark spots. It was thought that less fluctuations might be observed if the pinhole were large enough to sample a substantial area of this microstructure; as a result the very small pinholes were abandoned. Experiments in which almost the whole laser beam was admitted to the photomultiplier did not show any dramatic decrease in fluctuations, however.

When the expanded laser beam was scanned with a very small pinhole, its intensity across the beam was found to be very nonuniform. Figure 6 below shows how the photomultiplier current varied as the pinhole was moved along a diameter of the laser spot. In this experiment there were no interfering beams as only one mirror of the interferometer was in use. The peaking of intensity at the center



Profile of Expanded Laser Beam

FIGURE 6

may be partly due to the characteristics of the expander lens. However, experiments with multiple lenses arranged to recollimate the beam did not result in any marked improvement. While the waves emitted by the laser have plane wave fronts of constant phase, they do not have the uniform intensity along these fronts that is often considered to be a collateral property of plane waves.

Figure 6 shows the desirability of having the laser and photomultiplier and their accessories quite rigidly mounted even though they are not directly involved in the setting up of interference paths. If the beam should wander appreciably over the pinhole, the output of the interferometer will fluctuate in accordance with Figure 6. The pinhole diameter that was finally selected was 1.6 mm. The portion of the laser beam utilized is still small but much larger than in the initial setup. The attenuation that was lost in going to the larger pinhole was made up by including two layers of fogged photographic film in the system.

3.4 A Control System for Stabilizing the Operating Point

As shown in Figure 5, it is necessary to maintain the equilibrium value of the path length difference d_o constant in order to obtain an output from the interferometer that has minimal distortion. The proper operating point for d_o is shown in this figure, and the analysis of Equation (28) confirms that d_o should be maintained at a value which makes $\cos Kd_o = 0$. In practice, d_o tends to drift badly as building vibrations disturb the equipment.

In order to have precise control in setting d_o , the fixed mirror is mounted on a piezoelectric transducer. Varying the d.c. voltage on this transducer will cause translation of the mirror, thus varying the path length of the local oscillator beam.

When the path length drifts from its proper value, it can be reset by changing the voltage on the transducer. Readjustment appears necessary several times a minute with the present installation; therefore, an automatic system is obviously desirable.

Besides contributing to drift, the building vibrations introduce much low-frequency noise into the system. When conditions are poor, the noise components can drive the homodyne detector all the way to saturation; that is, to the peaks of the cosine curve of Figure 5. Even under favorable building conditions the noise components will cause excursions over 40 percent of the dynamic range of the detector. The effects of this noise can not be eliminated simply by electrical filtering of the interferometer output. The noise components intermodulate with the signal, and the signal even after filtering has random fluctuations in amplitude. It is thus apparent that a path-length control system should be designed to eliminate not only quasi-static drift but also low-frequency noise fluctuations.

By using negative feedback from the output of the photomultiplier to the transducer which controls the "fixed mirror," it is possible to keep this mirror moving in such a way that it removes the fluctuations in path length (that is, in d_o) that tend to be introduced by building vibrations. Of course, this negative feedback must be rendered ineffective at the higher frequencies at which measurements are to be made; the test transducer will also introduce fluctuations into the interference path when it is driven, but these constitute the desired signal. The troublesome building vibrations lie below 100 Hz and the measurements on the ceramic vibrators are planned to be made at frequencies above 1 kHz; therefore, a decade of frequency is available for the transition from full control to no control.

3.4.1 Description of System

Figure 7 shows the control system that is used. The photomultiplier tube, which is a constant-current generator, feeds current i_{PM} into the system at the left of the diagram. The current flows through a RC network where it develops a voltage e_{PM} , which may be applied to an oscilloscope, and also supplies a signal to a comparison bridge, which is used for precise measurements. The adjustable condenser C_p in this circuit is to provide some phase shift which was found to be necessary for the bridge circuit, and the $.1 \mu F$ condenser is to keep the d.c. out of the bridge. The bridge circuit will be described in detail in a later section. The current is delivered next to the input of the control system.

A large bypass condenser ($1 \mu F$) is used at the input of the control system to keep the voltage at this point, e_e , a small fraction of the total measured voltage, e_{PM} , at high frequencies. A d.c. reference current is supplied by the 1.5-volt dry cell battery in series with the $6.8 K\Omega$ and $2 K\Omega$ resistors. When the photomultiplier current is equal to this reference current, the error voltage is zero and the control system is quiescent. The reference current is approximately $.2 \text{ mA}$, which is close to the maximum photomultiplier current that is recommended when highly stable operation is desired. The detector operating point may be varied somewhat by adjusting the $2 K\Omega$ rheostat. The controlled operating point current corresponds to the constant A in Figure 5. To set the operating point correctly a vibration signal is supplied by the test transducer and its level is raised until the detector begins clipping. The reference current is then adjusted until symmetrical clipping is achieved.

The servo amplifier is a Philbrick Model UPA-2 operational d.c. amplifier.

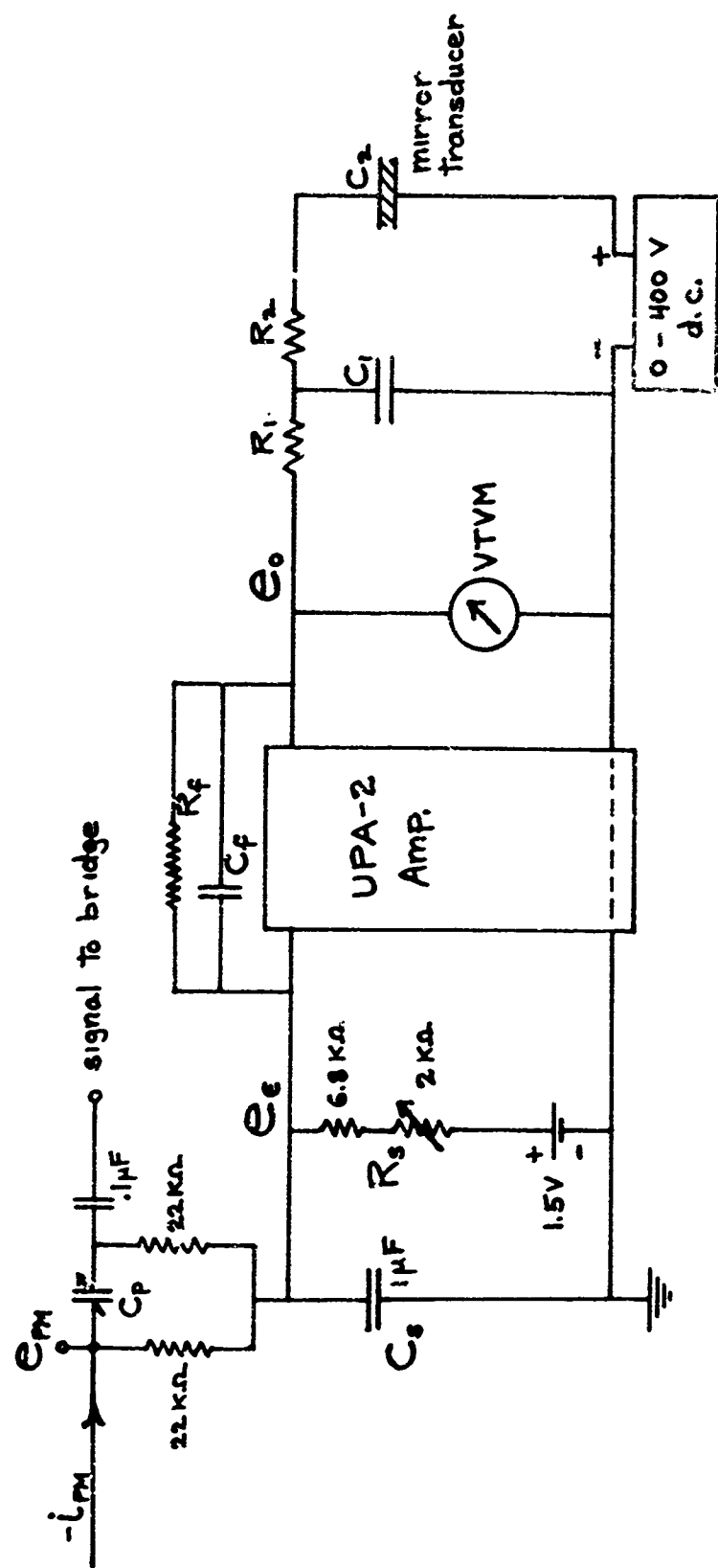


FIGURE 7
Control System for Stabilizing the Operating Point

It works in conjunction with a Phillbrick Model R-100B power supply. The amplifier operates with a local feedback loop formed by the elements R_f and C_f . Its output voltage swings over a ± 115 -volt range. The amplifier output is monitored by a vacuum tube voltmeter and occasionally by an oscilloscope. An RC filter, which includes the mirror transducer as one of its components, is used in the output circuit to attenuate high frequencies. The input admittance of this transducer in the range of interest is that of a slightly lossy condenser. The 400-volt power supply is placed in series with the amplifier and transducer. Its function is to set the operating point initially before the servo system takes control. The d.c. voltage is readjusted occasionally as the system drifts to keep the average amplifier output, as read on the VTVM, near zero.

When the photomultiplier current begins to differ appreciably from the reference current, the amplifier will deliver a voltage to the mirror transducer, which will cause the mirror to move and change the path difference d_o so as to bring the detector back to its original operating point. Depending on the polarity of the connections to the mirror transducer, the control system may be made to lock on to either an operating point on the negative slope of the detector characteristic curve or to an operating point on the positive slope of this curve; see Figure 5. The latter is the one that is used since nothing would be gained in having the detector invert the phase of the signal.

3.4.2 Design Objectives

The primary object of the control system is to reduce building vibration and drift components of the detector's input to the point where they do not appreciably

affect the signal component by intermodulation. From inspection of Figure 5, it was judged that keeping fluctuations in the operating-point current below 5 percent of the total dynamic range of the detector would be sufficient. Equation (28) can be used to obtain a rough quantitative check of this estimate. In this equation the constant A represents the desired value of the operating-point current; the d.c. drift component is given by the second term:

$$I_{\Delta} = B \cos(Kd_0) J_0(2K\xi_1) ; \quad (35)$$

and the fundamental component of current is given by the third term:

$$I_1 = 2B \sin(Kd_0) J_1(2K\xi_1) . \quad (36)$$

At the operating point $\cos(Kd_0) = 0$ and $I_{\Delta} = 0$, but for 5 percent drift $\cos Kd_0 = \pm .05$, if small signal conditions are assumed; i.e., $\xi_1 \rightarrow 0$. The corresponding value of $\sin Kd_0$ is .125 percent less than unity; hence, the fundamental component of current given by Equation (36) is reduced .125 percent due to the drift of the detector. This amount of intermodulation is considered tolerable.

Besides reducing the fundamental component of current the detector drift will cause even harmonics (the 4th term in Equation (28)) to appear. This is not a serious effect, for odd harmonics are already present, and during precision measurements filtering will be used. Equation (35) shows that large signals will reduce the drift current relative to the value that it has in the absence of signal. The maximum signal that will be used in homodyne detection is $\xi_1 = 926 \text{ \AA}$ as this value makes $J_1(2K\xi_1)$ maximum. The corresponding value of $J_0(2K\xi_1)$ is .317; therefore, Equation (35) shows that the reduction in drift current is 68 percent.

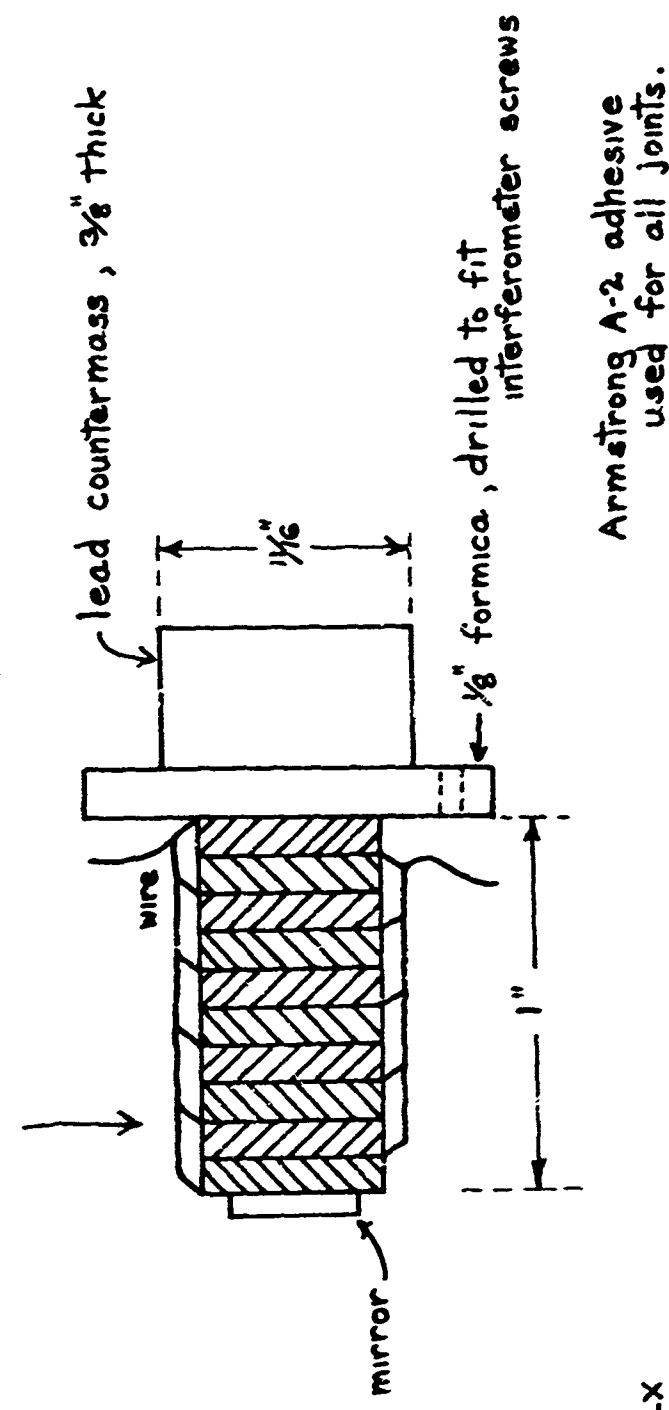
Graphical considerations support these conclusions; unsymmetrical clipping caused by drift will produce a d.c. component which opposes the original drift current. This drift current reduction is undesirable when the control system is operating, for the drift current given by Equation (35) is the error signal that actuates the control system. If the drift current is controlled within 5 percent when $\xi_1 = 0$, it will probably be controlled only within 15 percent when $\xi_1 = 926 \text{ \AA}$. Then the amount the fundamental component of current is reduced by the drift will rise from .125 percent to 1.1 percent.

The control system must be designed to cause no appreciable motion of the fixed mirror in the signal-frequency range; that is, above 1 kHz. The photomultiplier detector responds to the difference in motion of the two mirrors, and there is no practical way to determine and correct for motion of the "fixed mirror." Even a small motion of the fixed mirror could cause an error when measuring the phase of the test transducer, since the two mirrors might be vibrating in quadrature at some frequencies. Another design objective is to keep $e_\epsilon \ll e_{PM}$ in the signal-frequency range; see Figure 7. The voltage e_ϵ is a function of the feedback current as well as the photomultiplier current and, hence, its phase may be quite different from i_{PM} . The calibration procedure that is used will illuminate this potential error, but operation will be more straightforward if the effect is small.

3.4.3 Mirror Transducer

Figure 8 shows a sketch of the transducer used to move the "fixed mirror." The active elements are lead titanate zirconate disks manufactured by Clevite Corporation. They are wired in parallel, and the resulting capacity is .0052 μF .

stack of 10 PZT-4 disks, .10" thick, .5" dia.



Scale: 2X

Armstrong A-2 adhesive
used for all joints.

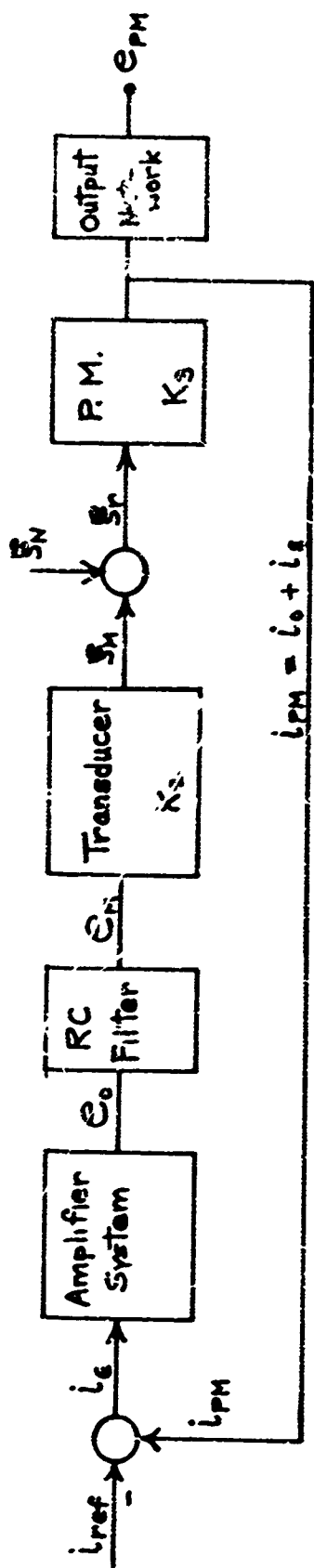
FIGURE 8
Mirror Transducer for Adjusting Interferometer Path Length

The original Gaertner interferometer had a very thick mirror inset in a metal mirror mount. The space originally occupied by this mirror is now occupied by a lead countermass, which helps to make the mounting plane a nodal plane. The new mirror is positioned an inch forward of the old location by the ceramic stack. It is not necessary to use a thick mirror with the laser beam because bending distortions are not noticeable over the 2 mm region that is illuminated.

The fundamental resonance of the mirror transducer (longitudinal mode) is at 49 kHz. Over the frequency range of use the displacement response of the transducer to constant voltage should be flat. The mounting system, however, is not ideal and causes weak resonances at 370, 1630, and 2000 Hz. The response rise at these resonances is only about 1 db, but the phase shift contributed by the 370 Hz resonance was noticeable when the final adjustments on the control system were made. The transducer calibration, with the resonant frequencies excepted, was determined by the interferometer to be 28 \AA/volt . This agrees well with the calculated value using the published piezoelectric constant. Since the amplifier's output range is ± 115 volts, the dynamic range of the control system is $\pm 3200 \text{ \AA}$. This is sufficient for all building disturbances that result from full daytime activity. A previous transducer that gave one-third this dynamic range was considered not fully satisfactory.

3.4.4 System Analysis

A block diagram of the control system is shown in Figure 9. At the summing point at the left the photomultiplier current is compared with the d.c. reference current, which is set to the desired operating-point current i_o , usually .2 mA.



- i_{ref} = d.c. reference current $\approx .2$ mA.
- i_{pm} = photomultiplier output current.
- $i_c = i_{pm} - i_{ref}$; $i_{ref} \approx i_o$.
- C_o = output voltage of UPA-2 Amplifier.
- e_m = voltage applied to mirror transducer.
- ξ_m = $K_x C_m$ = displacement of mirror.
- ξ_n = displacement of either interferometer mirror due to mechanical noise.
- $\xi_r = \xi_m + \xi_n$ = relative displacement of the two mirrors.
- $i_c = K_a S_r$ for small signals.
- C_{pm} = output voltage of interferometer system.

FIGURE 9. Block Diagram of the Control System

The resulting error current i_e actuates the amplifier system shown in Figure 7. The amplifier output, after filtering, drives the mirror transducer to produce a mirror displacement ξ_M . The transducer has a transmission constant K_2 of 28 \AA/volt . It has no appreciable inertia in the frequency range of interest. A disturbance ξ_N of the interferometer path length is shown entering the system at the summing point on the right of the diagram. If the motion of the driven mirror ξ_M is able to completely cancel out this disturbance, there will be no relative displacement ξ_r actuating the photomultiplier tube. But, of course, cancellation is not complete and the resulting disturbance of the photomultiplier is fed back to the amplifier, thus completing the loop.

A gain constant K_3 for the photomultiplier is defined for small signals: $K_3 = i_e / \xi_r$. The small-signal approximation is justified throughout the frequency range where the control system is effective since a small i_e is an objective of the control. In order to evaluate K_3 the homodyne detection equation will again be examined. From Equations (25) and (26) the detector characteristic with the operating point properly set is seen to be

$$i_{PM} = A + B \sin[2K\xi_r \cos(\omega t + \phi)] . \quad (37)$$

The constant B may readily be determined by measuring the peak current at the clipping point ($\xi_r = 791 \text{ \AA}$), for at this point $\sin[2K\xi_r \cos(\omega t + \phi)] = 1$. It is found that $B = A = .2 \text{ mA}$. The equality of the coefficients A and B indicates that the dividing plate was very accurately coated and that the two mirrors have retained equal reflectivity. The equation for the error current magnitude is

$$I_e = (i_{PM} - i_e)_{\max} = 2 \times 10^{-4} \sin(2K\xi_r) \quad (38)$$

and for small signals

$$K_3 = \frac{I_e}{S_r} = (2 \times 10^{-4})(2K) = 3.97 \times 10^{-7} \text{ Amp/}\text{A} . \quad (39)$$

The gain constant K_3 depends on the setting of the laser intensity control, on the voltage setting of the photomultiplier's power supply, and on the attenuation of the pinhole and other elements in the optical path. It is also influenced by any failure of the two laser beams to be exactly centered on the pinhole in accordance with Figure 6. However, all these factors work together to determine $i_o = A = B$, and all one has to do to maintain constant K_3 is to see that i_o always has the same value (normally .2 mA). In practice, the slight readjustments that have to be made to restore i_o to its chosen value are conveniently done by varying the photomultiplier's supply voltage. A more subtle factor influencing K_3 is intermodulation. As explained earlier, if a large high-frequency signal is being measured by the interferometer, it will reduce the error current below that given by Equation (38) and thereby effectively reduce K_3 . However, the initial gain of the system can be made high enough so that this gain reduction is tolerable.

Two complementary closed-loop characteristics are of interest: the response of the system to a disturbance

$$\frac{I_e}{S_N} = \frac{K_3}{1 - K_3 H} , \quad (40)$$

and the disturbance rejection function

$$\frac{\tilde{S}_M}{S_N} = \frac{K_3 H}{1 - K_3 H} . \quad (41)$$

Here H is the open-loop transfer function of the system

$$H = \frac{E_M}{I_\epsilon} . \quad (42)$$

The ideal behavior for Equation (41) would be for it to be unity in the control region ($f < 100$ Hz) and zero in the signal region ($f > 1000$ Hz). In the latter region ξ_N changes its role from a disturbance to a signal.

The transfer function H is partitioned into a number of factors:

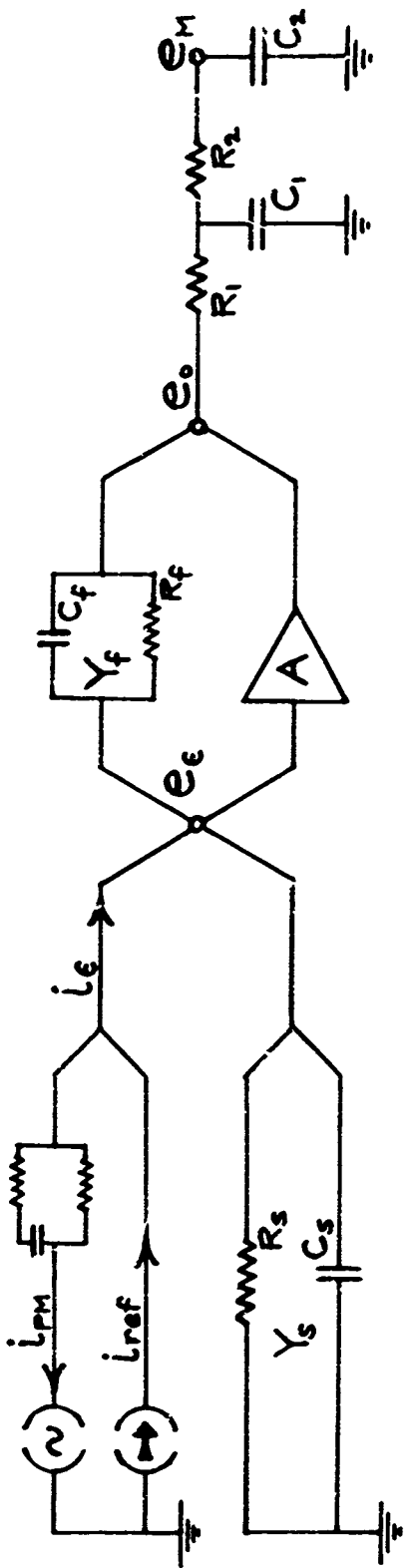
$$H = (K_2) \left(\frac{E_M}{E_o} \right) \left(\frac{E_o}{I_\epsilon} \right) . \quad (43)$$

K_2 is the transmission constant of the mirror transducer and has already been evaluated. The factor E_o/E_M is the voltage transfer ratio of the RC filter, and E_o/I_ϵ is the transfer impedance of the amplifier system. The optimization of these transfer functions was carried out experimentally by observing their effect on the closed-loop characteristics, defined by Equations (40) and (41). Although design was done experimentally, analysis was carried out also to ensure that the operation of the system was properly understood.

As an aid to analysis, the circuit diagram of Figure 7 has been redrawn in Figure 10. The branch which supplies the reference current (consisting of R_s and a battery) has been represented as a current source with shunt conductance by use of Thevenin's theorem. The nodal equilibrium equation for the e_ϵ node is

$$I_\epsilon + Y_f(E_o - E_\epsilon) - Y_s E_\epsilon = 0 . \quad (44)$$

By use of the relation $E_o = AE_\epsilon$ and rearrangement of terms, the transfer impedance is obtained:



$$i_e = -i_{PM} + i_{ref}$$

$$Y_s = G_s + sC_s \quad ; \quad G_s = \frac{1}{R_s} \quad . \quad T_s = \frac{C_s}{G_s}$$

$$Y_f = G_f + sC_f \quad ; \quad G_f = \frac{V_{R,f}}{G_f} \quad .$$

$$A = \text{gain of UPA-2 amplifier.} \quad S = \sigma + j\omega$$

Symbols

a.c.
current
source

FIGURE 10
Redrawn Control System Diagram

$$\frac{E_o}{I_e} = \frac{-A}{Y_f(A-1) - Y_s} \quad . \quad (45)$$

The manufacturer gives the following expression for the gain of the amplifier:

$$A = \frac{-K_1}{1 + sT_1} \quad \text{with } K_1 \approx 10^8, T_1 \approx 24 \text{ sec.} \quad , \quad (46)$$

and it has been found to apply to the particular amplifier on hand. The amplifier has a built-in -6 db/octave slope, starting at a frequency of .0066 Hz.

When Equation (46) is substituted into Equation (45), the result can be expressed as

$$\frac{E_o}{I_e} = \frac{-K_1 R_s}{T_1 T_2 (s - s_a)(s - s_b)} \quad , \quad (47)$$

where

$$T_2 = \frac{C_p + C_s}{G_f + G_s} \approx \frac{C_s}{G_s} = T_s \quad . \quad (48)$$

The transfer impedance has two poles on the negative real axis. The general expressions for these poles in terms of the circuit parameters are quite complex. However, by experimentation values of certain parameters were fixed and the useful ranges of variation of others were narrowed down. Mathematical approximations could then be carried out, and the following approximate expressions for the poles were obtained:

$$s_a \approx -\frac{K_1 \frac{G_f}{G_s}}{K_1 \frac{C_f}{G_s} + T_1} \quad , \quad s_b \approx -\frac{K_1 \frac{C_f}{G_s} + T_1}{T_1 T_s} \quad . \quad (49)$$

Increasing the feedback capacity C_f will move the lower pole s_a downward and the upper pole s_b upward in frequency. However, s_b can be moved in the

opposite direction by increasing the shunt capacity C_s , thereby increasing T_s .

Final choices of circuit parameters resulted in the following set:

$$K_1 = 10^8, \quad T_1 = 24 \text{ sec. (amplifier properties)}$$

$$R_s = 10 \text{ k}\Omega, \quad C_s = 1 \mu\text{F}, \quad T_s = 10^{-2} \text{ sec.}$$

$$R_f = 10 \text{ M}\Omega, \quad C_f = .002 \text{ to } .005 \mu\text{F}.$$

The feedback capacity of C_f , a plug-in unit, was kept variable. If the system in some situations showed a tendency to oscillate, increasing C_f was the most convenient cure for this trouble. Normally, $C_f = .003 \mu\text{F}$ is a high enough value to ensure stability, and in the calculations which follow this value is used. The poles, or break frequencies, of the transfer impedance are then at 5.35 Hz and 2000 Hz.

It did not appear possible to realize the objective of making the gain of the system negligible at 1 kHz by using only the poles s_c and s_d , even if they were moved to more favorable locations. Therefore, the RC filter was added at the amplifier output to introduce two more real-axis poles. The voltage transfer ratio of this filter is

$$\frac{E_M}{E_o} = \frac{1}{T_1 T_2 (s - s_c)(s - s_d)}, \quad (50)$$

where

$$T_1 = R_1 C_1, \quad T_2 = R_2 C_2.$$

The poles are given by the expression

$$s_{c,d} = s_0 \left[-1 \pm \sqrt{1 - \frac{2}{s_0 \left[T_1 \left(1 + \frac{C_f}{C_1} \right) + T_2 \right]}} \right], \quad (51)$$

where

$$s_0 = \frac{T_1 \left(1 + \frac{C_2}{C_1}\right) + T_2}{2 T_1 T_2} .$$

These poles were moved around a great deal in an effort to optimize the closed-loop response. At this point the seemingly insignificant minor resonance of the mirror transducer at 370 Hz made its presence felt. The closed-loop pole had a tendency to stick at 370 Hz rather than follow changes in the open-loop poles that should have moved it through this region. However, it was eventually decided that at or slightly below 370 Hz was an excellent location for the closed-loop pole. The final choices for the filter were:

$$R_1 = 10\text{ k}\Omega , C_1 = 0.069 \mu\text{F} , T_1 = 6.9 \times 10^{-4} \text{ sec.}$$

$$R_2 = 22\text{ k}\Omega , C_2 = 0.0052 \mu\text{F} , T_2 = 1.14 \times 10^{-4} \text{ sec.}$$

$$f_c = 213 \text{ Hz.} , f_d = 1540 \text{ Hz.}$$

By combining Equations (39), (43), (47), and (50) and inserting the various numerical data given above, an expression for the complete open-circuit transfer function is finally obtained:

$$\frac{S_M}{S_r} \approx K_3 H$$
$$= \frac{111}{(1 + 2.98 \times 10^{-2} s + 2.4 \times 10^{-6} s^2)(1 + 8.57 \times 10^{-4} s + 7.86 \times 10^{-8} s^2)} \quad (52)$$

Calculations show that the gain $|K_3 H|$ falls to unity at 320 Hz; therefore, one may expect a resonant rise in the closed-loop response in this frequency region if the phase margin is low, as indeed it is. Other calculations from Equation (52) will be presented in conjunction with the discussion of the experimental curves below.

3.4.5 Measured Characteristics

To measure the closed-loop characteristics one of the test transducers was used as a source of mechanical signal. The one actually selected was the 5-inch barium titanate bar shown in Figure 24. The displacement response of such a bar to constant-voltage drive is flat in the frequency range of present interest, except for a few barely noticeable resonances due to the mounting system. These resonant frequencies were known and were avoided in taking the data on the control system.

Figure 11 shows the response of the mirror transducer when a constant-displacement vibration signal is introduced into the interferometer path by the test transducer. The response actually measured was that of the voltage on the mirror transducer E_M ; the calibration curve of the mirror transducer (which is essentially flat) was then used to convert E_M to ξ_M . A General Radio Type 1900-A wave analyzer was used to measure E_M . The measured curve corresponds to the magnitude of the theoretical expression in Equation (41). Figure 11 shows that the control system has the general features desired: Below 70 Hz the mirror displacement ξ_M has a magnitude equal to that of the applied displacement ξ_N (hence, the two displacements cancel); above 1 kHz the mirror displacement is very small compared with the applied displacement. In between these two frequency regions overshoot occurs; the mirror displacement becomes considerably greater than the applied displacement.

Figure 12 shows the relative response of the photomultiplier output current to a constant-displacement vibration signal. The mechanical signal was generated in the same way as for the measurements given in Figure 11. The output current was measured with the aid of a Pearson Electronics Model WBCT-110 current

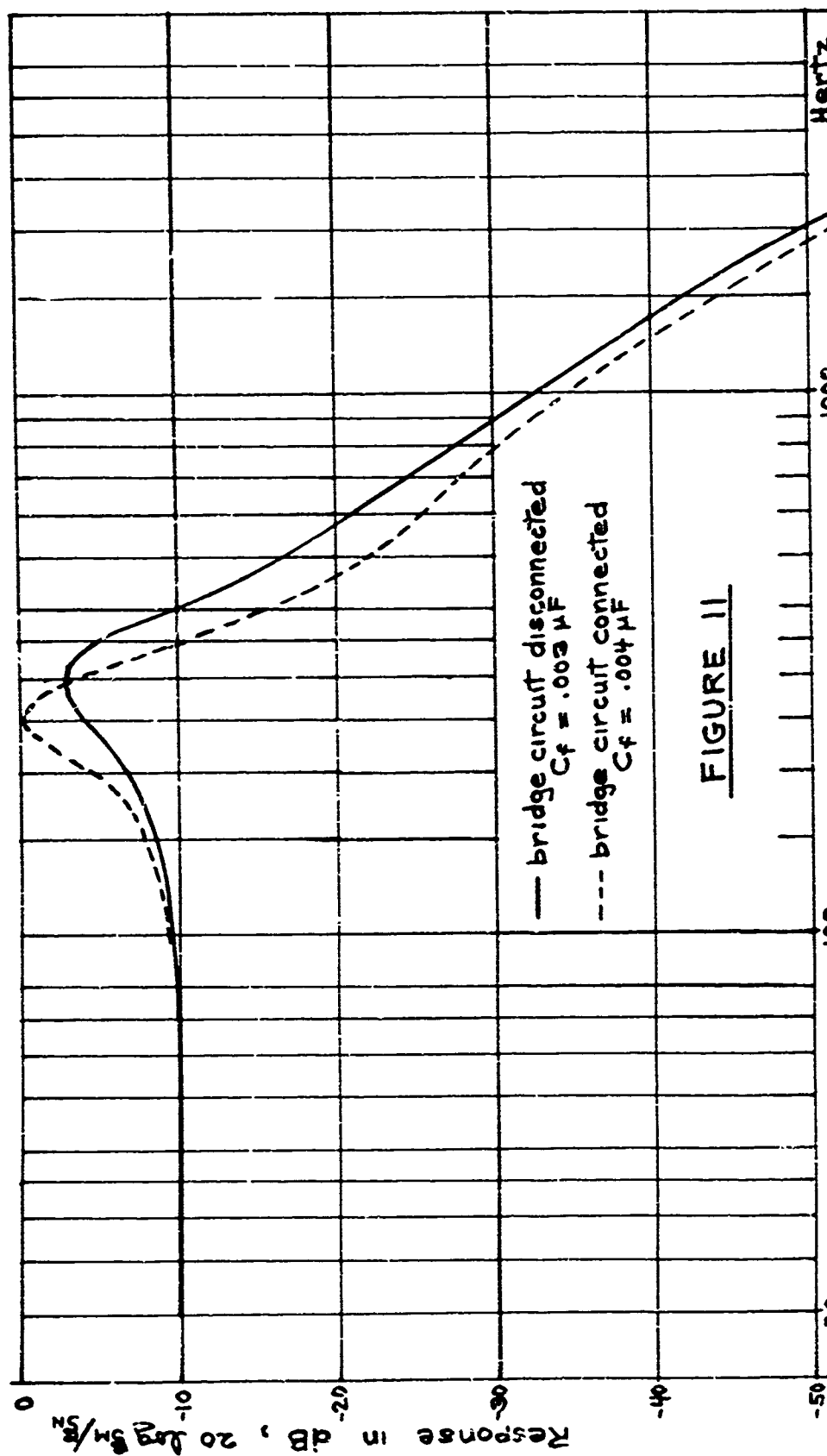
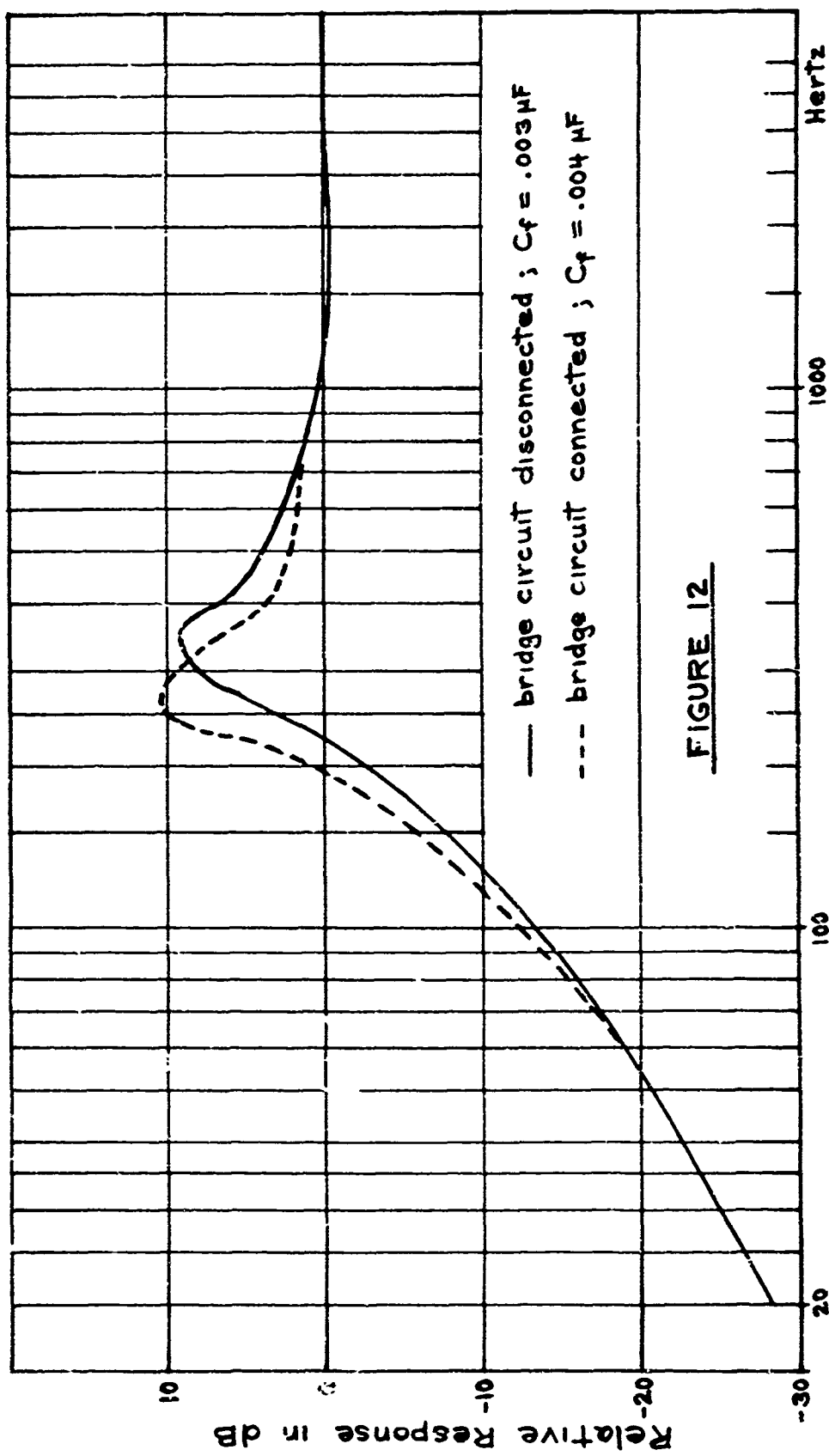


FIGURE 11
Closed-Loop Response of the Mirror Control System
to a Path-Length Disturbance



Relative Current Response of Interferometer to Mechanical Displacement of Constant Amplitude

transformer, which linked the photomultiplier current at the point where it entered the control system. The plotted response is normalized with respect to the high-frequency, flat portion of the curve. It corresponds to the magnitude of the theoretical expression $1/(1 - K_3 H)$ and thus is closely related to Equation (40).

Figure 12 is most useful for evaluating the system in the control region, $|K_3 H| \gg 1$, and Figure 11 is most useful for evaluating it in the signal region, $|K_3 H| \ll 1$. For example, Figure 12 shows that at 20 Hz the response of the measuring system to a disturbance is 28.5 db below what it would be in the absence of the control system. The corresponding figure calculated from Equation (52) is 29.2 db. A similar calculation indicates that at d.c. the response is down 40.9 db, but no corroborating measurement was attempted. The solid curve of Figure 11 shows, for example, that at 2 kHz the vibration of the mirror is 39.2 db below the level of the vibration that one is trying to measure. The calculated value from Equation (52) is 37.5 db.

The dashed curves of Figures 11 and 12 show the effects on the control system of connecting the interferometer output to the bridge circuit that is used to obtain precise measurements of the amplitude and phase of the signal. These results are not unique but depend on the setting of the bridge decade boxes and its associated phase shifter. The plotted curves show the worst case that was encountered in using the equipment. The dashed curves show not only the direct effect of connecting the bridge but also reflect the fact that the feedback capacity had to be increased from .003 μ F to .004 μ F to keep the system from oscillating. The reason that these effects exist is evident from Figure 7. Connection of the bridge circuit diverts part of the alternating component of the photomultiplier current, i.e.

away from its principal path, which includes the input to the servo system. When the bridge is balanced, the current it draws from the interferometer system becomes negligible at the signal frequency, but at other frequencies the bridge continues to draw current which would be delivered to the control system if the bridge were disconnected.

3.4.6 Input Impedance at Signal Frequencies

Another characteristic of the control system that is of some importance is its input impedance at signal frequencies. Ideally this impedance should be low compared with that of the photomultiplier's load circuit (about $11 \text{ K}\Omega$); in which case $e_e \ll e_{PM}$. Some variations in e_e might be expected as the servo system is driven toward saturation by low-frequency vibrations, and one would like these variations to be an insignificant component of the total voltage e_{PM} .

By use of Equation (44) and the relation $E_o = AE_e$ an expression for the input admittance is obtained:

$$Y_{in} = \frac{I_e}{E_e} = Y_s - Y_f(A-1) \quad . \quad (53)$$

Substitution of Equation (46) into Equation (53) yields

$$Y_{in} = Y_s + Y_f \left(\frac{K_1}{1+sT_1} + 1 \right) \quad . \quad (54)$$

The first term is due to the passive components of the input circuit while the second term is the active-circuit admittance. For frequencies greater than 1 Hz, $|sT_1| \gg 1$, and for frequencies less than 10 kHz, $|A| \gg 1$. In between these limits Equation (54) simplifies to

$$\begin{aligned}
 Y_m &= Y_s + \frac{K_1 Y_f}{s T_1} = G_s + s C_s + \frac{K_1 G_f (1 + s T_f)}{s T_1} \\
 &= \frac{1}{R_s} + s C_s + \frac{1}{R_a} + \frac{1}{s L_a} \quad . \quad (55)
 \end{aligned}$$

The input admittance may be represented by the parallel RLC circuit shown in Figure 13.

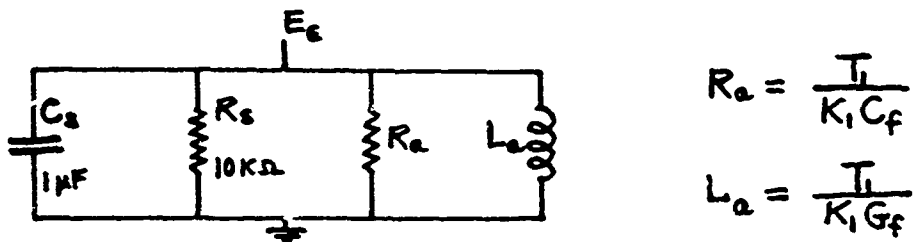


Figure 13

Circuit Representation of the Input Admittance

When the chosen values of the feedback elements ($G_f = 10^{-7}$ mhos, $C_f = .003 \mu F$) are employed, the active-circuit elements are found to be: $R_a = 80.6 \Omega$, $L_a = 2.4 H$.

The maximum value of the input impedance, which occurs at 103 Hz, is 80.6Ω .

The effect of the shunt capacity in reducing this impedance does not become appreciable (-3 db) until the frequency reaches 2 kHz. The installation of the shunt condenser C_s was motivated initially by the fact that smaller values of C_f were used, resulting in more objectionable values of R_a . While its presence now seems less important, it still serves to stabilize the input impedance in the event that amplifier overload occurs. The theoretical predictions were confirmed by direct measurement of E_e . At 2 kHz, E_{PM} was about .5 percent of E_e , and it dropped with increasing frequency.

Two ways in which the control system and the signal-measuring system interact have been noted above: (1) the voltage E_e , which is influenced by current

feedback, is a component of the measured voltage E_{PM} ; (2) the signal-measuring circuit diverts some of the error current from the control system. In principle, these interactions might be avoided completely by rearranging the circuit. One way would be to move the ground connection so that the control system would operate on current returning from ground to the photomultiplier (i.e., operate the photomultiplier E_ϵ volts above ground). This modification was tried but too much hum was introduced into the control system. Another isolation method is to obtain the signal output from a current transformer which links the photomultiplier current. This was also tried, but a high-gain amplifier had to be added to bring the signal up to its former level, and it was felt that the possibility of phase shift and gain fluctuation in the amplifier negated the advantage of avoiding the small interaction effects that occurred in the adopted setup.

3.4.7 Evaluation of the Control System

In comparing the performance obtained from the control system with the design objectives, it is concluded that sufficient control has been achieved to keep intermodulation of the signal by building vibrations to a satisfactorily low level, and that degeneration at signal frequencies has been kept low. With respect to the latter factor, the mirror motion at 1 kHz has dropped only to 8.6 percent of the signal amplitude, which is not very good; so the lower bound on signal frequencies for accurate measurements has to be pushed up to 2 kHz (mirror motion = 1.1 percent of signal). The overshoot of the control system in the 200-400 Hz range might appear to be very troublesome but it is not actually so. The filtering action of the control system and the filtering action of the rubber-supported base-

plate complement each other; spectral components of vibration which might excite the control system resonance are blocked by the base plate.

To demonstrate that the control system resonance is not excited significantly rough spectral measurements were made of the vibration components in the photomultiplier current. The test transducer was undriven electrically during these measurements, and the interferometer was operating under the conditions of the dashed curve of Figure 12. The results may be thought of as the product of this response curve and the spectrum of building vibrations after base-plate filtering. The measurements were made with the G.R. 1900-A wave analyzer set for 10 Hz bandwidth. The meter speed was set on Slow below 150 Hz and on Medium above 150 Hz. Several runs were made during the daytime, and after averaging and smoothing the results shown in Figure 14 were obtained. Although the control system resonance does produce the expected boost in the spectrum, the contribution of this portion to the total noise power is not very significant. The peak in the 70 Hz region is due to the fact that the suspension resonance of the test transducer occurs at this frequency.

When the photomultiplier current was observed broadband on an oscilloscope, the peak fluctuations due to building vibrations covered about 10 percent of the detector's dynamic range during noisy periods and fell as low as 3 percent during quiet periods. Sinusoidal oscillations at 70 Hz were often observable, but the major components appeared to be frequencies less than 20 Hz, which is the lower-limit of the wave analyzer results; see Figure 14. It is concluded that during quiet periods the desired objective of keeping fluctuations to no more than 5 percent of the detector's dynamic range is achievable, and that the control system

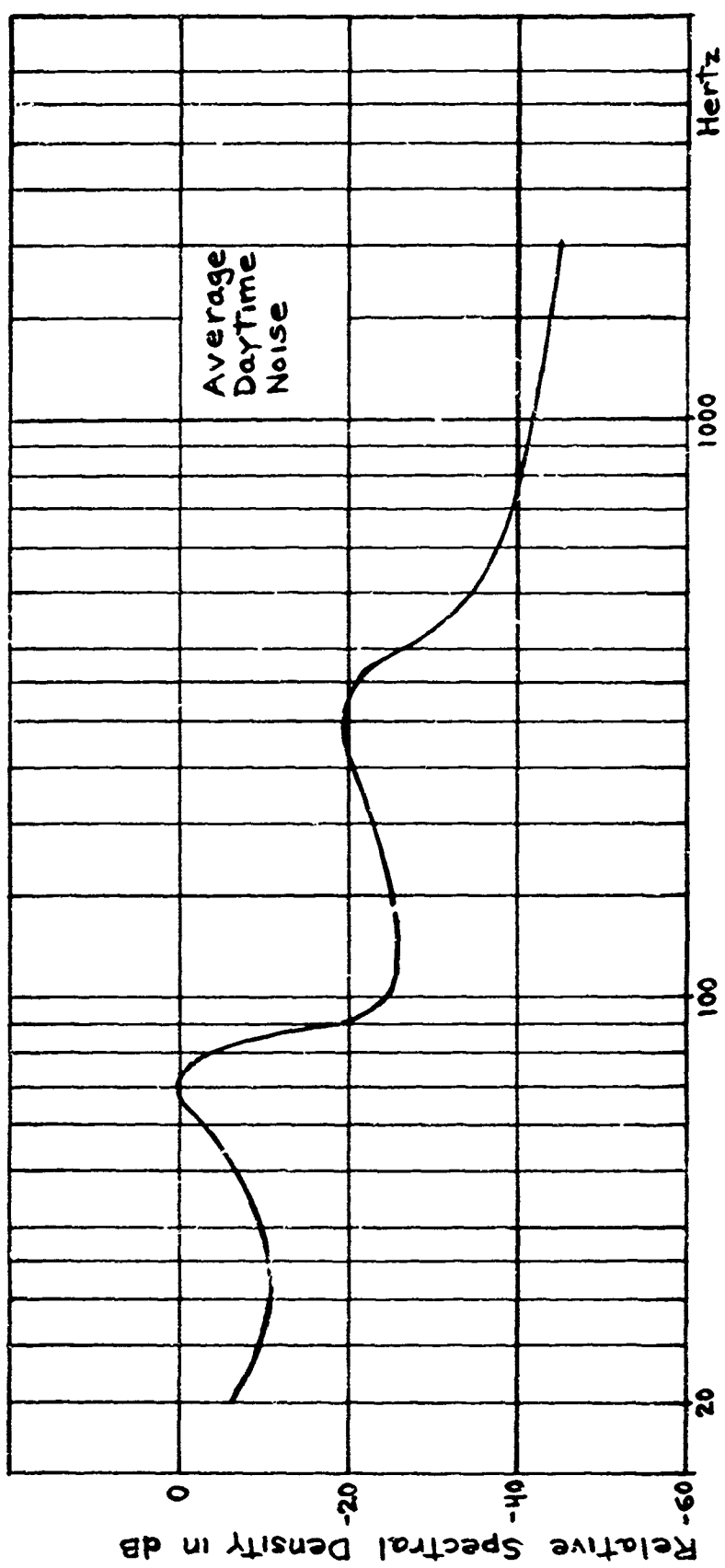


FIGURE 14
Relative Spectrum of Noise Output of Interferometer

resonance is not an important factor in this regard. The latter result is fortunate because to reduce the resonant rise significantly would require either sacrificing low-frequency gain or allocating more of the frequency spectrum to the transition region between full control and no control.

3.5 Laser Amplitude Control

After the effects of building vibrations were largely eliminated, as described above, good oscillographic displays of the signal from the test transducer were obtainable. Passing the photomultiplier output through a high-pass filter removed the traces of building vibration that had survived the control system. However, when precision measurements of the interferometer signal in a bridge circuit were attempted, fluctuations were noticed which prevented achievement of a good null. These fluctuations had periods of the order of seconds, and hence were not due to vibrations nor did they correlate with the drift which the path-length control system was counteracting. Measurements of the direct laser beam, with no interfering beam present, showed that the laser intensity fluctuated over about a 10-percent range. Since in Equation (29) the coefficient B is proportional to the light intensity, the homodyne detector output is amplitude-modulated by the laser fluctuations as well as phase-modulated by the signal. To achieve an immunity to amplitude modulation analogous to that enjoyed by FM radio receivers, it would be necessary to precede the photomultiplier detector with optical clippers or limiters, but such optical devices are not commonly available.

The laser fluctuation was not attributable to its power supply, which was very well regulated. A long warm-up time helped somewhat but the fluctuations usually

remained in excess of 5 percent. From other laser users it was learned that this behavior was normal. Since prospects for effecting any basic improvement in the laser did not appear promising, it was decided to use negative feedback to try to alleviate this condition.

The Perkin-Elmer Model 5203 power supply used with the laser has provisions for amplitude modulation of the light beam. The specifications state that up to 50 percent modulation is possible from 100 Hz to 10 kHz. For present purposes, however, quasi-static modulation was desired. The reason for the 100 Hz lower limit was found to be the presence of a small transformer in the modulation signal channel. The transformer could not be bypassed because its function is to transfer the modulating signal from ground level to a control circuit that is at a potential of 3000 volts with respect to ground. It was decided to use an a.c. control signal that would be transmitted by the transformer, but then to modify the power supply by inserting a rectifier and filter on the high-potential side of the transformer.

Figure 15 shows the circuit used to provide negative feedback from the laser's output to the regulating circuit of its power supply. Its general mode of operation is as follows. A silicon photodiode monitors the laser light, and the voltage generated by the photodiode is compared with a reference voltage derived from a battery. Subtraction of these two d.c. sources results in a small d.c. control signal. This small signal is chopped to form a 60 Hz square wave, which is amplified by a.c. amplifiers and transmitted to the modulation terminals of the laser power supply. In the power supply the 60 Hz control signal passes through the isolation transformer, is rectified and filtered, and then is introduced into the regulating circuit which controls the laser current.

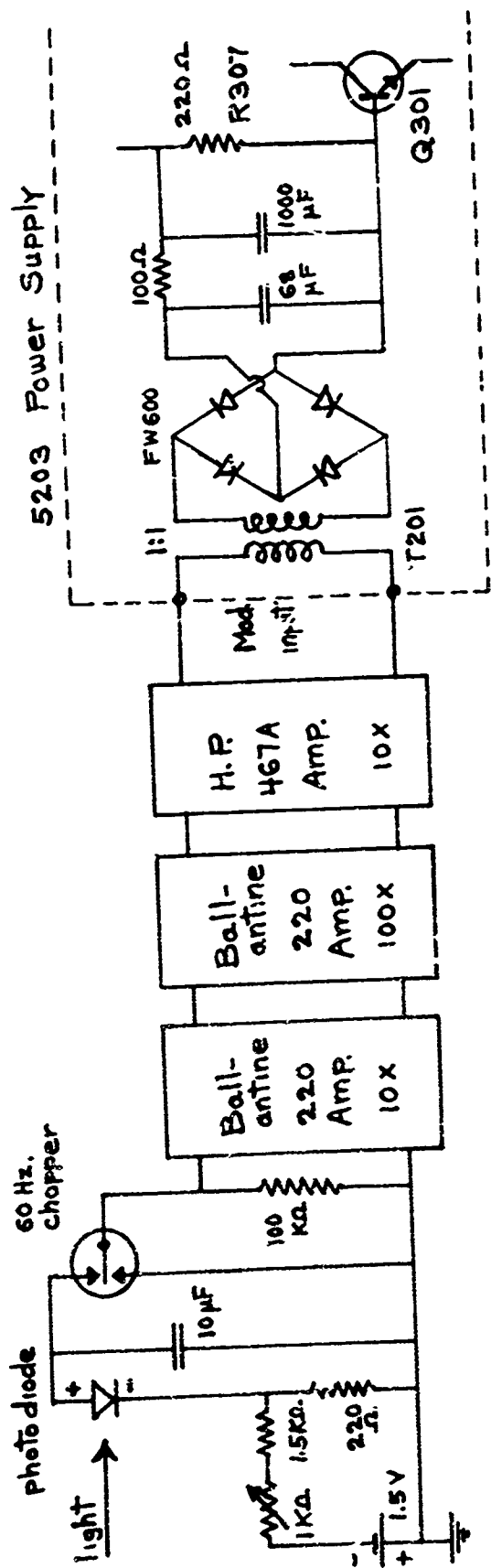


FIGURE 15
Feedback System to Stabilize Laser Intensity

Increasing the amplitude of the 60 Hz square wave control signal will drive the laser current downward, thus decreasing the light intensity. The system is adjusted so that the photodiode voltage is always greater than the reference voltage subtracted from it. A spontaneous increase in light intensity will, therefore, increase the magnitude of the control signal and corrective action (decrease of laser current) will ensue. A decrease in light intensity likewise will initiate appropriate corrective action, but if the photodiode voltage should drop to the point where it is smaller than the reference voltage, then the feedback will change from negative to positive (the control signal will increase if the photodiode voltage continues to fall). In other words, this feedback system is incapable of sensing a change of sign of the error signal. Rather than locking the laser output to some predetermined reference value, the feedback system acts merely to reduce the magnitude of the fluctuations, and the error signal never reaches or passes through zero.

The setup for monitoring the intensity of the laser beam is shown in Figure 16. The Gaertner interferometer carriage has a compensator plate mounted on it in addition to the dividing plate. The compensator plate was required when an incoherent light source was used, but normally it would serve no purpose in laser interferometry. However, in the present setup, it conveniently furnishes a light signal for the photodiode monitor. The compensator plate has no reflective coating like the divider plate but it nonetheless produces a strong reflection. Actually both plates produce three clearly seen reflected beams as shown in Figure 16; the strongest beam in each case is utilized.

The photodiode is a Texas Instruments SIV-7112 silicon diode of the generating type (no bias required). It is a flat plate with approximate dimensions

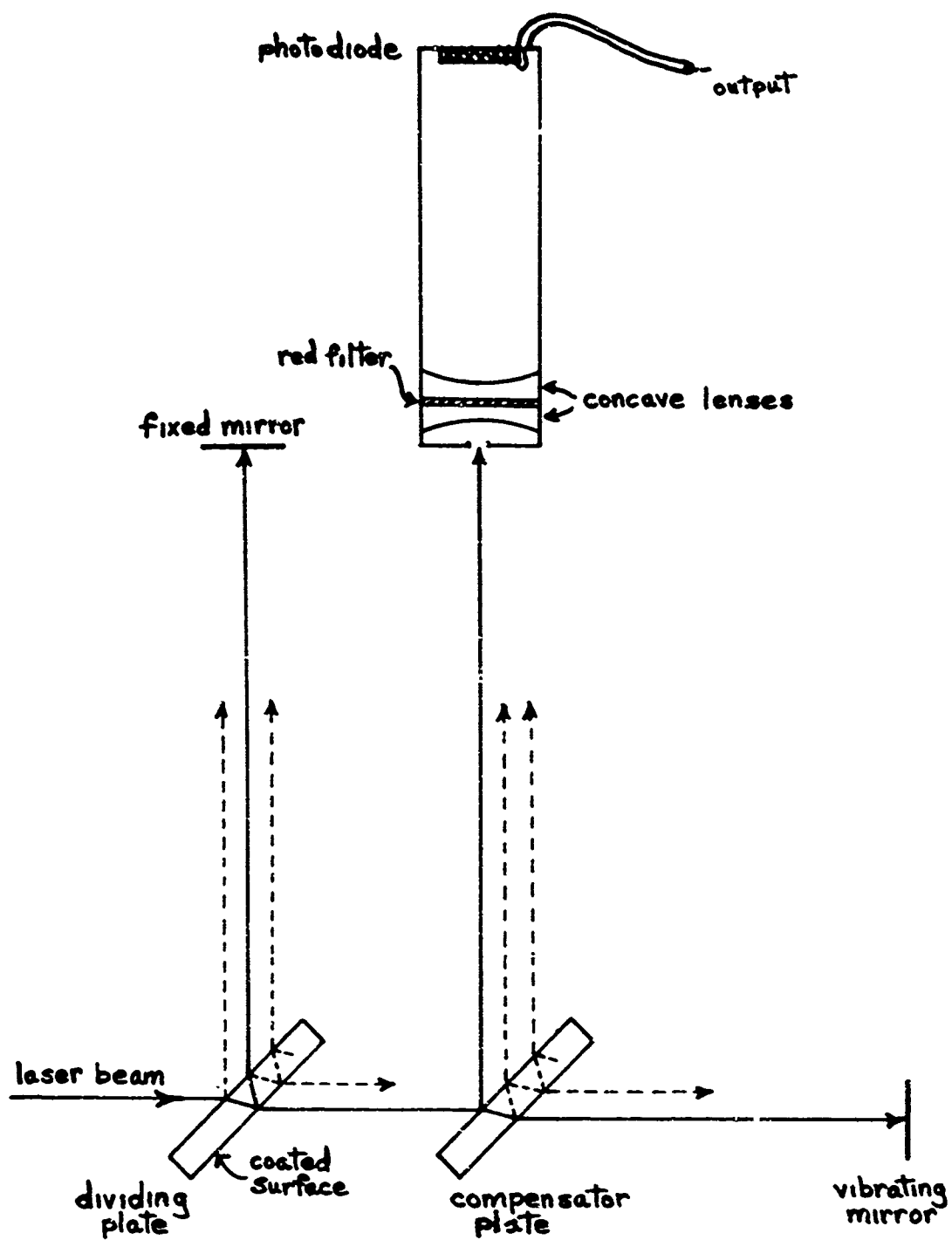


FIGURE 16
Paths of Primary Beam and Laser Monitor

1-1/2 x 2 cm. The diode is mounted at the end of a cylindrical enclosure, and the other end of the enclosure has a 2-mm-diameter hole to admit the laser beam. The beam is passed through a red filter, used to discriminate against room illumination, and through expander lenses to distribute it over an appreciable portion of the diode plate. The output of this detector is .18 volt when receiving the laser beam and is negligible when receiving only ambient light. The voltage generated by the photodiode drops rapidly when a load is applied; as a result the 10 μ F storage condenser shown in Figure 15 was added to hold the voltage up across the top of the square wave. The 100 K Ω resistor across the amplifier input was needed to reduce switching spikes.

The three amplifiers give a total voltage gain of 10^4 ; the last one is a power amplifier since it must work into a load of a few hundred ohms. In the laser power supply the secondary of the transformer T201 was originally connected directly across the resistor R307, which is a component of the transistor regulating circuit. The modifications that were necessary are shown in Figure 15.

This feedback control system is a nonlinear one because of the presence of the rectifiers that are required to demodulate the 60 Hz square wave. If the control signal approaches zero, the effectiveness of the control greatly diminishes. The system is therefore adjusted so that it always operated with a control signal of at least 2 volts peak at the output of the amplifier chain.

The fluctuations in the laser intensity, measured in terms of photomultiplier output current, could be kept down to 1 percent by use of the feedback system. Further improvement appears not easily achievable. If the amplifier gain is increased, instabilities occur, evidenced by sudden extinguishment of the laser.

The present system was developed empirically with no knowledge of the internal characteristics of the laser. Further stabilization of the laser's output would require a more fundamental study of the problem.

The laser-intensity-stabilization system cooperates with the control system for stabilizing the detector-operating point, described in the previous section, and improves its performance. The latter system reacts to laser fluctuations by changing the path-length difference d_0 so as to keep the operating current i_0 constant. It thus translates amplitude fluctuations into phase fluctuations. While this effect is not large, its reduction by the stabilization of the laser output is a desirable improvement.

3.6 Performance of the Interferometer

The various refinements described above were aimed mainly at optimizing the system for operation in the quasi-linear range of the homodyne detector; that is, for vibration amplitudes up to 791 \AA . Amplitude measurement within 2 percent accuracy is possible down to about 10 \AA . Phase and wave form information is also easily obtainable in this range with phase accuracies better than one degree under favorable conditions. For measurements below 10 \AA , steps to minimize the electronic noise of the laser and photomultiplier must be taken, but such low-level measurements were not required for this project.

When the vibration amplitude exceeds 791 \AA , the measurement procedures change considerably. Use of the control system for stabilizing the interference-path length often remains advantageous, but the system has more difficulty in maintaining control at high levels. Amplitude and phase measurements up to about $15,000 \text{ \AA}$ may be made.

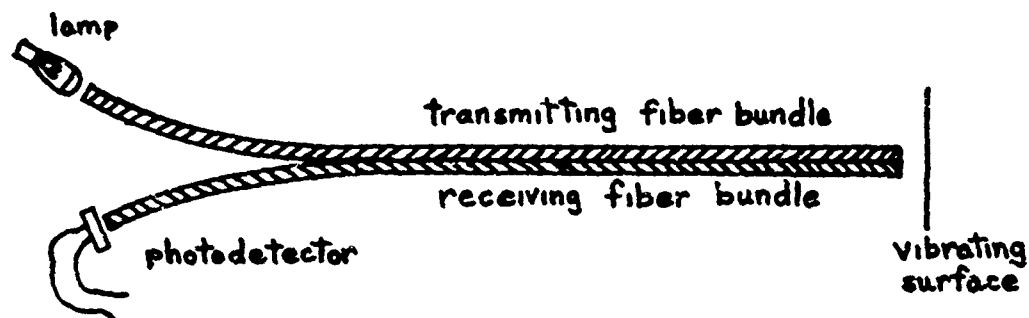
IV SENSORS USING OPTICAL-FIBER BUNDLES

For measurements above 791 \AA , an instrument with a linear response is needed to complement the interferometer, which has a grossly nonlinear relation between input and output in this high amplitude range. The interferometer remains the primary standard, giving amplitudes in terms of the wavelength of light, but the secondary instrument is useful for giving a measurable signal which has the wave form of the original vibration.

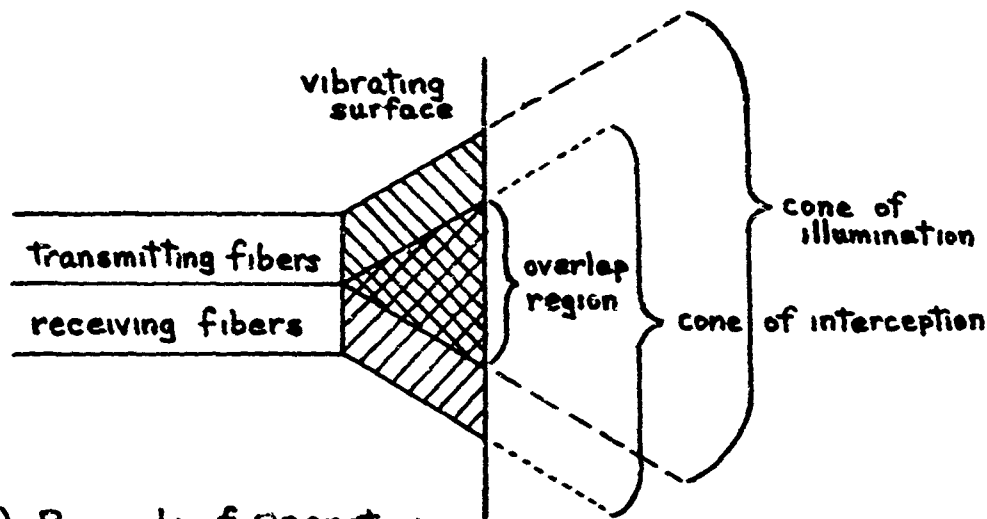
4.1 The Fotonic Sensor

An instrument called the Fotonic Sensor, manufactured by Mechanical Technology, Inc., was selected for the role of secondary instrument. The mode of operation of this instrument is shown in Figure 17. Two bundles of optical fibers are used, one to transmit light to the vibrating surface and the other to return reflected light to a photodetector. In this method the reflecting area is not made optically flat as it is for the interferometer, but high reflectivity is desirable. A piece of aluminum foil cemented to the ceramic vibrator is very satisfactory.

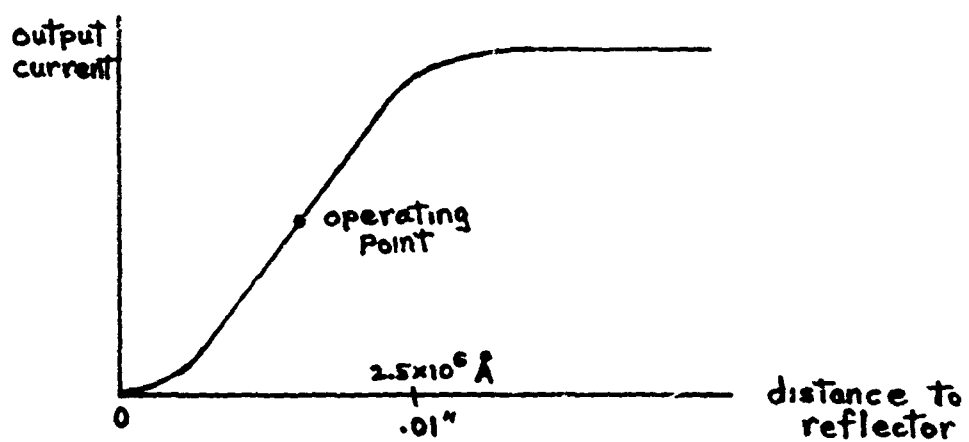
The radiation from the ends of the optical fibers is incoherent, and the light spreads with distance in a roughly conical pattern, as indicated in Figure 17b. The spatial response of the receiving fibers is restricted to a more or less conical region with the same angular pattern as for the transmitting beam by virtue of the



(a) Arrangement of Components



(b) Principle of Operation



(c) Operating Characteristic

FIGURE 17
Optical-Fiber Displacement Sensor

reciprocity principle. The overlap area of the transmitting and receiving patterns on the reflecting surface varies with its distance from the fiber ends. With the reflecting surface in contact with the fiber bundles, there is no coupling between the transmitting and receiving channels, but as the reflector is moved away the transmitted light is returned to the receiving channel in increasing amounts until finally a saturation effect is apparent. The operating characteristic is shown in Figure 17c. A large linear region of operation is available, and for vibration measurements the separation of the optical probe from the reflector is set to a distance corresponding roughly to the center of this linear region. In some of the probes manufactured by Mechanical Technology the fibers of the transmitting and receiving bundles are intermixed at the probe end. The operating characteristic then has the same general shape but has greater sensitivity, i.e., greater slope.

The ease with which vibrations may be measured by the Fotonic Sensor appears outstanding after the difficulties of interferometry have been experienced. Very little trouble from building vibrations is encountered when the apparatus is mounted on the 1 inch steel worktable. But this is not really remarkable in view of the much lower sensitivity of the Fotonic Sensor; the important feature is the absence of intermodulation. Any building vibrations that do appear in the output may be filtered out with the signal being unaffected. The dependence of the sensitivity of this instrument on the reflectivity of the vibrating surface detracts from its versatility but is not of importance in this project where aluminum foil is always used.

The major deficiency of the Fotonic Sensor was found to be its high noise level, with the noise being broadband electronic noise. The Model KD-45 Fotonic

Sensor, which has a passband of 0 to 100 kHz and is equipped with the most sensitive type of probe, was used in this project. When a 791 Å signal was observed in the broadband noise, the signal-to-noise ratio was only about 2:1. Narrowing the passband cleaned up the wave form greatly, and by use of a wave analyzer the amplitude of the signal could be measured accurately. The contaminating noise was an obstacle to the accurate measurement of phase, however.

4.2 Attempts to Improve Signal-to-Noise Ratio

The question now came up: Is the noise level of the Fotonic Sensor already irreducibly low, or might it be lowered by the use of more expensive components? The commercial instrument uses a Texas Instruments LS-403 photodiode for the light detector. It was decided to investigate the potential of other photodetectors in this application. A spare optical-fiber probe assembly was available. The transmitting fibers were illuminated by a G. E. 253X lamp, which has a built-in collimating lens. It was necessary to use well regulated d.c. on the filament of this lamp for any modulation of the current appeared also in the light output. A Texas Instruments SIV-7103 silicon photodiode was tried as the detector for the light returned by the receiving fibers. This generating diode is basically of the same type as is used in the laser output monitor, except that it has a much smaller area. A transistor amplifier that had been developed at the Underwater Sound Laboratory for use with these photodiodes was employed in the detection circuit.

While initial results with the new detector looked encouraging, the apparent improvement in signal-to-noise ratio was really only a narrowing of the bandwidth. The original Fotonic Sensor was just about as good when its bandwidth was made

the same. Next, the light from the receiving fibers was delivered to the photomultiplier tube. Again there was no real improvement in signal-to-noise ratio. To see if the noise originated in the tungsten light source, this source was removed, and the laser beam was directed onto the end of the transmitting bundle of fibers. Once more no improvement was effected.

The experiments with the photomultiplier confirmed an important fact that was also evidenced in the experiments with the other detectors: the noise is not present in the dark current. The RCA Phototube Manual⁽²⁶⁾ makes clear what the root of the present problem is. When detection of modulated light in the presence of strong background illumination is attempted, the signal-to-noise ratio is poor because the background light causes much photoelectric emission noise. The modulation of the light beam of the Fotonic Sensor is no more than a few percent for the range of vibration amplitudes encountered in this project. The strong light carrier causes many electrons to be emitted which carry no signal information. But the random emission of all these electrons contributes noise to the output of the detector.

It appears, therefore, that the poor signal-to-noise ratio of the Fotonic Sensor for small vibrations is inherent in its probe characteristics (which result in a low modulation index for small signals) and in the basic physics of the photoelectric process. The search for improvements in this measurement method was therefore concluded. Future work might more profitably be spent in the improvement of capacitive probe instruments.

V

ELECTRICAL INSTRUMENTATION

5.1 Generation of High A.C. Voltage

In high-power transducer applications, a. c. driving fields up to 4 KV/cm rms are in use. Such high fields may be applied only intermittently to the ceramic if severe heating is to be avoided, but many applications require only intermittent driving. The maximum thickness between electrodes of available ceramics is about 3/4 inch, since the poling process has not worked very successfully for thicker pieces. If the maximum field is to be applied to the ceramics of maximum thickness, a power supply that will produce about 8 KV rms is required.

The primary power supply for this project is a 200-watt McIntosh Model MI-200 AB audio amplifier. Since only a few watts are actually dissipated in the ceramic transducers, it might seem that there is ample reserve to take care of losses in the impedance matching networks. Such is not the case, however, and only about half of the voltage objective mentioned above was achieved. The available voltage, however, is enough to drive the ceramics into their interesting high-dissipation region of operation.

The audio frequency signal which drives the amplifier is obtained from a H.P. 200 CD oscillator, or the G.R. 1900 A wave analyzer operating in the Tracking Generator mode. For some high-field measurements the input is chopped into low duty-cycle pulse trains by an electronic pulser and gate circuit. This

equipment was built at the Underwater Sound Laboratory for long-pulse applications, and for present measurements it was usually set to produce pulses .1 second long at a repetition rate of 1 per second. The heating of the ceramic is then only one-tenth of what it would be for continuous excitation, while the pulse length is long enough to achieve steady-state vibrations in the ceramics and to permit oscillographic observations.

To step up the voltage from the 200-watt amplifier a high-voltage transformer is needed. The best that could be found was a UTC Varimatch modulation transformer Model CVM-4. Its maximum turns ratio is 7.3. A transformer with 4 times this turns ratio was built at the Underwater Sound Laboratory, but the distributed capacity and resistance of the large secondary winding were so great as to negate the advantage of the higher turns ratio.

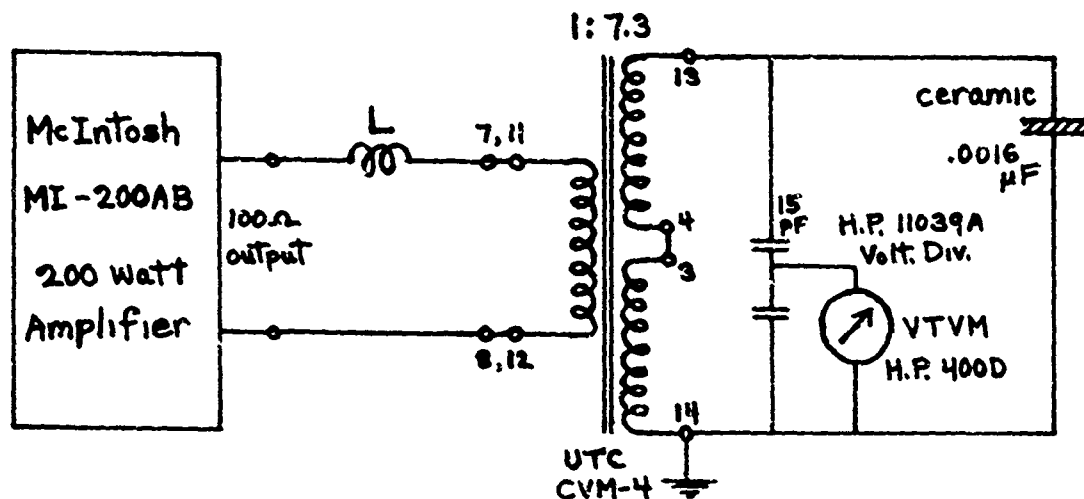
Reactance cancellation is necessary before large voltages can be achieved. The ceramic transducers act as capacitive loads in their stiffness-controlled frequency range, which is the range of present interest. Also, the transformer contributes a great deal of capacity. The inductors required to tune out this combined capacity are not readily obtained in the required high-voltage rating. A 5000-volt decade inductor covering the range .01-.1 Henries was built at the Underwater Sound Laboratory. More inductance would be desirable, but the feasibility of obtaining it is questionable. The cores and windings must be large in order to handle the voltage and reactive power. Hence, the distributed capacity and loss resistance can become excessive when one tries to attain the higher values of inductance.

Only two sizes of ceramic samples were used in this investigation, and the

matching circuits which were devised for these ceramics are shown in Figure 18. Figure 18a shows the circuit for the 5-inch bars, which were to be driven at about 3 kHz. Using the maximum turns ratio that the UTC transformer could provide proved to give the best results in this case. Insufficient inductance was available to tune out the capacity on the high-voltage side, but reactance cancellation in the primary circuit was satisfactory. A maximum voltage of 4500 V rms on the sample was achieved. The voltage is measured with a H.P. 400 D VTVM operating in conjunction with a H.P. 11039 A capacitive voltage divider. Figure 18b shows the circuit for the 3/4-inch bars, which were to be driven at about 8.7 kHz. In this case tuning the secondary was much better than tuning the primary even though considerable capacity (.002 μ F) had to be added to the secondary to achieve resonance with the inductance that was available. The maximum voltage obtainable was 3400 V rms. At the relatively high frequency used in this circuit the Q of the system was only about 7.

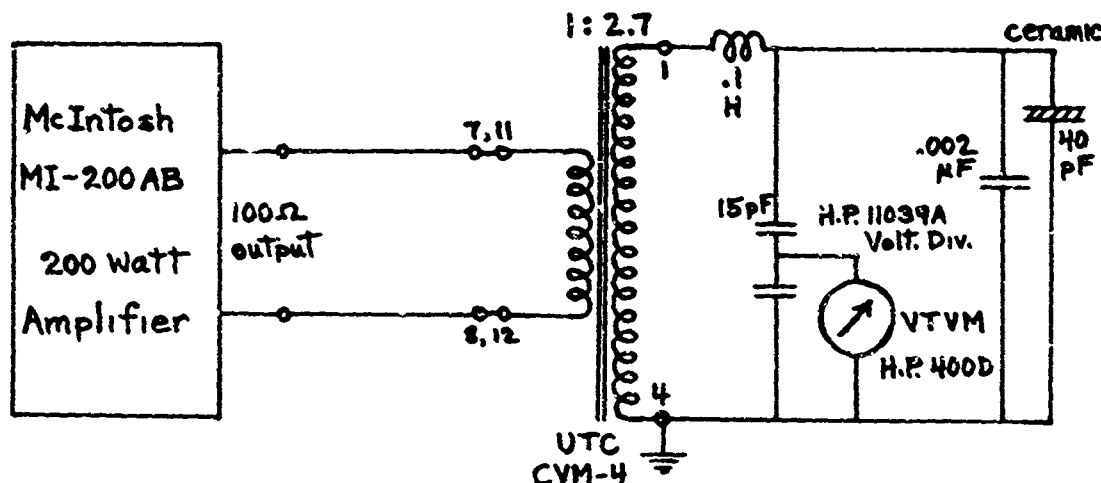
5.2 Measurement of Amplitude and Phase

Equations (11), (12), and (13) define three phasor ratios whose magnitudes and phases are to be measured. Two of these ratios, ξ/E and ξ/Q , contain the mechanical variable ξ , but ξ will be converted to an electrical variable by one of the displacement sensors described in previous sections, namely, the interferometer or the Fotonic Sensor. Assuming that the sensors are calibrated, the problem that remains is to measure the amplitude and phase of the sensor's output with respect to the driving voltage or charge. An auxiliary problem is measuring the amplitude and phase of the transducer's current with respect to the driving



$$L = .01, \text{ or } .02 \text{ H.}$$

(a) 2700 - 3500 Hz. Supply for 5" Bars



(b) 8700 Hz. Supply for 3/4" Bars

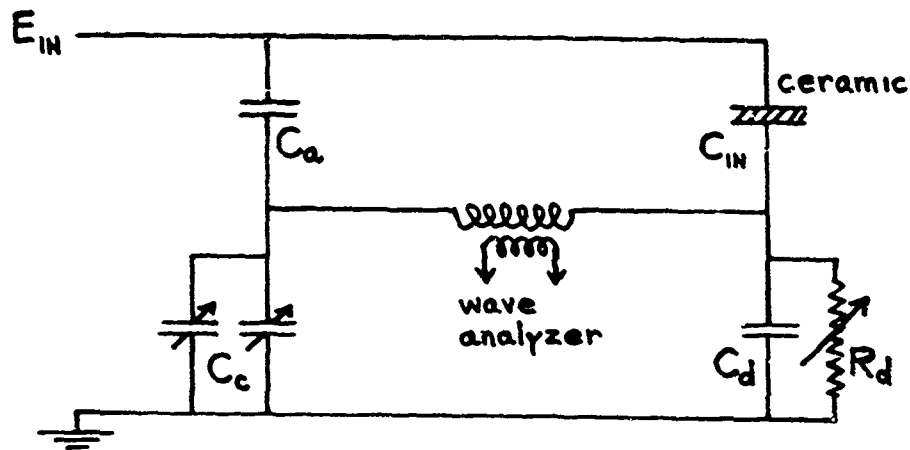
FIGURE 18
High-Voltage Power Supplies

voltage. The amplitude measurements are easily carried out but the phase measurements are difficult when the phase angles are of the order of 1 degree as they are in these ceramic transducer experiments.

Although many phase meters are now available commercially, those that could be obtained for this project did not appear to have the necessary accuracy, especially when the signals were contaminated with noise and were at greatly different levels in the two input channels. It was decided to use comparison methods and to rely on high-accuracy RC networks to produce the known phase shifts. Two methods of comparison were found useful: (1) the null method in which both the amplitude and phase of the signal to be measured were balanced against those of the signal from the standard RC network, and (2) the Lissajous pattern method in which just the phase of the signal to be measured was balanced against that of the signal from the standard RC network.

5.2.1 Driving-Point Impedance Bridge

General Radio decade resistance boxes and decade condensers were employed as the precision elements in the standard RC network. The simplest of the comparison setups is the bridge used to measure the input impedance of the transducer as defined by Equation (13). The circuit of this bridge is shown in Figure 19. The main consideration determining the choice of the circuit is the voltage limit of the precision circuit elements. The potential of the lower half of the bridge with respect to ground must not exceed 500 volts, while the input voltage to the bridge may be 5000 volts or more. Actually, it is possible to keep the voltage across the lower arms below 50 volts and still have ample sensitivity. This safety factor,



At balance:

$$C_{IN} = \frac{C_a}{C_c} C_d \quad \tan \delta_{IN} = \frac{1}{\omega R_d C_d}$$

$C_d \gg C_{IN}$,

Hence: ceramic voltage \approx supply voltage.

C_a : 100 pF vacuum condenser, Jennings W-100;
or 1000 pF mica condenser, Cornell-Dubilier Type 960-30B.

C_c : G.R. Type 1419-A decade capacitor, plus
G.R. Type 1428-BM variable capacitor.

C_d : G.R. Type 1419-A decade capacitor.

R_d : G.R. Type 1432-M decade resistor.

Bridge Transformer : G.R. 578-A .

FIGURE 19
Driving-Point Impedance Bridge

plus the fact that the a.c. power supply has high internal impedance, ensures the safety of the precision circuit elements when arc-overs between the ceramic electrodes occur.

To achieve the desired low potentials the capacities of the lower arms must be about 100 times greater than the capacities of the corresponding upper arms. The chosen bridge circuit requires only one high-voltage circuit element: the condenser C_a . Glass-sealed vacuum condensers are ideal for this element, and the 100 pF unit that is used is of this type. An 8000-volt 1000 pF mica condenser is also installed and may be connected into the circuit in place of the 100 pF vacuum condenser. The best convergence towards a balance is achieved by adjusting R_d to balance the dissipation factor and adjusting C_c to balance the capacity of the ceramic. Occasionally the resistance R_d is placed in series with C_c , but the parallel connection is generally preferred.

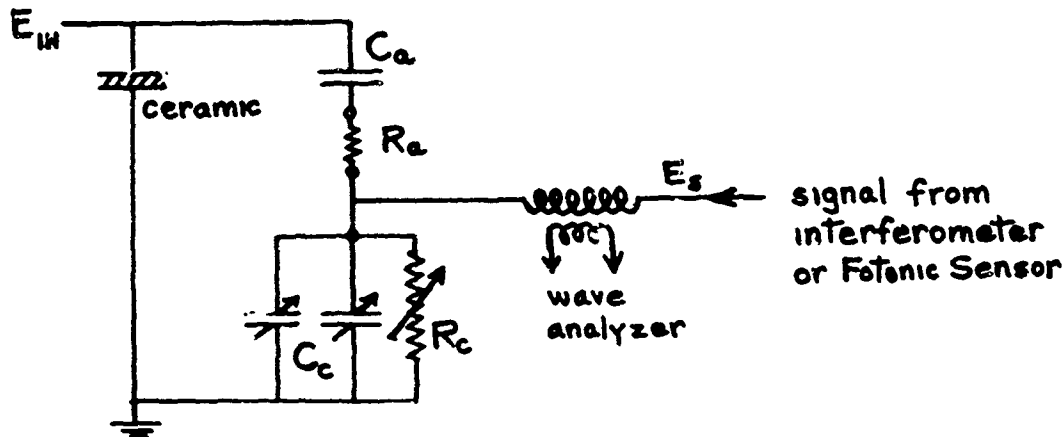
The G.R. 1900 A wave analyzer is used as a bridge detector. When the current through the ceramic becomes distorted at high driving fields, sharp balances are still obtainable with the aid of the wave analyzer. The impedance which the bridge measures is defined as the ratio of the applied voltage (which is sinusoidal) to the fundamental component of the current. At the highest driving levels used, the distortion of the current wave observed on an oscilloscope is barely noticeable; so the fundamental component differs but little from the total current.

For bridge measurements the wave analyzer is used in its Tracking Generator mode. It then supplies a signal which is used to drive the 200-watt amplifier, and the analyzer never drifts out of tune with the signal. The output of the

analyzer in this mode is a 100 kHz signal whose amplitude is proportional to that of the fundamental component of the input signal. For CW measurements the output meter on the wave analyzer is used as the bridge indicator, while for pulse measurements the 100 kHz output signal is observed on an oscilloscope. Three choices of bandwidth (3, 10, 50 Hz) are available in the analyzer, and the 10 Hz bandwidth is a good match for the .1 second pulses that are normally used.

5.2.2 Transfer Parameter Bridges

In measuring the electromechanical transfer parameters, the same null balancing procedures as are used in the driving-point impedance bridge are employed. Figure 20a shows the circuit used in the measurement of ξ/E . The signal from the interferometer or the Fotonic Sensor is balanced against a signal from a precision voltage divider and phase shifter. This circuit is formed from the same components as are used in the bridge circuit in Figure 19. The elements R_c , C_c in the low-voltage branch, however, can provide only phase lead. To provide phase lag a resistance R_a is inserted in the high-voltage branch. This resistor is composed of a number of 1/2-watt metal-film resistors wires in series. A set of these plug-in units was made up and their resistances were determined by measurement in a G.R. 1650 A bridge. A resistor from this set is selected which gives more lag than is needed; the excess lag is then balanced out by adjustment of the decade box R_a . When a null balance is achieved, this circuit determines the magnitude and phase relations between the voltage output of the displacement sensor, E_s , and the voltage applied to the ceramic E_{IN} .



$$\frac{E_s}{E_{in}} = \left| \frac{E_s}{E_{in}} \right| e^{j\theta'_E}, \quad \theta_E = \theta'_E - \theta_c,$$

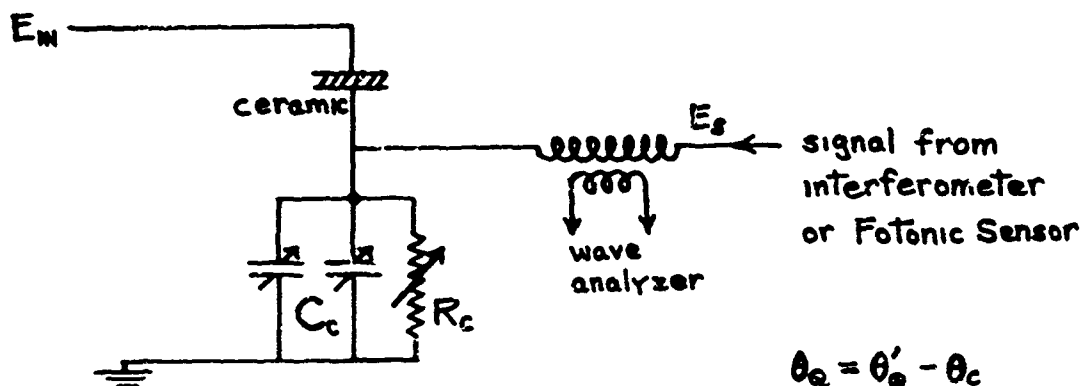
θ_c = phase correction, obtained by circuit of Fig. 21a.

At balance:

$$\tan \theta'_E = - \frac{\omega R_a C_a - \frac{1}{\omega R_c C_c}}{1 + \frac{C_a}{C_c} \left(1 + \frac{R_a}{R_c} \right)}$$

$$\left| \frac{E_s}{E_{in}} \right| = \frac{1}{\left(1 + \frac{C_c}{C_a} + \frac{R_a}{R_c} \right) \sqrt{1 + \tan^2 \theta'_E}}$$

(a) Circuit for Measuring S/E



$$\theta_Q = \theta'_Q - \theta_c$$

At balance:

$$\tan \theta'_Q = \frac{1}{\omega R_c C_c}$$

$$\left| \frac{E_s}{Q} \right| = \frac{1}{C_c \sqrt{1 + \tan^2 \theta'_Q}}$$

(b) Circuit for Measuring S/Q

FIGURE 20
Transfer Parameter Bridges

Figure 20b shows the circuit used for measurement of ξ/Q . When $R_c = \infty$, the voltage developed across C_c is Q/C_c , if the bridge is balanced so that no current flows into the bridge transformer. Thus, a signal representative of the ceramic charge Q is achievable, but this signal must be phase-shifted to produce a balance. The decade resistor R_c will provide phase lead. To provide phase lag a different approach from that used in Figure 20a must be devised. While insertion of a series resistance in the high-voltage branch produces a phase shift with respect to the applied voltage, it does not produce any phase shift with respect to the current or charge, which is the variable of present interest. The simplest solution to the problem of providing phase lag appeared to be to introduce it into the channel which carries the signal E_s from the displacement sensor. It is for this purpose that the condenser C_p was installed in the output circuit of the interferometer, as shown in Figure 7. The calibration procedure for the sensor must, of course, include a determination of the phase shift intentionally added to its channel.

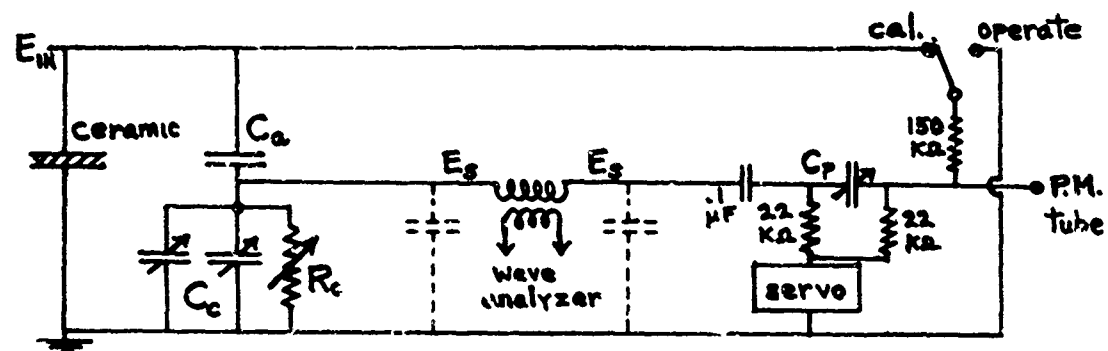
The two circuits of Figure 20 enable accurate measurements to be made of the outputs of the displacement sensors. The next problem to consider is the transfer characteristics of the sensors themselves. For the role of absolute standard, the Fotonic Sensor is considerably less promising than the interferometer; so the Fotonic Sensor is used for relative measurements only. It is useful for observing the change of phase and magnitude of the ceramic's transfer parameters as the driving voltage is raised, but the absolute values of these parameters will be determined by the interferometer. The interferometer gives amplitudes directly in terms of the wavelength of light; so there is no problem as far as the magnitude

of its transfer characteristic is concerned. The one problem that does remain is the determination of the phase shift between the mechanical displacement ξ measured by the interferometer and its electrical signal E_s , which is delivered to the comparison circuits of Figure 20.

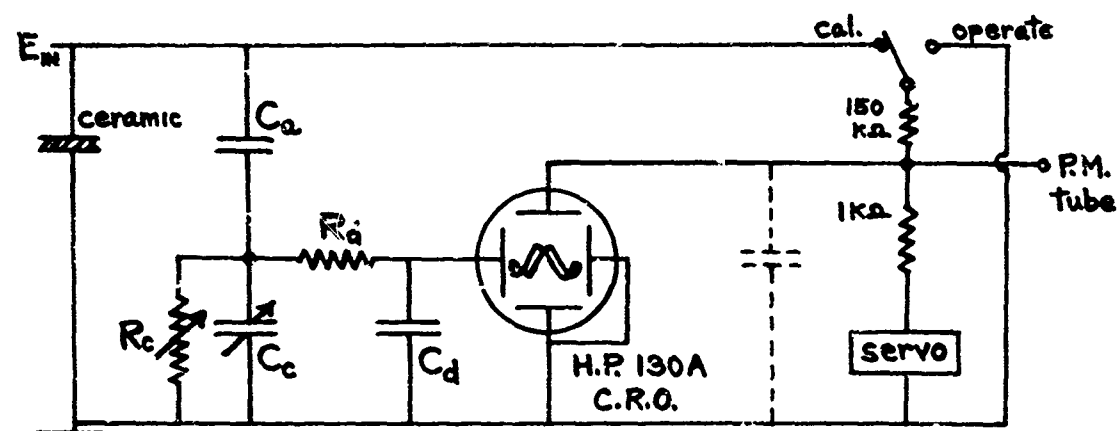
5.2.3 Phase Calibration of the Interferometer

To use the interferometer for the absolute measurement of mechanical phase angles it is necessary to assume that no phase shift exists between the displacement signal and the photomultiplier current. This assumption appears well justified. The pulse rise time of the photomultiplier is 3×10^{-9} seconds, and the transit time is less than 10^{-7} seconds.⁽²⁶⁾ The latter figure indicates that the phase shift should be less than .36 degree at 10 kHz. When measurements on the photomultiplier current are attempted, shunt capacities are introduced which cause phase shifts, but these effects may be corrected. In the circuits of Figure 20 these shunt capacities comprise the capacity of the cable going from the photomultiplier to the bridge transformer (180 pF) and the shunt capacity of the transformer input (40 pF). At balance the current through the transformer primary approaches zero, but current continues to flow into the transformer's capacity to ground.

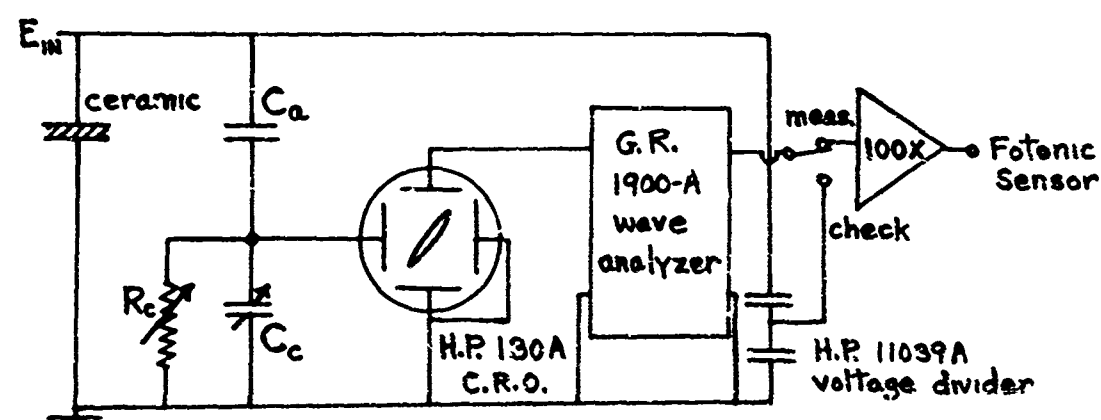
Figure 21a shows the calibration circuit for determining the phase error caused by the measurement circuitry. The principle of operation is the substitution of a current derived from the high-voltage power supply for the photomultiplier current. The photomultiplier remains connected into the circuit, but its light signal is blocked off during calibration. If the series resistor which draws



(a) Circuit for Phase Calibration of Transfer Parameter Bridge



(b) Circuit for Absolute Measurement of θ_E , Using Interferometer



(c) Circuit for Relative Measurement of θ_E , Using Fotonic Sensor

FIGURE 2:
Phase Measurement Circuits

the calibration current from the high-voltage supply is large enough, the current will be in phase with the supply voltage E_{IN} . The null balancing procedure is carried out and the values of C_c and R_c at balance give the phase shift θ_c that exists in the measuring circuit. This value is subtracted from the phase angles measured by the circuits of Figure 20 in order to arrive at the true electromechanical phase angles θ_E and θ_Q . Since this calibration procedure must be carried out in any case, no real loss is suffered in introducing additional phase shift by means of the condenser C_p in order to facilitate balancing of the circuits of Figure 20 when phase lag is required.

The validity of the calibration method depends on the excellence of the resistor used to produce the calibration current. If appreciable shunt capacity is associated with this resistor, the calibration current will not be in phase with E_{IN} as required. With this limitation in mind the value of the calibration resistor was chosen to be $150 \text{ K}\Omega$, whereas if the capacity problem did not exist a higher value of resistance would be desirable. The resistor is a 6-inch string of five $30.1 \text{ K}\Omega$, $1/2$ -watt metal-film resistors. A shunt capacity of 3 pF across each resistor of this string would cause .1 degree phase shift at 10 kHz , but the estimated shunt capacity is much less than this value. The resistor string is suspended well away from other conductors to avoid mutual capacity effects. Both estimates and measurements of the mutual capacities indicate that they are negligible.

The impedance to ground of the node into which the calibration resistor injects current is about $11 \text{ K}\Omega$. The $150 \text{ K}\Omega$ calibration resistor is, therefore, not large enough to form a constant-current source when it is connected to the supply voltage. It should form such a source if it is to be a proper substitute for the

photomultiplier, but as explained above, use of a much greater value of resistance would invite trouble from stray capacities.

A subterfuge can be used to get the same results with the $150\text{ K}\Omega$ calibration resistor as would be obtained if this resistor were made nearly infinite. The procedure is to have the $150\text{ K}\Omega$ resistor shunting the photomultiplier during normal measurements and to shift it into its series position (connected to the supply voltage) during the calibration process. Figure 22 shows the right-hand portion of the

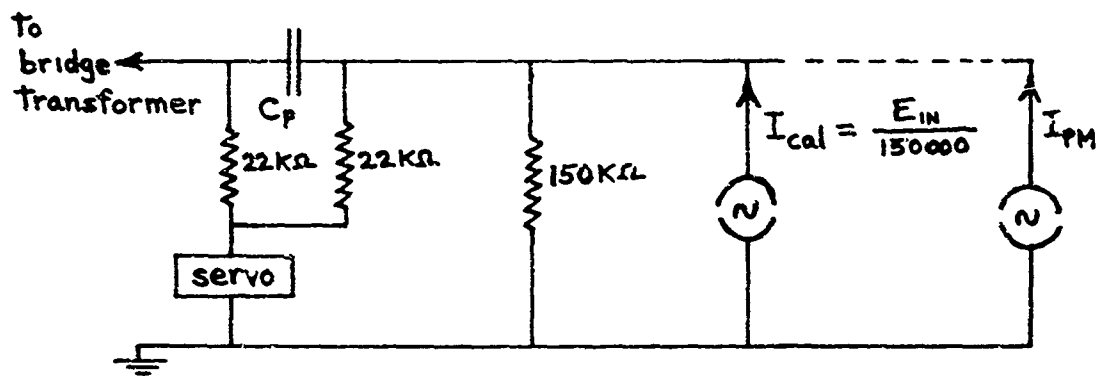


FIGURE 22
Calibration Circuit after Thévenin Transformation

circuit in Figure 21c in the calibrate mode, after the source of calibration current has been represented in parallel form, rather than its actual series form, by Thevenin's theorem. An ideal current source now appears in the diagram; this source is a proper substitute for the photomultiplier, which is a current source. The ideal current source is, of course, shunted by the $150\text{ K}\Omega$ calibration resistance. When the ideal current source is deactivated (to return to the measurement mode) the $150\text{ k}\Omega$ shunt resistance should remain in the circuit if the calibration, which is based on the assumption of an ideal current source, is to remain valid. This requirement is satisfied by replacing the conceptual $150\text{ K}\Omega$ shunt by a physical one when the

equipment is used for measurements. What has been accomplished by this procedure may be summarized by saying that the $150 \text{ k}\Omega$ shunt resistor produces a slight phase shift which compensates for the slight phase error that occurs in the calibration process as a result of the source resistance being noninfinite.

5.2.4 Advantages and Disadvantages of Null Methods

The null methods described above have the advantage that all filtering is done after the two signals have been combined in the comparison circuit and, therefore, the phase shift of the filter is irrelevant. A disadvantage is that to measure phase accurately the amplitude of the unknown signal must be balanced to a much finer degree than would be required merely to measure the amplitude itself with satisfactory accuracy. For example, if the phase error is to be kept down to .1 degree, the balance must be perfected until the bridge output is less than .2 percent of the signal amplitude being measured. The interferometer signal, however, fluctuates about 1 percent, even with the laser intensity control system in operation; therefore, a steady balance this good is not achievable. The signal from the Fotonic Sensor passes through an amplifier with a gain of 100 or 1000 before it is presented to the bridge, and the fluctuations in gain of this combined system are also noticeable at balance. Because of these difficulties it is necessary to be content with a running balance in the transfer parameter bridge. As the signal drifts through the balance range, the phase shift is adjusted with the resistor R_c until a deep null is obtained momentarily during the drift cycle.

5.2.5 Phase Balancing by Lissajous Patterns

Instead of balancing amplitude and phase simultaneously as described above,

phase only may be balanced by use of Lissajous pattern displays on an oscilloscope. The output from the displacement sensor is applied to the vertical channel of the scope, the signal from the standard phase shifter is applied to the horizontal channel, and the phase shifter is adjusted until the pattern indicates zero phase difference. Figure 21b shows the circuit used with the interferometer for measuring the phase angle between the driving voltage and the mechanical displacement. The phase shift network is similar to the networks used in the previous circuits except that a resistor R_d has been inserted in order to provide phase lag.

For small signals the Lissajous pattern is the conventional ellipse, and zero phase is indicated when the ellipse has been closed into a straight line. For large signals the signal from the interferometer would trace out the cosine curve of Figure 5 if it were plotted against a linear time base. But the actual time base is a sinusoidal signal obtained from the phase shift network, and the resulting display is a distorted Lissajous pattern as shown in Figure 23a. The homodyne

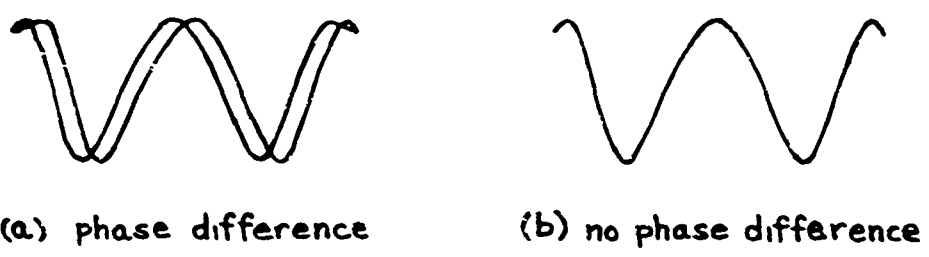


FIGURE 23

detector acts like a crude frequency multiplier for large signals. When the mechanical signal ξ is in phase with the time base signal, the oscillograph pattern retraces itself over the cycle and a single line is obtained as shown in Figure 23b.

To measure θ_Q rather than θ_E , the condenser C_a is removed from the circuit and the ceramic sample put in its place.

The equations for the phase shifter used in the circuit of Figure 21 b are

$$\tan \theta'_E = \frac{\frac{1}{\omega R_c C_s} - \omega R_d C_d \left(1 + \frac{C_a}{C_c}\right)}{1 + \frac{C_a}{C_c} + \frac{C_d}{C_c} \left(1 + \frac{R_d}{R_c}\right)}, \quad (56)$$

and

$$\tan \theta'_Q = \frac{\frac{1}{\omega R_c C_s} - \omega R_d C_d}{1 + \frac{C_d}{C_c} \left(1 + \frac{R_d}{R_c}\right)}. \quad (57)$$

The condenser C_d is kept large enough (e.g., $C_d > .01 \mu\text{F}$ at 3 kHz) that the $1 \text{ M}\Omega$ input resistance of the scope does not cause any appreciable phase shift. The resistor R_d is a measured, metal-film resistor employed as a plug-in unit. The phase shift of the scope and associated circuitry must be measured and used to correct the phase angles given by Equations (56) and (57), before the true phase angles θ_E and θ_Q may be found. The procedure used for phase calibration is the same as that used with the transfer bridge and discussed in connection with Figure 21a; that is, a calibration current drawn directly from the high-voltage supply is substituted for the photomultiplier current, and the phase shifter is adjusted until the ellipse closes into a straight line.

For large signals the output of the photomultiplier contains multiple frequencies, and any phase shift in this channel will cause changes in the wave form

unless the phase shift is equivalent to a time delay (phase shift proportional to frequency). When such wave form changes do occur, it is no longer possible to obtain complete retracement of the oscillograph figure as shown in Figure 23b. All phase shifting is, therefore, done in the horizontal scope channel where the signal is a pure sinusoid for ξ/E measurements. For ξ/Q measurements the situation is less ideal. The charge wave form is slightly distorted at high levels, and the oscillograph curves always contain regions where they are double-valued. The phase shifter is then adjusted so that retracement occurs over the central portion of the figure. To keep the phase shift of the photomultiplier signal low, the resistance in its output circuit is reduced to $1\text{ K}\Omega$. The loss of signal voltage thus incurred can be compensated by increasing the gain setting of the oscilloscope.

The method of measuring phase described above contains a weak link in its logical chain. The phase calibration is done only with the fundamental component of the signal, since there is no practical way of reproducing the distorted interferometer output wave form in the substituted calibration signal. For large signals the photomultiplier output is composed predominantly of frequency components higher than the fundamental. Even though there is no noticeable phase distortion in the complex signal, the possibility remains that the complex wave may have undergone a phase shift different from that determined by the calibration procedure at the fundamental frequency. The calibration procedure, of course, can be carried out at higher frequencies also, and the results indicate that the differential phase shift between the two channels of the H.P. 130 A oscilloscope stays in the range 0 - 2 degrees. In other applications the method

of phase measurement described above might be quite adequate, but for this project its adequacy is doubtful.

5.2.6 Relative Phase Measurements with Fotonic Sensor

Since the output of the Fotonic Sensor is essentially undistorted, the difficulties described above do not apply to it. However, the phase shift through this instrument is unknown; therefore, it is useful only for relative measurements. The Lissajous pattern of the Fotonic Sensor's output is an ellipse, but it is so contaminated with noise that detection of a few degrees of phase shift is not possible. However, passing its signal through the G.R. 1900 A wave analyzer removes the noise. For this application the wave analyzer is operated in its Normal mode; it then provides a filtered output signal, but no longer serves as a signal generator as it does in the Tracking Generator Mode. The H.P. 200 CD oscillator is now used to drive the 200-watt amplifier. The phase shift of the wave analyzer varies rapidly through its pass band, and by careful tuning the phase shift may be adjusted so that the ellipse on the scope is closed into a line.

Figure 21c shows the circuit used for the measurement of relative phase. The output from the Fotonic Sensor is amplified by a factor of 100 and then delivered to the wave analyzer, which, in turn, supplies the filtered signal to the vertical channel of the scope. The phase shift network, which can produce only phase lead, is set initially to provide a few degrees phase shift. Then, the tuning of the wave analyzer is varied slightly to close the ellipse. Next, the voltage on the ceramic is raised, and if the ellipse opens up it indicates that the phase angle θ_E changes with increasing electric field. The ellipse is reclosed by adjusting

R_c and from the change in R_c the phase change (which may be positive or negative) is computed using the equation given in Figure 20. To observe changes in θ_a the procedure is the same except that the condenser C_a is replaced by the ceramic sample.

This method of measuring phase changes appears quite sound in principle; the problem is to be able to close the ellipse accurately enough that the residual phase shift will be less than 1 percent. It is best to start with the ellipse covering at least half of the oscilloscope screen. The ceramic voltage may then be increased by a factor of 2 or 3; the ends of the ellipse will be driven off the screen, but phase nulling is carried out very successfully with the portion that remains visible. To practice this procedure and to make sure that over-driving the scope screen does not cause error, a check circuit is used as shown in Figure 21c. In this case the input to the wave analyzer is taken from the H.P. voltage divider instead of from the Fotonic Sensor. Raising the voltage by a factor of 3 then causes no opening of the loop, and this result supports the validity of the method.

The evaluation of the different methods of measuring phase will be discussed further in the final section giving the results of the measurements on the ceramics.

VI

MOUNTING SYSTEM FOR THE CERAMIC BARS

The ceramic bars that are used as test transducers must be mounted in such a way that they can be accurately positioned with respect to the light beam of the interferometer or with respect to the probe of the Fotonic Sensor. These requirements suggest that the bars be rather firmly held by the support structure, but on the other hand the mounting must be so flexible that the structure does not absorb appreciable vibrational power nor affect the vibrational modes of the bars. A mounting system which appeared to be a reasonable compromise between these conflicting requirements is illustrated in Figures 24 and 25.

Thin leaf springs, which respond in their bending mode when the bar is vibrating, are used to position the bar above a steel carriage. The steel carriage is supported at three points by thumbscrews which bear on the steel base plate of the worktable. By adjusting these thumbscrews the position and vertical tilt of the mirror attached to the ceramic bar is controlled. The long bars require at least two leaf springs for stability; otherwise their rocking motion would be excessive. However, for the 3/4-inch ceramic bar shown in Figure 25b, a single spring was sufficient.

6.1 Stabilizing the Bar Against Building Vibrations

The 5-inch ceramic bars, such as the one shown in Figure 24, have two

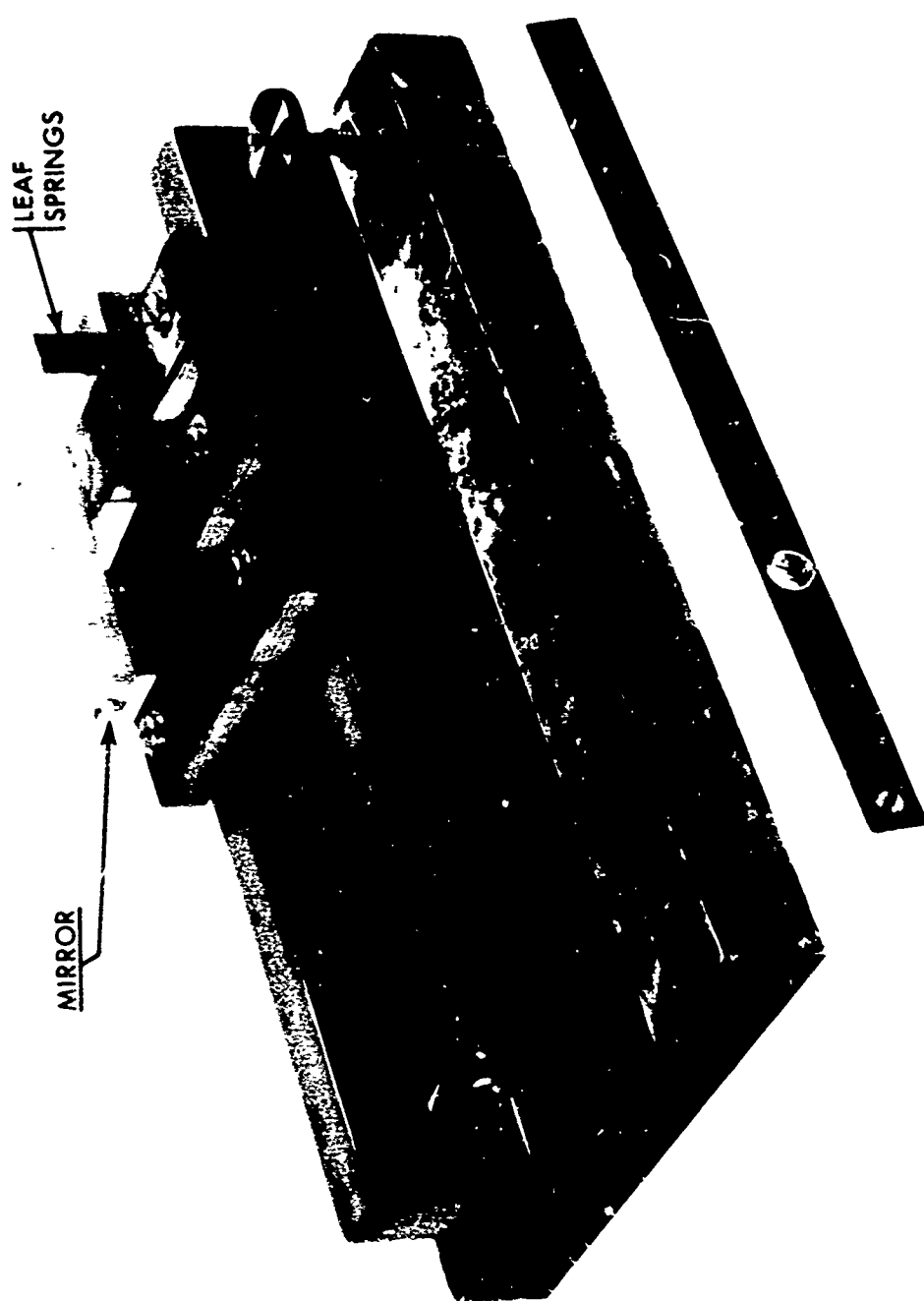


Figure 24
Five-inch Barium Titanate Bar Mounted on Vibrator Carriage



Ceramic Cylinder with $\lambda/4$ Glass Stubs Attached
Free Ceramic Cylinder

Figure 25

$3/8'' \times 3/4''$ PZT-4 Ceramic Vibrators

.007-inch-thick phosphor bronze springs attached 1 inch from the bar ends. These two springs control the rocking motion adequately but they allow excessive axial motion of the bar in response to building vibrations. Consequently, a third spring is attached at the center of the bar, which substantially increases the stiffness to axial motion. The center of the bar is the best place to attach mounting structure because it contains a nodal plane for the desired longitudinal vibrations. That is, when the bar is driven electrically, it is a balanced vibrator; the two ends have equal but opposite velocities and the center has zero axial velocity. When the bar responds to low-frequency room vibrations, on the other hand, it moves as a rigid body and the center has the same velocity as the ends. The central spring, therefore, inhibits the response to room vibrations, but it is not coupled to the axial motion of the piezoelectric vibrations.

Advantage of the central nose is also taken to introduce some damping into the suspension system. The central spring is made of 1/16-inch cellulose acetate, which is a much more lossy material than the phosphor bronze used for the other springs. The objective of measuring ceramic properties would be best served by use of a low-loss mounting system, since coupling of external dissipation into the vibrating system tends to falsify the results for the ceramics. But interferometry is difficult unless the natural vibrations of the support system excited by room vibrations are damped. Using the central spring to introduce dissipation causes minimal damping of the piezoelectric vibrations, yet the damping is fully effective against the rigid-body motions. It would be false to claim, however, that the central spring is totally uncoupled to the piezoelectric vibrations. While the axial motion is zero at the center during piezoelectric vibrations, the transverse motion is

uniform along the length of the bar. An end-electroded round bar, for example, has a transverse strain $S_1 = S_2 = d_{11} \epsilon_3$, according to Equation (1), and the transverse displacement is this strain multiplied by the bar radius. This radial motion excites the springs into longitudinal vibrations.

The principal motion of the springs is a bending motion with the longitudinal motion mentioned above being a minor effect. The spring motion will, therefore, be considered from the point of view of beam bending theory. The bases of the leaf springs are cemented to formica cross members on the vibrator carriages. This construction provides clamped-end boundary conditions (the slope of the spring at the end is constant during the vibration cycle). The upper ends of the springs are cemented to the bars, but here a butt-joint type of construction is used. An epoxy adhesive Armstrong A-2 is used for all these joints. The butt joints on the bars were expected to approximate clamped-end boundary conditions for the springs, but the epoxy cement is not stiff enough for this condition to be realized. The calculated rigid-body resonance of the 5-inch ceramic bar with two phosphor bronze springs, for example, is 36 Hz if the butt joints are assumed to provide clamped-end boundary conditions and 6.4 Hz if they are assumed to provide hinge joints. The measured resonance was 13 Hz. When the plastic spring was added at the center, the resonance went up to 65 Hz.

The suspension resonance, with the plastic spring installed, has a Q about 10. As indicated in Figure 14, this resonance no longer contributes an excessive disturbance. It would be inadvisable to use any less spring stiffness, even with damping, for two reasons: (1) the resonant frequency should be kept high enough that the base-plate attenuation is effective in reducing the excitation of the

resonance; and (2) the response to low-frequency building vibrations is inversely proportional to the stiffness, and it is these frequencies (below 20 Hz) that cause the most disturbance.

6.2 Behavior at Frequencies Used for Measurements

In the frequency range above 1 kHz, where the measurements on the ceramics will be made, the springs have a series of bending mode resonances. The mechanical impedance that the springs offer to the tangential motion of the ceramic surface to which they are bonded is of interest. The general form of the impedance function is shown in Figure 26. The impedance functions of flexing beams

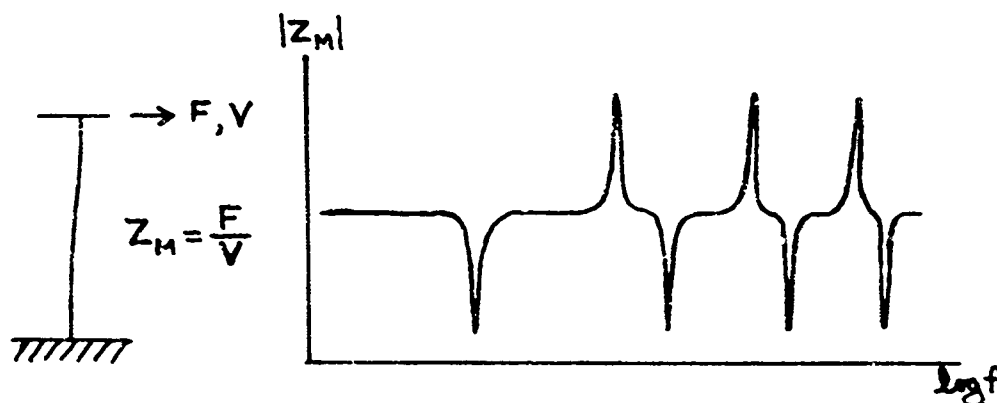


FIGURE 26
Driving-Point Impedance of a Flexing Beam

with different boundary conditions and different degrees of damping have been computed by Snowdon.⁽²⁷⁾ However, the boundary conditions and damping contributed by the cement joints are not known accurately for the springs used here; so the computed data can not be put to much use. Trouble is to be expected at the antiresonant frequencies, where the supports have their maximum impedances, and a search for these effects can be carried out experimentally.

A 5-inch barium titanate bar has its lowest resonance at 18 kHz when unmounted. Any perturbations of its driving point or transfer impedances below this frequency may be attributed to the influence of the mounting system. A very sensitive method for detecting these perturbations is to examine the electromechanical phase angle θ_E using the interferometer and a Lissajous pattern display, while the frequency is swept through the contemplated operated range. This is done at low-signal levels with no phase shift introduced; so the normal Lissajous pattern is a closed ellipse. To remove the slight jitter caused by the building vibrations that survive the action of the control system, the interferometer signal is passed through a Krohn-Hite filter set for a lower cutoff frequency of 100 Hz. The phase shift of the filter is insignificant for frequencies above 1 kHz.

For the 5-inch barium titanate bar the ellipse opened up noticeably at the following frequencies: 1257, 1467, 1565, 1768, 4018, 4389, 4786, 6548 Hertz. The indicated phase shift was only a few degrees in most cases and the amplitude perturbations were scarcely measurable. The assumption is made that if these critical frequencies are avoided when measurements are made, valid data on the ceramic properties will be obtained. The only direct support for this assumption comes from the measurements of the electrical input impedance Z_{IN} . This impedance may be measured for a free bar (that is, a bar suspended on the fine wires that are used for the electrical connections), as well as for the mounted bar. No significant differences were found in the input impedance of a bar before and after mounting when measurements were made at frequencies other than the critical frequencies mentioned above.

VII

MEASURED CERAMIC PROPERTIES

7.1 5-inch Barium Titanate Bar

Measurements were made on a 5-inch barium titanate bar manufactured by Clevite Corporation from their Ceramic-B material. The bar is 5/8-inch wide by 1/2-inch thick, and the voltage is applied across the 1/2-inch dimension. The mounting of this bar is shown in Figure 24. A frequency of 3400 Hz was used for the measurements, and there were no secondary resonances due to the mounting observable in the vicinity of this frequency.

The variations of the electrical dissipation factor $\tan \delta_{IN}$ and the permittivity ϵ_{33}^T with driving field are shown in Figure 27. These measurements were made with the circuit of Figure 19, and for voltages above 1000 V rms pulsing was employed. At the highest voltage used (3200 V rms) a half minute of steady driving would cause very noticeable heating, and the ceramic properties would change excessively. The behavior of the dissipation factor is in accordance with published data.⁽⁵⁾ The permittivity increases considerably at high driving fields. Although polarization saturation eventually would set in, at the maximum field used in practice the polarization is still increasing faster than the field.

The relation between the a.c. strain and the driving field is shown in Figure 28a. These data are derived from measurements of the magnitude of the transfer ratio ξ/E ; the strain equals the displacement divided by half the bar length.

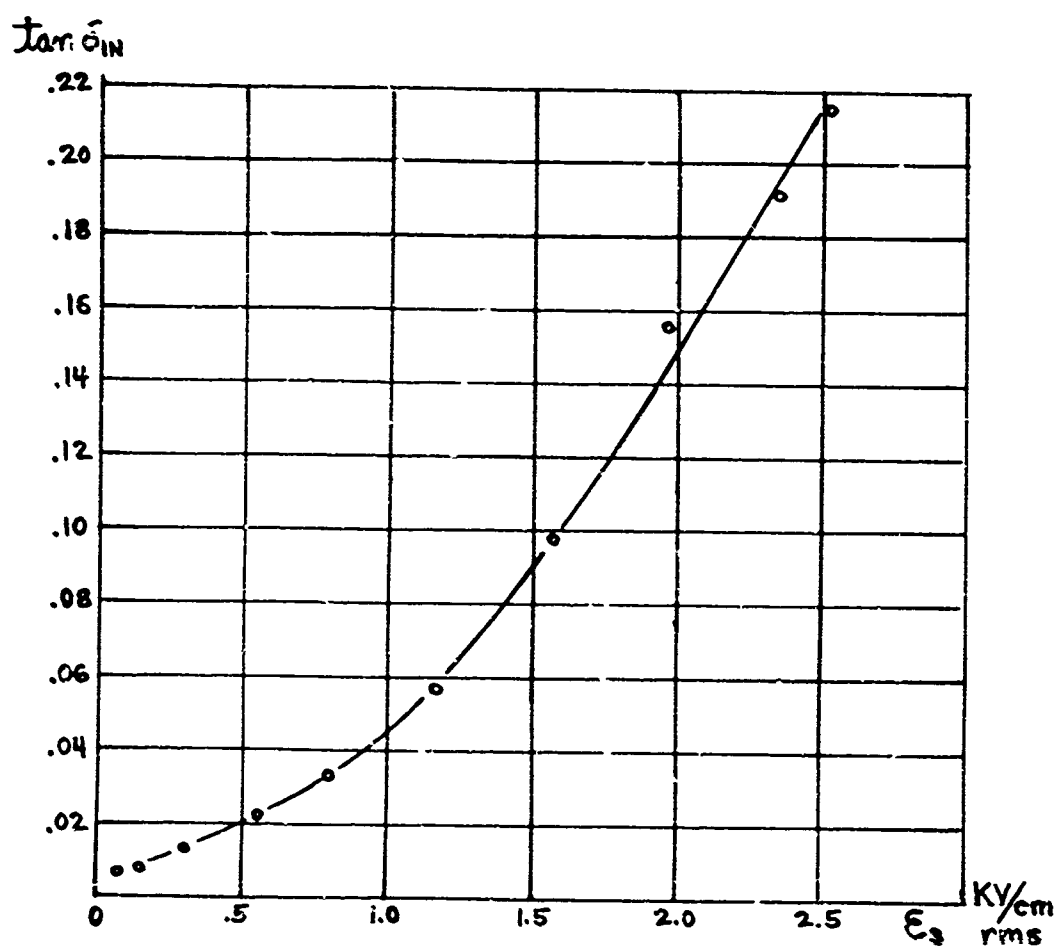
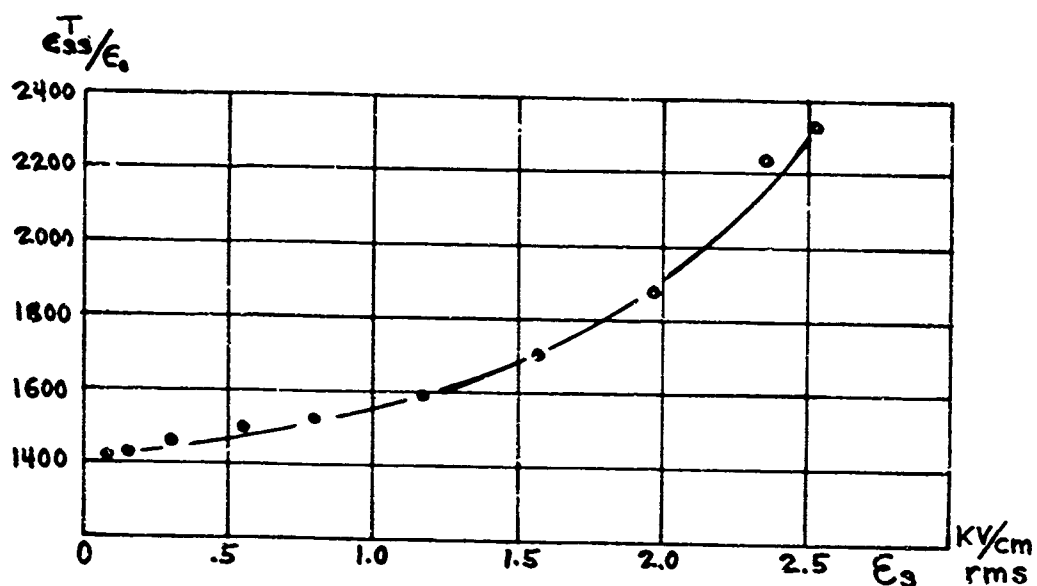


FIGURE 27
 5-inch Barium Titanate Bar
 PERMITTIVITY and INPUT DISSIPATION FACTOR

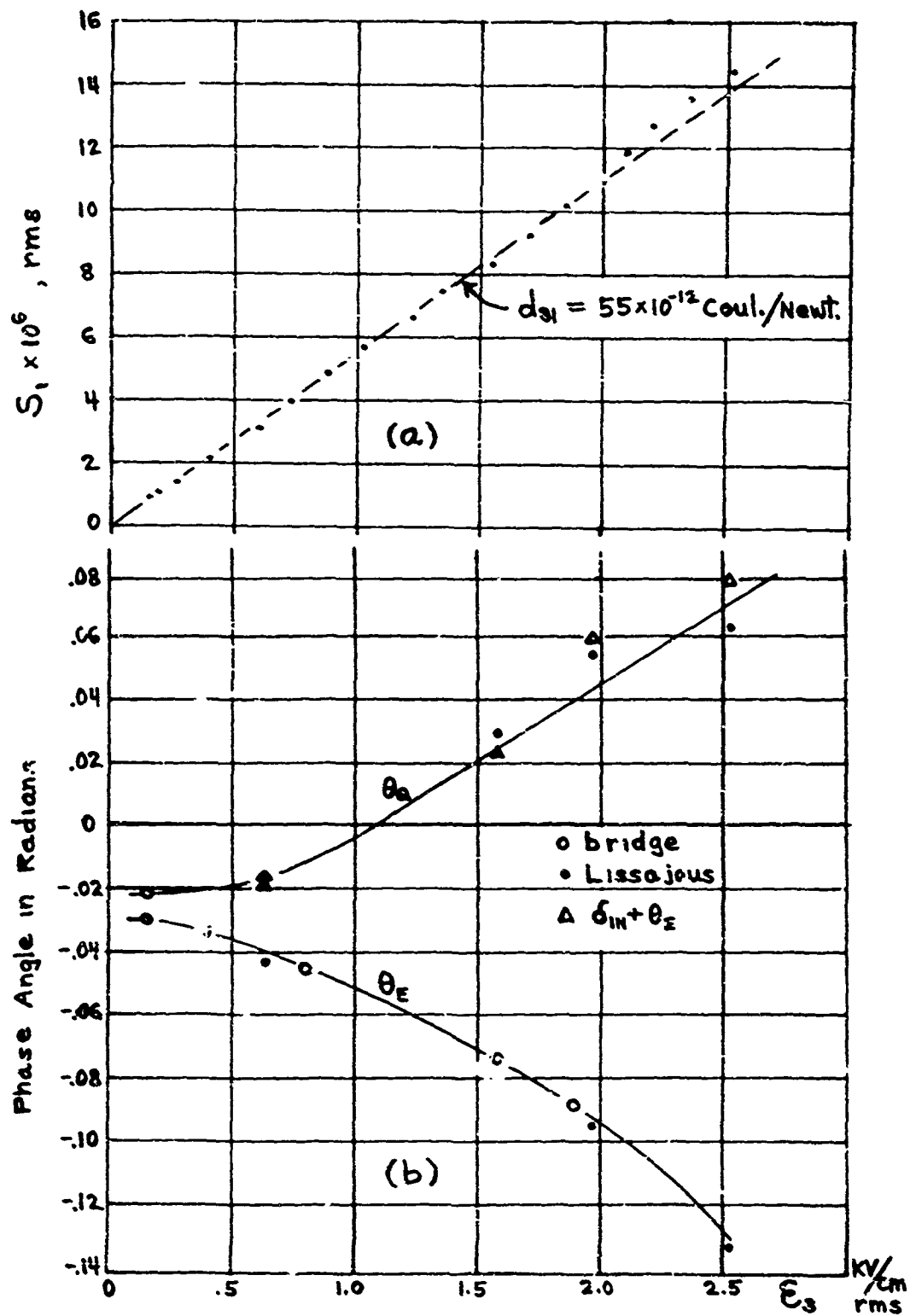


FIGURE 28
 5-inch Barium Titanate Bar
 (a) Strain (b) Transfer Phase Angles

All points on this curve (which covers the displacement range 791 - 14,600 \AA) were obtained directly by the interferometer. Displacement measurements were made at both the zeros of $J_1(2K\xi_1)$ and the zeros of $J_0(2K\xi_1)$. As mentioned in Section 3.2, the zeros of $J_1(2K\xi_1)$ are found by observing the output of a wave analyzer tuned to the fundamental frequency and recording the driving voltages at which the output approaches zero.

Although the zeros of $J_1(2K\xi_1)$ could be found even without the control system for stabilizing the operating point turned on, better results were obtained with the control system in operation. There were certain critical amplitudes at which this system tended to lose control. When this happens the amplifier saturates, and several minutes must elapse before it recovers and can be made to re-establish control. This trouble can be eliminated by reducing the gain of the amplifier; so for these measurements the feedback resistance R_f , shown in Figure 7, is reduced from $10 \text{ M}\Omega$ to $4 \text{ M}\Omega$. The critical amplitudes which disturb the control system were found to serve a useful purpose, for they correspond to the zeros of $J_0(2K\xi_1)$ and, therefore, enable these calibration points to be recorded. The effect of interest can be observed without actually throwing the system out of control by looking at the servo amplifier output e_0 on an oscilloscope. Normally the building vibrations are prominently seen in this output. But when the signal amplitude goes through a point where $J_0(2K\xi_1) = 0$, the building vibrations suddenly disappear from the oscilloscope trace. The signal itself is not seen on the oscilloscope because it is outside the passband of the servo system.

The control system behavior described above is in accordance with Equation (35) and the ensuing discussion in Section 3.4.2. When $J_0(2K\xi_1) = 0$, the error

signal which actuates the servo system is reduced to zero. The nulling of the vibration noise is very sharp, and this method is fully as satisfactory as the method which utilizes the zeros of $J_1(2K\xi_1)$ observed on a wave analyzer.

Figure 28a shows that the strain is a linear function of the electric field up to about 2 KV/cm. From the slope of this curve the d_{31} piezoelectric coefficient may be determined, and its value is 55×10^{-12} coulombs/Newton. This figure compares favorably with the nominal published value of 56×10^{-12} coulombs/Newton. Above 2 KV/cm the transfer parameter $|\xi/E|$ (or piezoelectric parameter d_{31}) increases about 5 percent. This is a very moderate change in view of the 60 percent increase in permittivity in this range of field as shown in Figure 27. The strain remains an almost-linear function of field at high driving levels, but it would show a pronounced saturation effect if it were plotted against electric displacement or polarization. The g_{31} piezoelectric coefficient, which is the ratio of strain to electric displacement, evidently decreases about 55 percent as the field is raised to the maximum value attained here.

The transfer phase angles θ_E and θ_Q are shown in Figure 28b for different values of driving field. The interferometer was used to measure absolute phase for the first point on each curve (at 100 V/cm), as described in Sections 5.2.2 and 5.2.3. Phase changes with respect to this datum were found by use of the Fotonic Sensor. Using the Lissajous pattern method with this instrument, as described in Section 5.2.6, the relative phases of both θ_E and θ_Q were measured. The results satisfy fairly well the requirement, given by Equation (13), that $\theta_Q - \theta_E = \delta_{IN}$. The transfer parameter bridge was also used with the Fotonic Sensor to measure changes in θ_E . These values are in agreement with those

obtained by the Lissajous pattern method. The bridge balance was rather broad because of noise and fluctuations from the Fotonic Sensor, but results were repeatable within ± 10 percent. Repeatability was not this good when attempts were made to measure θ_Q on the transfer parameter bridge. Perhaps the distortion in the charge wave form is responsible for the further deterioration of a method which is marginal at best. The measurements using Lissajous patterns with the interferometer, described in Section 5.2.5, gave results that were out of line with those obtained by the other methods. Furthermore, the interferometer results did not satisfy the requirement that $\theta_Q - \theta_E = \delta_{IN}$. Since this method is vulnerable to phase errors in the oscilloscope, it was decided to discard it for this project.

The small negative phase angles at low driving levels indicate that the strain lags both the electric field and the polarization for small signal conditions. As the driving level is raised, the strain (or displacement) begins to lead the polarization. This effect is perhaps surprising, but may seem less so if one recalls that the strain observed here is a transverse effect; that is, the measured strain is at right angles to the applied electric field. The results indicate that when the voltage across the bar thickness increases, causing the bar to expand its thickness, the cross-contraction reaches its maximum before the polarization is fully developed. In other words, the first effect of the domain motion is the cross-contraction; then slight further domain rearrangement takes place (without causing any more cross-contraction) before the polarization reaches its maximum.

7.2 5-inch Lead Titanate Zirconate Bars

A number of bars with dimensions $1/2'' \times 1/2'' \times 5''$ was obtained from Channel Industries. The material is a lead titanate zirconate composition (PZT) with properties similar to Clevite's PZT-4 ceramic. The electrodes are on the sides; so the voltage is applied across the half-inch thickness dimension, as was the case for the barium titanate bar described above. The standard low-level measurements on the set of bars showed them to be virtually identical in properties.

One bar was mounted in the same way as the barium titanate bar shown in Figure 24. A second bar had 17-inch pyrex glass rods cemented to each end to act as quarter-wave high-impedance terminations. This composite vibrator is similar to the one shown in Figure 25 except that it is on a larger scale. A plastic spring is attached to the center of the ceramic bar, and two .01-inch-thick steel springs spaced 10 inches apart are attached symmetrically to the glass rods. The resonant frequency of this suspension system is 45 Hz. A small mirror (.1" square, .05" thick) is cemented to the ceramic, perpendicular to its surface. The mirror is located at one end of the ceramic section, adjacent to the joint. Square glass rods to match the ceramic cross-section were difficult to procure; so 1/2-inch-diameter round rods are used instead. The joints are made with Armstrong A-2 epoxy adhesive and they are about .003-inch thick. Glass is chosen instead of metal for the stubs in order to avoid shorting out the electrodes on the ceramic section; a second reason is that the very low thermal expansion coefficient of PZT is less mismatched when glass is used.

The measurement program for the unloaded bar is essentially the same as for the barium titanate bar as described in the previous section. The operating

frequency is 3085 Hz in the present case, because this frequency corresponds to the quarter-wave frequency of the glass rods. The measurements on the bar with the quarter-wave stubs are confined to a determination of its electrical input impedance. While the electrical measurements are being made, the motion of the mirror on the ceramic adjacent to the joint is monitored with the interferometer.

The effectiveness of the blocking provided by the quarter-wave stubs was determined as follows. At a frequency of 1000 Hz the composite vibrator was driven until the mirror motion reached 926 Å. The driving voltage was then 95 V rms, which is the same voltage as is required to drive the unloaded bar to this amplitude. The photomultiplier output read on the wave analyzer was 1.23 V rms. Next the frequency was raised to 3085 Hz, where the motion dropped to its minimum value, and the composite vibrator was again driven with 95 V rms. The output of the wave analyzer was now 3.3 mV. By use of Equation (31), in which voltage may be substituted for current, the peak amplitude was computed to be 1.6 Å. The quarter-wave stubs thus reduce the motion by a factor of 580 from the motion existing under stiffness-controlled conditions. This seems like an impressive degree of blocking.

When the composite vibrator was driven at voltages up to 4000 V rms, the mirror motion increased roughly in proportion to the voltage. It was surprisingly easy to maintain the minimum-velocity condition. The wave analyzer, acting as a signal generator, was sufficiently stable for this task, and the quarter-wave frequency of the glass rods did not change with driving level. The PZT ceramic had much less tendency to heat up than the barium titanate, and such heat as was generated was not transmitted very significantly to the glass rods.

The results of the electrical input impedance measurements are shown in Figure 29. The superiority of PZT over barium titanate for high-power transducers is plainly evident from the plots of $\tan \delta_{IN}$ and ϵ_{33}^T . The dissipation factor and change of permittivity at high driving fields are much lower for the PZT. According to standard piezoelectric theory, the blocked permittivity is related to the free permittivity by the equation

$$\epsilon_{33}^S = \epsilon_{33}^T (1 - k_{31}^2) \quad , \quad (58)$$

where k_{31} is the electromechanical coupling factor. From the permittivity curves of Figure 29 the coupling factor may be computed and the results are given in Table 1. The low-level value agrees with the value obtained by conventional

TABLE 1
HIGH-FIELD DATA ON THE 5-INCH PZT BAR

ϵ_3 (KV/cm)	k_{31}	θ_N (radians)	δ_M (radians)	$ IN $ (Newt./volt)	ϵ_{11}^S (m ² /Newt.)
.080	.30	.027	.057	.18	19×10^{-12}
.79	.31	.019	.052	.19	18×10^{-12}
2.35	.34	-.014	.031	.25	15×10^{-12}
2.75	.36	-.019	.030	.29	13×10^{-12}
3.15	.37	-.019	.037	.32	13×10^{-12}

electrical measurements, and at high fields the coupling factor increases. Since most aspects of transducer performance improve with an increase in coupling factor, the high-field behavior of this factor is gratifying. But, of course, caution must

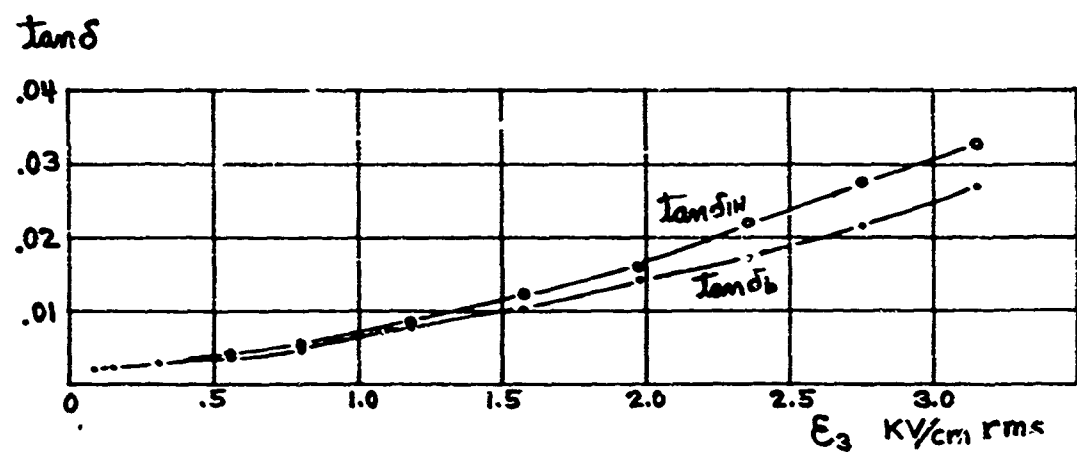
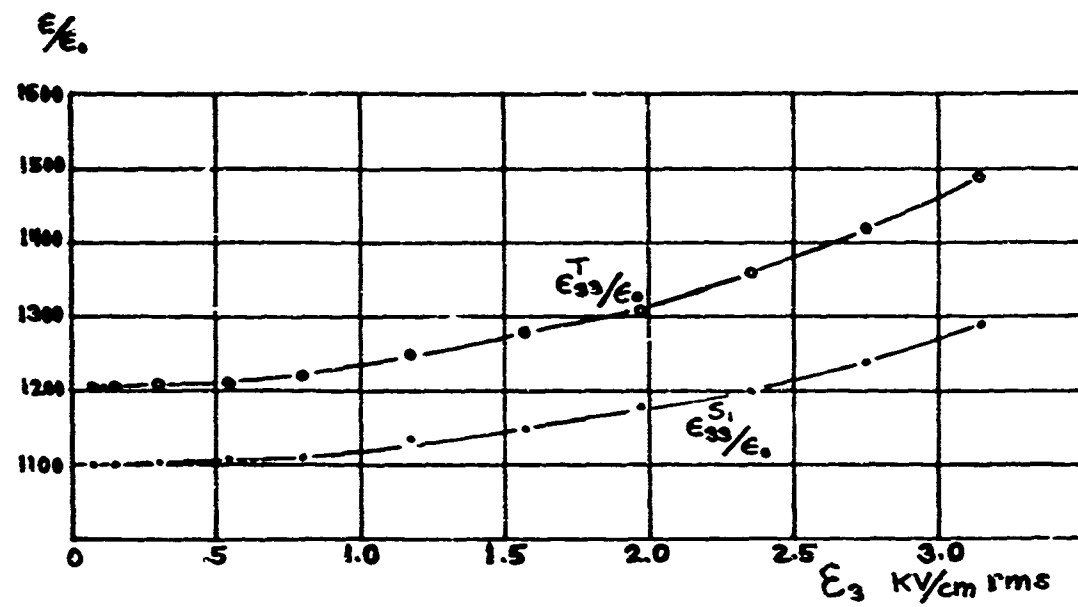


FIGURE 29
5-inch PZT Bar
Permittivity and Input Dissipation Factor

be exercised in extending any conclusions reached from small-signal studies to the large-signal case.

Figure 30a shows the relation between the a.c. strain and the driving field. Values of displacement up to $31,200 \text{ \AA}$ were measured successfully with the interferometer. Above this amplitude, identifying the order of the zeros of $J_0(2K\xi_1)$ and $J_1(2K\xi_1)$ became difficult. The calibration points were crowded on the voltmeter scale, and the ceramic would get warm if time was spent in careful adjustment of the voltage so as to avoid skipping any calibration points. The last part of the curve is an extrapolation based on Fotonic Sensor measurements using the circuit of Figure 20a. The strain curve is similar to that for the barium titanate bar, although the slope of the straight-line portion (i.e., the d_{31} coefficient) is almost three times greater. The decrease in the g_{31} coefficient at maximum field is approximately 15 percent, or about one-third the decrease found for barium titanate.

Figure 30b shows the variation of the transfer phase angles θ_E and θ_Q with driving field. The first point on each curve was measured with the interferometer, and the relative phase changes with respect to these initial points were measured with the Fotonic Sensor operating in the transfer bridge setup. As always with this arrangement, the bridge balances were rather broad. Attempts to confirm the bridge measurements with Lissajous patterns (using the circuit of Figure 21c) were made. No phase change in θ_Q with driving field could be seen, but this is to be expected since the changes shown by the bridge method are so small. The lag of θ_E was definitely observed to increase with increasing field, and while the precision of this measurement was poor, the magnitude of the phase

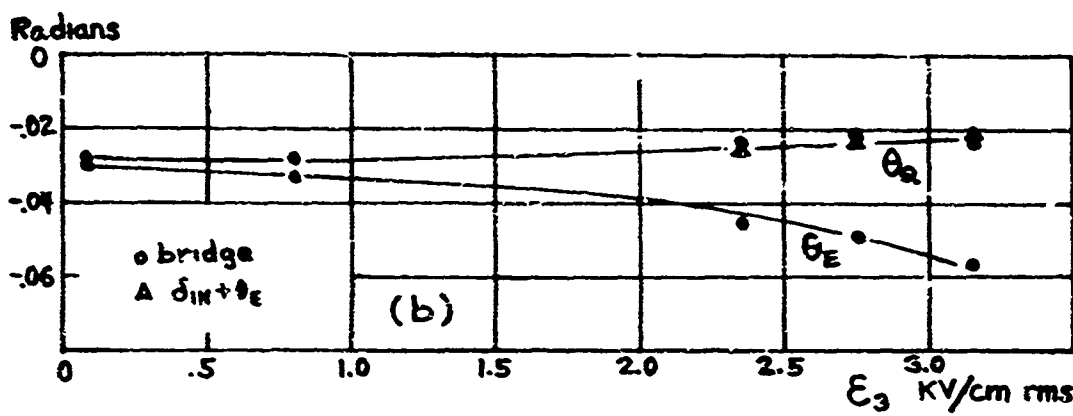
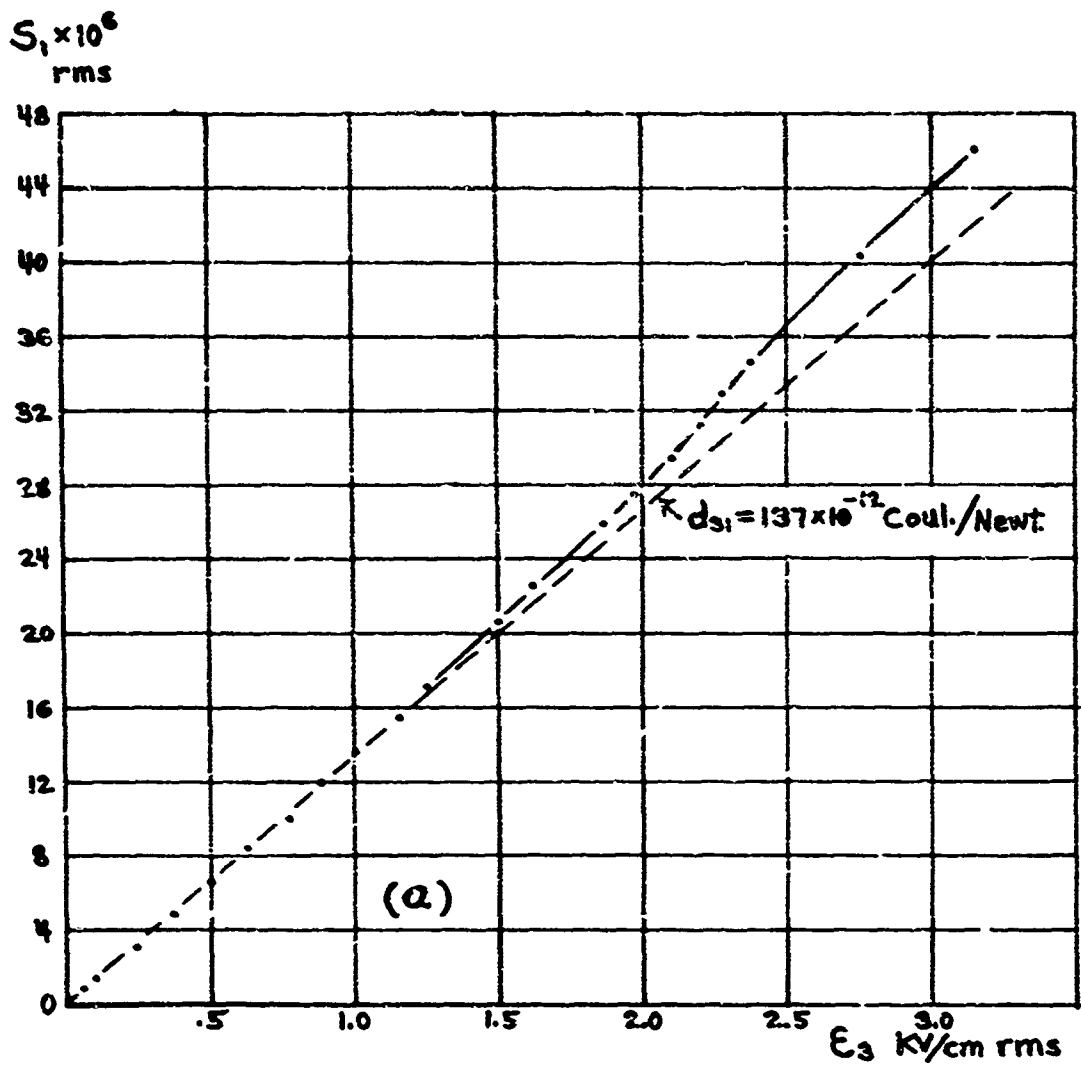


FIGURE 30
 5-inch PZT Bar
 (a) Strain (b) Transfer Phase Angles

change was in rough agreement with the bridge results. It is concluded that the behavior of the PZT bar is qualitatively the same as that of the barium titanate bar, even though the effects are much less pronounced at the highest fields that could be applied with the present apparatus.

Enough measurements were made on these PZT bars to enable all the electromechanical circuit parameters, or all the applicable piezoelectric parameters, to be calculated. The reliability of the results will have to be carefully evaluated, but one can proceed with the calculations and judge their validity later. As indicated in Equation (15), the first step is to perform a phasor subtraction of the blocked admittance from the input admittance to obtain the motional admittance. The motional admittance is the electrical equivalent of the mechanical admittance, except for modifications introduced by the transformation ratio N as a result of its nonideal behavior. When the motional admittance data and ξ/E transfer ratio data are combined in Equation (16), the parameter N is found. Then the mechanical impedance is obtained from Equation (17).

The essential results of these calculations are given in Table 1. The mechanical impedance is represented by the mechanical loss angle δ_m (defined in Figure 2) and the compliance constant s_{11}^E . From these parameters the actual components of the mechanical impedance, as used in Equation (17), can readily be computed but they are generally less meaningful than the parameters in the table. The physical realizability conditions (8) and (10) are satisfied with ample margin by the data contained in Table 1 and Figure 29; so the validity of the data can not be questioned on thermodynamic grounds. The data for the magnitudes $|N|$ and s_{11}^E should be highly reliable, and they reveal very pronounced

dependence of these parameters upon the driving field strength.

The results for the angles θ_N and δ_M must be treated with some suspicion until such time as independent measurements of these parameters are carried out and reported. In spite of the fact that the blocking action of the quarter-wave bars is deemed highly successful, one must still be concerned about the residual motion of the ends of the bar when considering energy dissipation. It is conceivable that enough energy is dissipated in the thin cement layers by this residual motion to invalidate the assumption that $\tan \delta_b$, as given in Figure 29, is a measure of the energy dissipated in the ceramic bar. If the angle δ_b is erroneous, then the computed angles θ_N and δ_M will also be erroneous.

The only information in Table 1 that is considered suspicious on its face value is the positive sign associated with θ_N for the 100-volt and 1000-volt driving levels. When θ_N is positive, the force exerted by the blocked transducer on the blocking clamps will lead the applied voltage. In considering the response of the ferroelectric domains to an electric field it is difficult to discover any mechanisms that might cause the force to lead the electric field. If the parameters of the circuit of Figure 3 are calculated from the data of Table 1 and Figure 29, the resistance R_A will be negative when θ_N is positive. This fact is interesting but not prejudicial, since the other resistance in the circuit will dissipate more energy than is generated by R_A under all conditions of operation. Numerical values for the circuit elements of Figure 3 would be useful in specific applications but they are not of enough general interest to be presented here.

7.3 3/4-inch Lead Titanate Zirconate Bars

All the results given above are for bars in which the electric field is perpendicular to the measured motion. To obtain some information on ceramic behavior when the field is parallel to the motion, 3/4-inch bars with axial polarization were procured. These were obtained from Clevite Corporation in their PZT-4 composition. They are round bars, 3/8 inch in diameter, and the electrodes are on the ends. Low-level measurements showed all samples to be virtually identical.

One bar was mounted on a single cellulose acetate spring; it is shown in Figure 25b. A second bar, shown in Figure 25a, had 6-inch pyrex glass rods cemented to each end so that it could be used for blocked-ceramic experiments. To make electrical connections to the silver electrodes it was necessary to insert a layer of .003-inch-thick expanded-metal screen in each joint. The motion of the end of the ceramic section, measured with the aid of a small mirror cemented on the side, was minimum at 8660 Hz. At this frequency the displacement was down by a factor of 110 from the value observed at 3000 Hz with the same driving voltage applied.

The measurements program carried out on these bars was essentially the same as that described in the previous sections for the other ceramic bars. It was not possible to generate electric fields as high as for the other samples, however. The electrical input impedance data are given in Figure 31. The change of permittivity with driving field for the free bar is about the same as for the Channel Industries material, but the dissipation factor $\tan \delta_{IN}$ runs higher. The dissipation factor of the bar with the quarter-wave stubs is so high that it suggests that cement losses are playing a dominant role. The electromechanical coupling

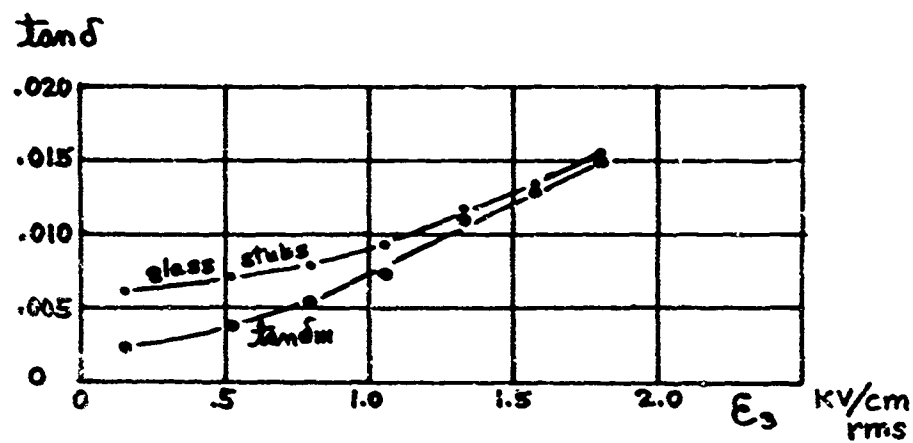
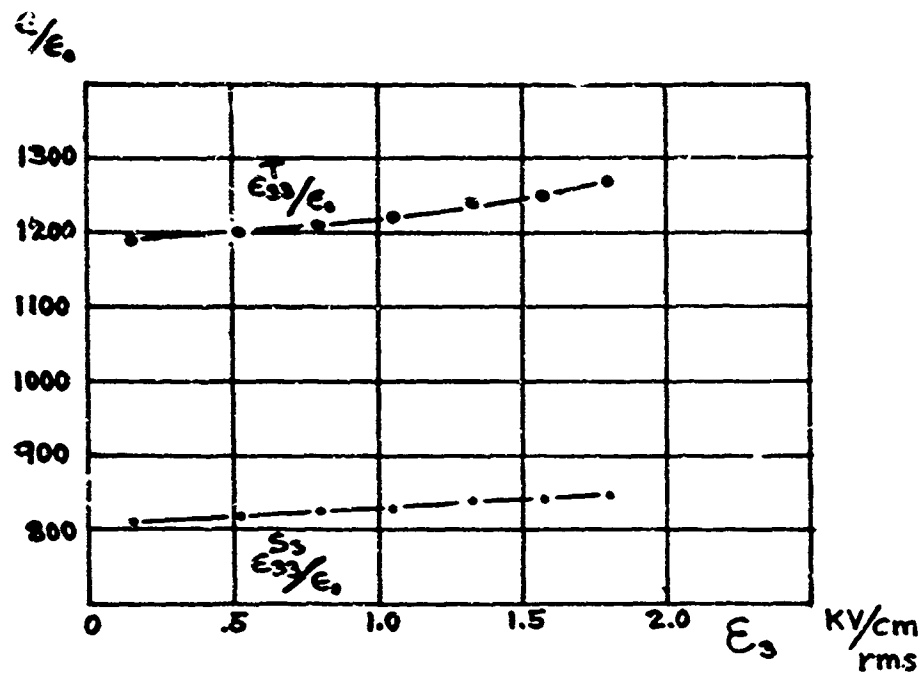


FIGURE 3a
 $\frac{3}{4}$ -inch PZT Bar
 Permittivity and Input Dissipation Factor

factor k_{33} starts at .56 and rises to .58 at 1.8 KV/cm.

The relation between strain and driving field is shown in Figure 32a. The d_{33} coefficient increases at high field strengths, in a similar manner to the d_{31} coefficient observed with the previous samples. The relative increase in d_{33} just about equals the relative increase in the permittivity ϵ_{33}^T . Consequently, the g_{33} coefficient is substantially independent of driving field up to the highest point reached in this investigation, and this behavior contrasts with that of g_{31} , which decreases at high field strengths.

The transfer phase angles θ_E and θ_0 are shown in Figure 32b. The interferometer was used to obtain the initial points, and the rest of the curves were measured with the Fotonic Sensor and transfer bridge. Lissajous patterns with the Fotonic Sensor were confirmatory; that is, no phase change in θ_0 with increasing field could be detected, while a definite increase in lag for θ_E was seen, and the magnitude of the change was in rough agreement with the transfer bridge results.

The 3/4-inch unloaded bar was useful for checking the phase lag that is consistently found for both θ_E and θ_0 by the interferometer at low-signal levels. The interferometer and transfer bridge setup (Figures 20a and 21a) gave the following results: at 8.7 kHz $\theta_E = .015$ radian; at 3 kHz $\theta_E = .015$ radian; at 1 kHz $\theta_E = .020$ radian. If the reported lag of θ_E at low levels were not a real effect but were actually due to transit time or undetermined capacities in the photomultiplier, the phase lag would be expected to increase with frequency. But no such increase was found.

If the complete set of data on the 3/4-inch bars is processed as was done in

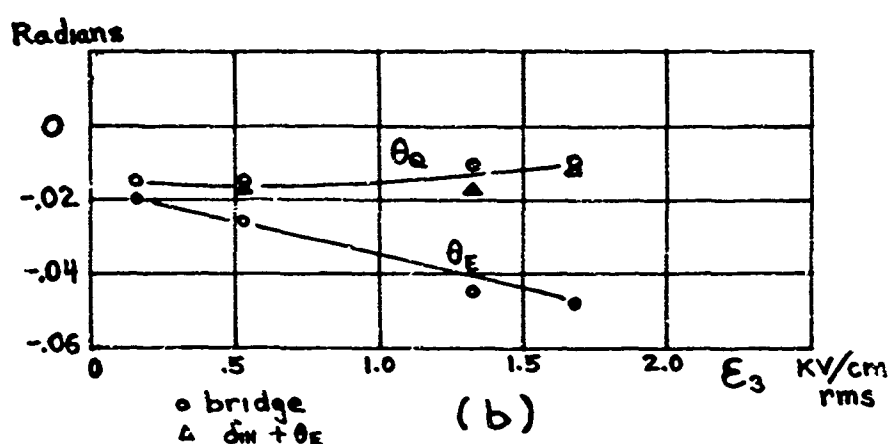
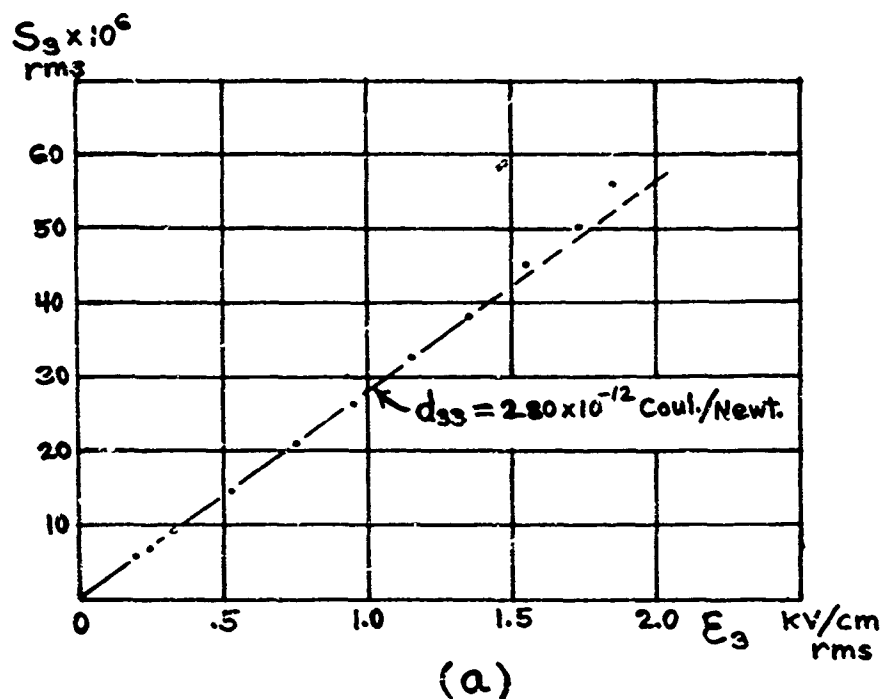


FIGURE 32

$\frac{3}{4}$ -inch PZT Bar
 (a) Strain (b) Transfer Phase Angles

the previous section in an attempt to find θ_N and δ_M , it is immediately found that the motional conductance is negative when the subtraction indicated in Equation (15) is carried out. Even so, physical realizability conditions are not violated. But the calculations result in large angles ($\theta_N = .05$ radian, $\delta_M = .07$ radian) even at low driving levels. Since the blocking effect achieved with the composite vibrator incorporating the 3/4-inch bar is relatively poor, discarding these phase angle results is undoubtedly justified. The poorer performance of this composite vibrator relative to the one described in the previous section is probably attributable to the thicker joints (incorporating metal screen) and to the higher frequency.

Determination of the changes in magnitude of INl and C_M^E from the experimental data is probably valid even though the phase angle results are not. The results indicate that C_M^E is substantially independent of field, while INl goes from .093 to .097 Newton/volt as the field is raised from .2 to 1.8 KV/cm.

7.4 Discussion of Results

The barium titanate bar showed the most interesting results. Its high-field effects are large enough that they are measurable with fairly good accuracy. On the other hand, heat generation in this ceramic is a severe problem and can easily lead to inconsistencies in the results, which are all intended to apply at a common temperature. Heating is avoided by the use of short pulses, but when the signal-to-noise ratio is low pulse methods may lead to loss of accuracy. Measurements on an axially poled barium titanate bar would be valuable to complement the results obtained here on the bar with transverse polarization. Barium titanate samples

similar to the 3/4-inch PZT bars could not be obtained from the manufacturers, however.

For all of the ceramics the displacement ξ , or strain, lagged the driving field to an increasing degree as the field strength was increased. The phase relations of the strain with respect to the polarization were more diverse. For the barium titanate bar with transverse field the strain took on a leading phase angle with respect to the polarization at high driving levels, but this did not happen with the other samples. There was a trend for θ_Q to increase with driving field for both PZT samples, but the accuracy of these results is not high. A leading phase angle for θ_Q seems more reasonable for bars with transverse electric field (where this effect was found in the case of barium titanate) than it would for bars with axial field.

The fact that θ_E and θ_Q had lagging phase angles that were larger than the input loss angles δ_{IN} at low driving levels was unexpected. For example, in the barium titanate bar the initial values of these angles were: $\theta_N = -.03$ radian, $\delta_{IN} = .007$ radian. The difficulties of measuring these small angles are so formidable that one may be tempted to attach no significance to these small values. However these results were obtained consistently, and no sources of a systematic error could be uncovered.

Besides being unexpected, the initial lag angles of θ_E have disturbing implications with respect to θ_N . In Table 1, θ_N is shown with a positive phase angle for low fields. This effect might be caused, in part, by deficiencies in the measurement of the blocked loss angle δ_b , but it is also influenced by the phase angle of θ_E . For example, if the initial phase angle of θ_E were taken to be

zero rather than its reported value of .03, calculation of θ_N would then yield a negative phase angle for the low-field cases in Table 1.

The reason that positive phase angles for θ_N are considered disturbing is because it is difficult to devise an explanation in terms of ferroelectric domain behavior for the blocked force leading the applied field. If one looks for a source of phase lead outside of the ceramic, one sees that a series condenser would produce this effect (as long as $\delta_b \neq 0$). Such a series condenser would exist if the electrodes were separated from the ceramic by a slight gap. However, no reasonable gap would produce a phase shift of the order of .03 radian. Gaps also exist at the grain boundaries inside the ceramic. It does not seem likely that their cumulative effect would produce a significant phase shift, but this matter deserves further study.

The measurement of magnitudes, such as $|\xi/E|$, C_{IN} , and $|NI|$, are more reliable than the measurement of phase and loss angles. For the bar with transverse field the measurements show that the displacement of the free bar is more nearly proportional to the electric field than it is to the polarization. On the other hand, the blocked force is more nearly proportional to the polarization than to the electric field. The latter conclusion follows from an examination of the values of $|NI|$ in Table 1. These conclusions do not appear to apply to the bar with axial field, although this bar could not be driven with high enough fields to show very pronounced nonlinear effects.

VIII CONCLUSIONS

The major conclusions resulting from this investigation are listed below.

The laser interferometer for measuring vibrations can be considerably improved by the addition of electronic control systems to stabilize the path length of the interfering beams and to stabilize the intensity of the laser's output. Phase measurements as well as amplitude measurements may be made in the small-signal, quasi-linear range of this instrument. Phase measurements can also be made in the large-signal, nonlinear range, but an oscilloscope with exceptional phase accuracy would be required if the phase of the vibration is to be measured within an accuracy of 1-degree.

The Fotonic Sensor manufactured by Mechanical Technology Inc. is very useful for measuring vibration amplitudes above 1000 Å, but is of marginal value for the measurement of phase at low vibration amplitudes. The high electronic noise level of this instrument is inherent in its principle of operation, and the prospects of effecting any major improvements are not bright.

The electromechanical transfer ratios relating displacement to voltage or displacement to charge can be measured with the instrumentation developed under this project. Both amplitude and phase of these ratios may be measured for piezoelectric ceramic vibrators in the audio frequency range. Attainment of phase accuracies of better than 1 degree is possible only under favorable circumstances,

and further improvement of this instrumentation is desirable.

The problem of applying known mechanical load impedances to transducers is still far from solved. An important step in this direction was taken with the quarter-wave stub approach used in this investigation. Blocking the transducer to the extent that the velocity was reduced by a factor of 500 was achieved. Some question remains as to whether the dissipation in the cement joints is a significant factor.

There is no simple one-to-one correspondence between the polarization and the piezoelectric strain in ceramics. When the driving field is transverse to the measured motion, the strain leads the polarization in barium titanate. The magnitude of the strain in this transverse field case is more nearly proportional to the electric field than to the polarization.

The nonlinearity of the piezoelectric ceramics is very noticeable in the way all parameters vary both in phase and magnitude with driving level. Wave-form distortion, however, is quite small. The validity of superposition in the design of high-power transducers is questionable. A great deal of work, both theoretical and experimental, remains to be done on nonlinear phenomena in piezoelectricity before the design of high-power transducers will be thoroughly understood.

BIBLIOGRAPHY

1. H. D. Megaw, Ferroelectricity in Crystals (Methuen and Co., Ltd., London, 1957).
2. P. W. Forsbergh, Jr., "Piezoelectricity, Electrostriction and Ferroelectricity," Handbuch der Physik (Band XVII, Springer-Verlag, Berlin, 1956).
3. F. Jona and G. Shirane, Ferroelectric Crystals (Pergamon Press, New York, 1962).
4. W. Kanzig, Ferroelectrics and Antiferroelectrics, Solid State Physics (Academic Press, New York, 1957), Vol. 4.
5. W. P. Mason (Editor), Physical Acoustics (Academic Press, New York, 1964), Vol. 1 Part A, Chap. 3.
6. W. G. Cady, Piezoelectricity (Dover Publications, Inc., New York, 1954).
7. W. P. Mason, Piezoelectric Crystals and Their Application to Ultrasonics (D. Van Nostrand Co., Inc., New York, 1950).
8. J. J. Z. Van Zeist, "Circuit for Condenser Microphones with Low Noise Level," Philips Tech. Rev. 9, 357 (1947/1948).
9. W. Koidan, "An Acoustic Method for the Measurement of Vibration Amplitudes," J. Acoust. Soc. Am. 26, 428 (1954).
10. J. H. Jurmain, "Application of Tensor Analysis to Elasticity and Piezoelectricity," J. Franklin Inst. 245, 475 (1948), based on MS Thesis, Tufts College (1947).
11. 61 IRE 14.51 Committee, "IRE Standards on Piezoelectric Crystals: Measurements of Piezoelectric Ceramics, 1961," Proc. IRE 49, 1161 (1951); and "1949 Standards" Proc. IRE 37, 1378 (1949).
12. R. Holland, "Representation of Dielectric, Elastic, and Piezoelectric Losses by Complex Coefficients," IEEE Transactions SU-14, 18 (1967).

13. R. S. Woollett, "Effective Coupling Factor of Single-Degree-of-Freedom Transducers," *J. Acoust. Soc. Am.* 40, 1112 (1966).
14. H. J. Carlin and A. B. Giordano, Network Theory (Prentice-Hall, Inc., Englewood Cliffs, 1964).
15. R. Gerson, "Dependence of Mechanical Q and Young's Modulus of Ferroelectric Ceramics on Stress Amplitude," *J. Acoust. Soc. Am.* 32, 1297 (1960).
16. C. E. Land, G. W. Smith, C. R. Westgate, "The Dependence of the Small-Signal Parameters of Ferroelectric Ceramic Resonators upon State of Polarization," *IEEE Transactions SU-11*, 8 (1964).
17. G. E. Martin, Unpublished Report, Office of Naval Research, Code 468, (April 1965).
18. R. S. Woollett, "Trends and Problems in Sonar Transducer Design," *IEEE Transactions UE-10*, 116 (1963).
19. H. Osterberg, "An Interferometer Method of Studying the Vibrations of an Oscillating Quartz Plate," *J. Opt. Soc. Am.* 22, 19 (1932).
20. R. L. Powell and K. A. Stetson, "Interferometric Vibration Analysis by Wavefront Reconstruction," *J. Opt. Soc. Am.* 55, 1593 (1965).
21. V. A. Schmidt, S. Edelman, E. R. Smith, and E. Jones, "Optical Calibration of Vibration Pickups at Small Amplitudes," *J. Acoust. Soc. Am.* 33, 748 (1961).
22. H. A. Deferrari and F. Andrews, "Laser Interferometric Technique for Measuring Small-Order Vibration Displacements," *J. Acoust. Soc. Am.* 39, 979 (L) (1966).
23. P. Rabinowitz, S. Jacobs, R. Targ, and G. Gould, "Homodyne Detection of Phase-Modulated Light," *Proc. IRE* 50, 2365 (L) (1962).
24. H. S. Black, Modulation Theory, (D. Van Nostrand, New York, 1953), p. 188.
25. C. Chandler, Modern Interferometers, (Hilger and Watts, Ltd., London 1951).
26. "Phototubes and Photocells," Technical Manual PT-10, Radio Corp. of Am., Lancaster (1963).

27. J. C. Snowdon, "Approximate Expression for the Mechanical Impedance
and Transmissibility of Beams Vibrating in Their Transverse Modes,"
J. Acoust. Soc. Am. 36, 366 (1964).

UNCLASSIFIED
Security Classification

DOCUMENT CONTROL DATA - R & D

(Security classification of title, body of abstract and indexing annotation must be entered when the overall report is classified)

1. ORIGINATING ACTIVITY (Corporate author)		2a. REPORT SECURITY CLASSIFICATION
U. S. Navy Underwater Sound Laboratory Fort Trumbull, New London, Connecticut		UNCLASSIFIED 2b. GROUP
3. REPORT TITLE		
MEASUREMENT OF THE DISSIPATION ASSOCIATED WITH THE ELECTRO-MECHANICAL COUPLING IN PIEZOELECTRIC CERAMICS		
4. DESCRIPTIVE NOTES (Type of report and inclusive dates) Research		
5. AUTHOR(S) (First name, middle initial, last name) Ralph S. Woclett		
6. REPORT DATE 12 July 1967	7a. TOTAL NO. OF PAGES 146	7b. NO. OF REFS 27
8a. CONTRACT OR GRANT NO	8a. ORIGINATOR'S REPORT NUMBER(S) 834	
b. PROJECT NO SF 101 03 18-11287	8b. OTHER REPORT NO(S) (Any other numbers that may be assigned to this report)	
c. 7-1-451-00-00	d.	
10. DISTRIBUTION STATEMENT This document has been approved for public release and sale; its distribution is unlimited.		
11. SUPPLEMENTARY NOTES	12. SPONSORING MILITARY ACT. VITY U. S. Navy	
13. ABSTRACT The object of this investigation is to develop methods for precise measurements of velocity or displacement (including their phase angles as well as their magnitudes) and to apply these methods to extend the knowledge of the dissipative parameters of piezoelectric ceramics. Laser interferometry is a very promising new method for measuring small vibrations. In this method the motion of a small mirror attached to the vibrating body phase-modulates the light beam, and the light beam is subsequently demodulated by a photomultiplier tube. An electronic control system was developed to stabilize the interferometer against low-frequency building vibrations. In this system the mirror of the interferometer that is normally fixed is mounted on a small piezoelectric transducer. This transducer is driven by a servo amplifier in such a manner that it keeps the path length of the interfering beams constant at low frequencies. Building vibrations thus are canceled out, but the control system becomes inoperative above 1 kHz and, hence, does not interfere with the measurement of the desired vibration signals, which are in this upper frequency range. Another feedback control system was developed to stabilize the amplitude of the laser output, which was found to fluctuate as much as 10 percent. These fluctuations were reduced to about 1 percent. After suitable measurement methods had been developed, measurements were made of the electromechanical transfer ratios of a number of ceramic samples. It was found that there was no simple one-to-one relation between the mechanical displacement and the polarization under stiffness-controlled conditions. The phase angle between the displacement and charge in barium titanate bars with transverse field becomes a lead angle at high drive levels. The amplitude of displacement for these bars is more nearly proportional to the electric field than to the polarization. Some samples were measured under blocked conditions by use of quarter-wave blocking stubs. In this way enough data were obtained to calculate a complete set of two-port parameters.		

DD FORM 1473 (PAGE 1)

S/N 0101-607-6001

UNCLASSIFIED

Security Classification

300 PP30 13292

UNCLASSIFIED

Security Classification

14 KEY WORDS	LINK A		LINK B		LINK C	
	ROLE	WT	ROLE	WT	ROLE	WT
Sonar Transducers Sonar Transducer Materials Physical Properties of Ceramics Dissipative Parameters of Piezoelectric Ceramics Electromechanical Transfer Ratio Laser Interferometry for Measuring Small Vibrations						

DD FORM NOV 68 1473 (BACK)
(PAGE 2)**UNCLASSIFIED**
Security Classification